Vibrational Excitation of Nitrogen and Carbon Dioxide for Plasma-Assisted Catalysis and CO_2 Remediation

Thesis

Presented in Partial Fulfillment of the Requirements for the Degree Master of Science in the Graduate School of The Ohio State University

By

Caleb Richards

Graduate Program in Mechanical Engineering

The Ohio State University

2021

Thesis Committee

Dr. Igor V. Adamovich, Advisor

Dr. Jeffrey Sutton

Copyright by

Caleb Richards

2021

Abstract

Time-resolved N_2 vibrational temperature and translational-rotational temperature in quasi-two-dimensional atmospheric pressure plasma jets sustained by ns pulse and RF discharges in nitrogen / noble gas mixtures are measured by the broadband vibrational CARS. The results indicate a much stronger vibrational excitation in the RF plasma jet, due to the lower reduced electric field and higher discharge power. In a ns pulse discharge in N_2/He, N_2 vibrational temperature is significantly lower compared to that in N_2/Ar, due to the more rapid V-T relaxation of nitrogen by helium atoms. In the RF plasma jets in N_2/Ne and N_2/Ar, the vibrational excitation increases considerably as the nitrogen fraction in the mixture is reduced. The experimental data in the RF plasma jet in N_2/Ar jet are compared with the kinetic modeling predictions. The results indicate that nitrogen vibrational excitation in N_2/Ar plasma jets with a small N_2 fraction in the mixture (several percent) is controlled primarily by electron impact, anharmonic vibration-vibration (V-V) pumping, and vibration-translation (V-T) relaxation by N atoms. In comparison, V-V energy transfer from the vibrationally excited molecules in the first excited electronic state, $N_2(A^3\Sigma_u^+,v)$, which are generated primarily by the energy transfer from the metastable Ar atoms, has a minor effect on the vibrational populations of the ground electronic state, $N_2(X^1\Sigma_g^+,v)$. Although the discharge energy fraction going to electronic excitation is significant, the predicted quasi-steady-state $N_2(A^3\Sigma_u^+)$ number density, controlled by the energy pooling and quenching by N atoms, remains relatively low. Because of this, the net rate of $N_2(X^1\Sigma_g^+)$ vibrational excitation by the V-V energy transfer from $N_2(A^3\Sigma_u^+)$ is much lower compared to that by the direct electron impact. The results show that atmospheric pressure RF plasma jets can be used as sources of highly vibrationally excited N_2 molecules and N atoms.

In a closely related experiment, time-resolved CO_2 and N_2 vibrational populations and translational-rotational temperature are measured in a CO_2-N_2 plasma sustained by a ns pulse discharge burst in plane-to-plane geometry. Time-resolved, absolute number density of CO generated in the plasma is also inferred from the experimental data. CO_2 and CO vibrational populations are measured by mid-IR, tunable Quantum Cascade Laser Absorption Spectroscopy, and N_2 vibrational populations are measured by the ns broadband vibrational CARS. Transient excitation of N_2 and CO_2 asymmetric stretch vibrational energy modes is detected during the discharge burst. The time-resolved rate of CO generation does not correlate with N_2 or $CO_2(\nu_3)$ vibrational temperatures, suggesting that CO_2 dissociation via the vibrational excitation is insignificant at the present conditions. The rate of CO generation decreases during the discharge burst. The estimated specific energy cost of the CO product is close to that of N atoms in pure nitrogen, measured at similar operating conditions. The effective cost, based on the input energy fraction going to CO_2, is approximately 6.5 eV, close to the threshold of CO_2 electron impact dissociation cross section. This suggests that CO_2 dissociation by electron impact may be the dominant channel of CO generation at the present conditions.

Acknowledgements

I am thankful for and deeply indebted to those with whom I worked and learned alongside with during my time at Ohio State. In particular, the generosity, knowledge, and work of Elijah Jans, Xin Yang, Keegan Orr, Sai Raskar, David Mignogna, Ilya Gulko, and Nathan Radomski are gratefully acknowledged.

Additionally I would like to thank those who facilitated and made my research visit at Sandia Livermore National Laboratory successful, especially Dirk van den Bekerom, Erxiong Huang, and Jonathan Frank.

The skills and expertise of those who fabricated essential components for the experiments are appreciated, especially Timothy Henthorne at the Ohio State Chemistry glass blowing shop and Aaron Orsborne from the MAE student machine shop.

Finally, I would like to extend my thanks to my Dr. Igor Adamovich for sharing time and knowledge with me and taking exceptional interest in my research. The wealth of knowledge I received will continue to benefit me throughout my career. Additionally, I am thankful for the opportunity to interact with Dr. Bill Rich, as his enthusiasm and extensive background have been uniquely beneficial to experience.

Vita

2019 Bachelor of Science in Mechanical Engineering with Minor in Physics, the Ohio State University, Columbus, OH

2019-2021 Graduate Research Assistant, the Ohio State University, Columbus, OH

Publications

Richards, C., Jans, E. R., Gulko, I., Orr, K., & Adamovich, I. V. (2021). “N_2 Vibrational Excitation in Atmospheric Pressure Ns Pulse and RF Plasma Jets.” under review at Plasma Sources Science and Technology

Gulko, I., Jans, E. R., Richards, C., Raskar, S., Yang, X., van den Bekerom, D. C. M., & Adamovich, I. V. (2020). “Selective generation of excited species in ns pulse/RF hybrid plasmas for plasma chemistry applications.” Plasma Sources Science and Technology, 29(10), 104002. https://doi.org/10.1088/1361-6595/abb3a1

Yang, X., Jans, E.R., Richards, C., Raskar, van den Bekerom, D. C. M., Wu, K., & Adamovich, I. V. (2021). “Measurements of atoms and metastable species in N_2 and H_2-N_2 Ns pulse plasmas.” Accepted for Publication in Plasma Sources Science and Technology, 29(10), 104002. https://doi.org/10.1088/1361-6595/ac3053

Field of Study

Mechanical Engineering

Table of Contents

List of Tables

List of Figures

Chapter 1. Introduction

1.1 Background: Vibrational Excitation in Atmospheric Pressure Plasma Jets

Generation and detection of vibrationally excited molecules in nonequilibrium high pressure plasmas are of considerable importance for engineering applications such as molecular lasers, plasma chemical syntheses, and plasma-assisted catalysis. Vibrational excitation of reactants, stimulated by the anharmonic vibration-vibration (V-V) pumping [1], is known to enhance considerably the rates of gas-phase chemical processes, such as CO_2 dissociation [2-4], associative ionization and carbon disproportionation reaction between two CO molecules [5,6], and nitric oxide formation in a reaction of N_2 with O atoms [7]. In addition, surface reactions of vibrationally excited N_2 [8] and CO [9] have been suggested as possible dominant channels of plasma-catalytic ammonia and CO_2 formation.

Strong vibrational excitation of molecules such as N_2, CO, H_2, and CO_2 in DC, RF, and microwave discharges have been detected in a number of previous studies, using mid-IR laser absorption spectroscopy, spontaneous Raman scattering, FTIR emission spectroscopy, and CARS (e.g. see [2, 10-16]). At these conditions, efficient vibrational excitation is produced by electron impact, over a wide range of reduced electric fields (E/N). Strong vibrational excitation of N_2 has also been detected in ns pulse discharges in nitrogen and air [17-22]. Although peak E/N in a ns pulse discharge is typically too high for efficient vibrational excitation by electron impact, in ns discharges with metal electrodes most of the energy is coupled to the plasma at a lower, quasi-steady-state E/N value reached after breakdown, where vibrational excitation processes become more efficient.

Recently, strong vibrational excitation of nitrogen has also been detected in an atmospheric pressure RF plasma jets, at relatively low N_2 fractions in the mixture with He or Ar (several per cent) [23,24]. At these conditions, a significant fraction of the discharge input energy goes to electronic excitation of He or Ar by electron impact, with the subsequent energy transfer to excited electronic states of N_2, such as $A^3\Sigma_u^+$ [25]. N2 vibrational excitation at these conditions may occur both by electron impact and during the quenching of $N_2(A^3\Sigma_u^+)$ molecules [26], such that the kinetic mechanism of this process is not fully understood. An objective of the present study is to quantify the vibrational nonequilibrium of nitrogen in atmospheric pressure plasma jets in N_2 / inert gas mixtures generated by a ns pulse discharge train and by an RF waveform, and to elucidate the dominant mechanisms of N_2 vibrational excitation in the mixtures with different amounts of nitrogen.

1.2 Background: Carbon Dioxide Dissociation

CO_2 dissociation in nonequilibrium plasmas has been studied extensively in the past, following the early experiments indicating that it is enhanced by vibrational excitation [27], and demonstration of strong vibrational excitation of CO_2 in DC glow discharges [28,29]. The vibrational mode-specific kinetics of this process is discussed in great detail in [30]. Over the last decade, a considerable effort has been devoted to the development and optimization of CO_2 conversion processes in different types of electric discharge plasmas, although the early results obtained in microwave discharges (demonstrating 80-90% energy efficiency [31,32]) have not been reproduced. In addition, significant advances have been made in the experimental characterization of CO_2-containing plasmas and the state-specific kinetic modeling of the energy transfer and chemical reactions. An extensive authoritative review of the recent work, incorporating the experimental methods, diagnostic techniques, and kinetic modeling approaches, is given in [33]. One of the critical issues affecting the energy efficiency of CO_2 conversion in the plasma is whether the dissociation occurs via the vibrationally enhanced "ladder climbing" mechanism driven by the anharmonic vibration-vibration (V-V) pumping, or via the excitation of CO_2 electronic states by electron impact [31]. The energy required for dissociation in the former process is much lower, resulting in the higher efficiency of CO2 conversion in microwave and RF discharges, compared to dielectric barrier discharges (DBD) at the same specific energy input [31,34,35].

Since nitrogen is often present in CO_2-containing gas mixtures, e.g. in combustion exhaust flows, feasibility of CO_2 dissociation in nonequilibrium CO_2-N_2 mixtures has been studied in a microwave discharge and analyzed by state-specific kinetic modeling [36]. The rate of vibration-translation (V-T) relaxation of nitrogen is much slower compared to that of carbon dioxide, such that it can be used as a vibrational energy reservoir, sustaining CO_2 vibrational excitation by the rapid V-V energy transfer to the CO_2 asymmetric stretch mode ($\nu3$), as occurs in CO_2 lasers. The results of Ref. [36] indicate that adding nitrogen does increase the CO_2 conversion, although the overall energy efficiency still decreases due to the lower CO_2 fraction in the mixture.

Isolating different kinetic mechanisms of CO_2 dissociation in the plasma requires (i) varying the energy input into vibrational energy modes, without significant change in the rates of electronic excitation and molecular dissociation by electron impact, and (ii) time-resolved measurements of CO_2 vibrational level populations and CO number density. The feasibility of this approach has been demonstrated recently in a “hybrid” electric discharge sustained in nitrogen and its mixtures with H_2, CO, and CO_2 by using a combination of high peak voltage, ns pulse duration pulse train and a lower voltage, sub-breakdown RF bursts between the pulses [37]. In this type of discharge, ionization is produced by the ns pulses while most of vibrational excitation occurs at a much lower reduced electric field applied by the RF waveform, which does not generate additional ionization. The total energy coupled to the plasma is varied by changing the number of pulses in the train. The use of a ns pulse train adding energy to a large-volume plasma on a ms time scale, instead of a smaller size plasma generated by a single ns pulse discharge [38], does not require the ns time resolution of the diagnostics and reduces the effect of compression waves generated by the rapid heating of the plasma on a sub-μs time scale [39]. In the present work, time-resolved CO_2 and CO vibrational populations in the plasma are monitored by the high-resolution mid-IR absorption spectroscopy, using a tunable Quantum Cascade Laser (QCL). Similar diagnostics were employed recently in a pulsed DC glow discharge [40] and a single-pulse ns discharge [38]. The use of QCL absorption spectroscopy for CO_2 and CO vibrational population measurements is complementary to in situ step-scan FTIR spectroscopy [41]. Step-scan FTIR spectra can be used to infer time-resolved, non-Boltzmann populations of multiple vibrational states [42]. However, multiple overlapping vibrational bands detected at relatively low spectral resolution, ~ 0.1 cm^{-1}, make the inference of the high vibrational level populations of polyatomic molecules rather challenging and limits the sensitivity of the measurements. To quantify the energy transfer from nitrogen to carbon dioxide in CO_2-N_2 mixtures, the nitrogen vibrational temperature is measured by the broadband vibrational CARS [37].

The principal objectives this present work are to (i) quantify the rate of CO_2 dissociation in the ns pulse plasma, and (ii) obtain time-resolved data on N_2 vibrational temperature, CO_2 vibrational level populations, CO number density, and gas temperature at these conditions, for validation of the state-specific kinetic models.

Chapter 2: Atmospheric Pressure Plasma Jet

2.1 Experimental Setup

To study vibrational excitation of nitrogen, a quasi-two-dimensional atmospheric pressure plasma jet assembly was studied, as shown in Fig. 2-1. A mixture of nitrogen and inert gas diluent (argon, helium, or neon) is flowing through a 3 mm x 50 mm rectangular cross section glass channel with the wall thickness of 2 mm (VitroCom RT0350). The channel is fused to an 8 mm internal diameter glass tube, via an adapter channel 25 mm long and expansion angle of 45^0, as shown in Fig. 2-1. A 7 cm long ABS plastic plug on the top of the glass tube, with a 1/8 inch diameter port in the center, serves as a high-voltage electrode feedthrough. The flow enters the tube 7.25 cm below the electrode feedthrough, through a ¼ inch diameter tube connected to the delivery line via a plastic Swagelok fitting. The nitrogen and inert diluent flow rates, with the total flow rate maintained at 2-3 SLM, are measured by MKS 1179A mass flow controllers.

The high-voltage lead is a brass rod 1/8 inch in diameter, with a threaded top part used to control the vertical position of the electrode in the channel. The high-voltage electrode, a 40 mm x 15 mm rectangular brass plate 1 mm thick, with rounded edges, is soldered to the slotted end of the lead using a silver-based solder, and positioned in the center of the channel. The use of a high melting temperature solder is critical for operation of the RF plasma jets at a relatively high discharge power, exceeding ~100 W. In the present experiments, the lower edge of the high-voltage electrode is maintained either 10 mm or 3 mm above the channel exit, for the ns pulse and RF-powered plasma jets respectively. The grounded electrode is an adhesive copper tape 13 mm wide, wrapped around the outside perimeter of the glass channel, with the lower edge 8.6 mm above the channel exit, as shown in Fig. 2-1. The flow exiting the channel is impinging on a horizontal glass plate 1.7 mm thick (for a ns pulse discharge) or quartz plate 1.4 mm thick (for the RF discharge), with a rectangular grounded electrode 26 mm x 90 mm, made of adhesive copper tape, attached to the bottom of the plate. The target plate was placed 5 mm (for a ns pulse discharge) or 2.5 mm (for the RF discharge) below the exit plane of the flow channel.

The flow channel is placed inside a co-flow assembly, with a 23 mm x 70 mm rectangular cross section co-flow channel. The assembly is made of two identical plastic parts using 3-D printing, with a rubber gasket between them, as shown in Figure 2-1. The co-flow enters the 8.5 mm inside diameter channels on two sides of the assembly, connected to the split delivery line via two UltraTorr vacuum fittings. The flow is then injected into the co-flow channel via 1 mm diameter injection ports, 6 on each side. The flow rate, 20 SLM, is measured by a MKS 1179A mass flow controller. A 3-D printed honeycomb plug 30 mm long and with the hole diameter of 1.5 mm, with a rectangular shape opening for the main flow channel, is placed in the housing 3 cm below the injection ports, to serve as the co-flow straightener. The exit plane of the main flow channel is aligned with the exit plane of the co-flow channel. The co-flow (dry air or oxygen) prevents the plasma jet perturbation by the ambient air convection in the room, as well as the flashover between the high-voltage electrode and the grounded electrode along the channel surface. In the present experiments with a ns pulse plasma jet, the oxygen co-flow also greatly reduces the “stray” CARS signal from nitrogen in the ambient air surrounding the plasma jet.

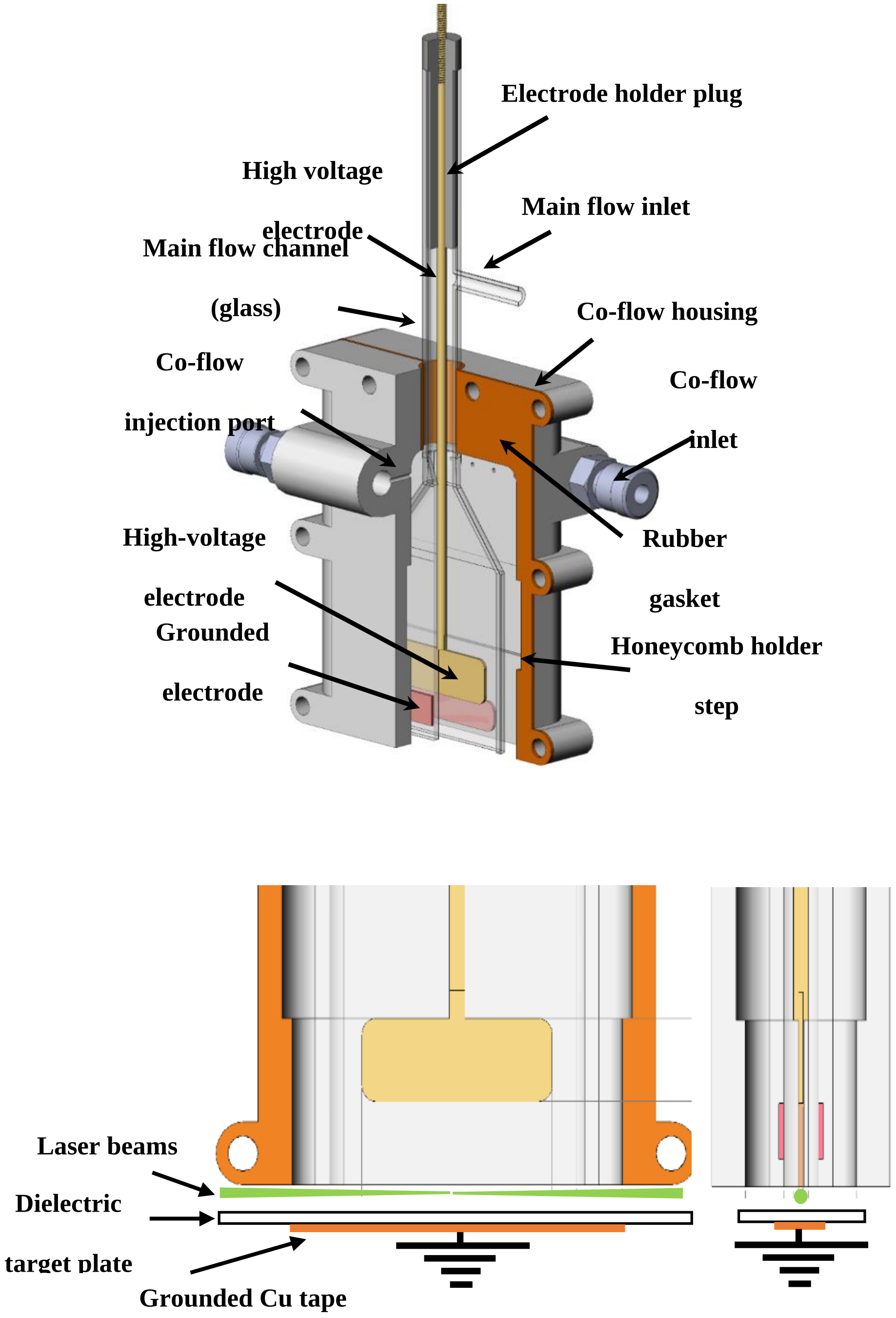

Figure 2 - 1 (a) Schematic of the 2-D plasma jet assembly; (b) schematic of the plasma jet electrodes.

The repetitive burst discharge in the main flow channel is sustained (i) by a custom-made, alternating polarity high-voltage pulse generator (pulse peak voltage 12 kV, pulse duration 100 ns, pulse repetition rate 10 kHz, 200 pulses in a burst, duty cycle 20%), or (ii) by an ENI ACG-6B RF plasma generator with an MFJ-989D impedance matching tuner (frequency 13.56 MHz, peak voltage 1 kV, burst duration 30 ms, duty cycle 30%). In both cases, the burst repetition rate is kept at 10 Hz, to match the laser pulse repetition rate. The ns pulse discharge is sustained in gas mixtures with 20-40% N_2, and the RF discharge is sustained in gas mixtures with 2.8-7.0% N_2. Further increase of the nitrogen fraction in the mixture results in the intermittent breakdown, particularly by the RF waveforms. The pulse voltage and current waveforms are measured by a Tektronix P6015A high-voltage probe and a Pearson 2877 current monitor. Broadband plasma emission images are taken using a gated PI-MAX 3 ICCD camera with a UV lens.

Vibrational level populations of nitrogen in the ground electronic state are measured by broadband N_2 vibrational CARS, discussed in detail in [43]. Briefly, 80% of the second harmonic output of an externally triggered, injection-seeded, ns Nd:YAG laser (Surelite, SLIII-10) is used to pump a custom-built broadband dye laser to generate the Stokes beam with the FWHM of 6 nm, centered at 605 nm. In the present work, the oscillator cavity of the dye laser is intentionally misaligned slightly to reduce the etalon fringes in the broadband output, which affect the detection limit of the vibrational populations inferred from the CARS spectra. The rest of the Nd:YAG laser output is used as the CARS pump/probe beam. The pulse energies of the pump/probe and the Stokes beams are 17 mJ and 12 mJ, respectively. Both beams are vertically polarized. The two beams are combined using a delay line and dichroic mirrors, and focused in the test section by a 22 cm focal distance lens, in collinear phase matching geometry. The CARS signal generated in the test section is separated from the pump and Stokes beams using dichroic mirrors and detected by an Andor 750 spectrometer with Andor EMCCD camera. The resolution of the broadband CARS spectra is dominated by the spectrometer instrument function, approximately 10 pm (0.4 cm^{-1}) FWHM. N_2 vibrational and rotational-translational temperature are inferred from the CARS spectra using a CARSFT program [44], modified to infer these parameters independently.

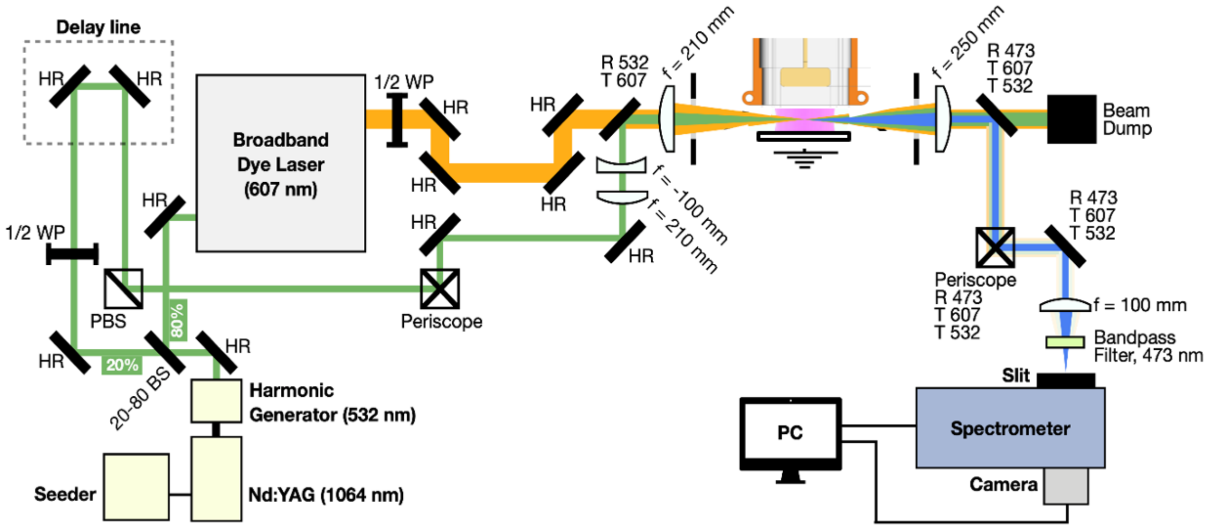

Figure 2 - 2: Optical Layout for CARS Diagnostic

The use of CARS for the N_2 vibrational population measurements at the present conditions is challenging, due to the relatively low concentration of nitrogen in the jet. Although the collinear laser beam geometry greatly increases the CARS signal, the contribution of nitrogen in ambient air into the $N_2(v=0)$ CARS signal may still be significant. In the ns pulse plasma jet, this “stray” CARS signal was suppressed by using a pure oxygen co-flow. In the RF plasma jet, operated with much lower N_2 fractions, this suppression was not sufficient. In this case, the

N_2(v=0) signal was ignored in the data reduction, and vibrational level populations and rotational temperature were inferred using the signal from N_2(v>1) bands.

2.2 Kinetic Model

The quasi-zero-dimensional kinetic model is described in detail in our previous work [45,46]. Briefly, the model solves the electron energy equation (a moment of the Boltzmann equation), the heavy species energy equation, and equations for the species concentrations. The model incorporates the electron impact ionization, dissociation, electronic excitation, and vibrational excitation processes; energy transfer among the excited electronic states of Ar and N_2; and N_2 vibrational relaxation (state-specific vibration-vibration energy transfer for N_2-N_2 and vibration-translation relaxation for N_2-N, N_2-N_2, and N_2-Ar). The time-resolved discharge power waveform, used as an input in the model, is obtained from the experimental discharge voltage and current waveforms. The electron impact rate coefficients are predicted by the Boltzmann equation solver Bolsig+ [47,48]. The rates of energy transfer among the electronically excited Ar and N_2 are taken from [25,49-52]. Vibration-vibration (V-V) and vibration-translation (V-T) rates for N_2-N_2 are taken from [53] and [54], respectively. The V-T rates for N_2-Ar are assumed to be the same as the rates for N_2-N_2. For N_2-N, the V-T rates are predicted in [55], including the multi-quantum transitions. To quantify the effect of N_2-N_2 and N_2-Ar V-T rate uncertainty on the modeling predictions, the model was exercised using two different sets of rates, one predicted in [54] and the other in [56] (Pot II). Finally, the rates for V-V energy transfer between the first excited state and ground state of nitrogen, $A^3\Sigma_g^+$ and $X^1\Sigma_g^+$, are taken from [26]. A brief summary of the vibrational energy transfer rate coefficients, which have the most significant effect on the modeling predictions, is given in Appendix D.

The entry parameters of the model include the discharge input power waveform, flow rate, pressure, and estimated plasma volume. Wall heat transfer and diffusion are taken into account as approximate quasi-zero-dimensional corrections.

2.3 Results and Discussion

Figure 2-3 plots the voltage and current waveforms in the 20% N_2-Ar plasma, for positive and negative ns pulse polarities. In the ns pulse burst, the odd pulses are positive polarity and the even pulses are negative polarity. It can be seen that the waveforms are similar to each other, with the negative polarity peak current being somewhat higher. The waveforms taken in the N_2-He plasma are nearly identical to the ones shown in Fig. 2-3. The coupled pulse energy for the positive and negative polarity pulses, 4.0 and 3.0 mJ, respectively, remains approximately the same during the entire burst.

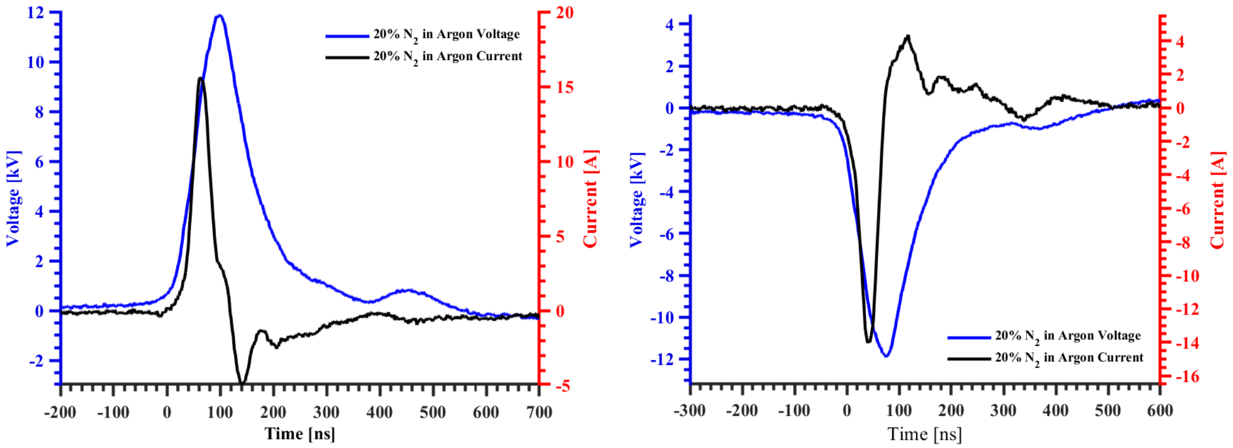

Figure 2 - 3 : Typical ns discharge current and voltage waveforms in a 20% N_2-Ar mixture: (a) positive polarity, (b) negative polarity.

Figure 4 shows the broadband plasma emission images, both single-pulse and 100-pulse accumulations, taken during a 200-pulse ns discharge burst in 20% N_2 / He and 20% N_2 / Ar mixtures. A cartoon schematic of the jet channel exit, the target plate, and the laser beam (nearly to scale), as well as the spatial distribution of the CARS signal measured by traversing a 1 mm thick glass plate across the laser beam, are also shown in Fig. 2-4. Similar to our previous work in a ns pulse discharge sustained in ambient air, using the same pulse generator [57], the negative polarity pulses appear significantly more diffuse and less filamentary compared to the positive polarity pulses, with the exception of pulses #1 and #2. In N_2-He, the plasma also gradually becomes more diffuse during the burst (see Figure 2- 4(a)). In N_2-Ar, the plasma generated by the positive polarity pulses remains filamentary for the entire duration of the burst, although the negative polarity pulses generate diffuse plasma (see Figure 2-4(b)).

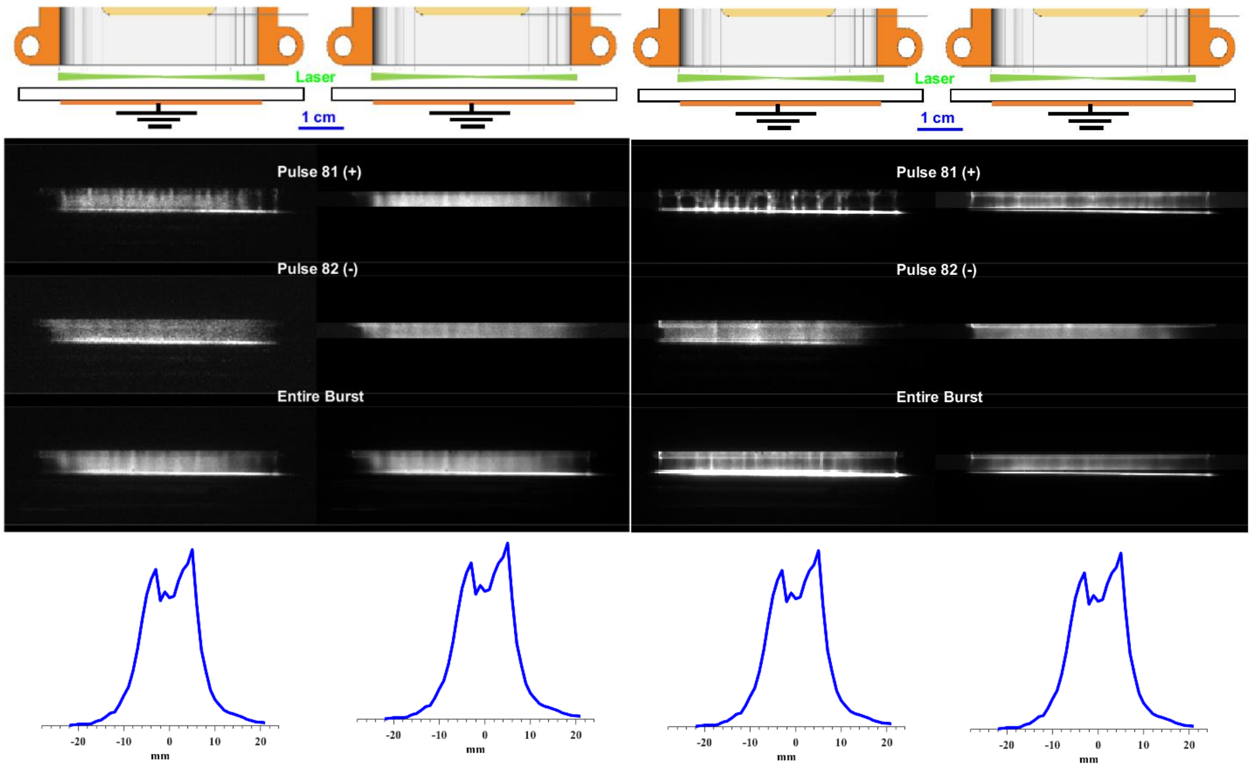

Figure 2 - 4: ICCD images of a ns pulse discharge burst: (a) single shot, 1 μs gate (left column), and 100-shot accumulation (right column), 20% N_2 / He; (b) single shot, 1 μs gate (left column), and 100-shot accumulation (right column), 20% N_2 / Ar. Pulse number in the burst and pulse polarity are indicated next to the images. CARS signal distribution is plotted below the images.

The formation of filaments in the ns pulse discharge does not preclude using the collinear geometry CARS spectra for characterization of the vibrational nonequilibrium in the plasma, for two reasons. First, as will be shown later, N_2 vibrational excitation produced by individual discharge pulses is relatively low, less than 1 meV/molecule, such that the net vibrational excitation is the result of accumulation over multiple pulses during the burst. Second, the filaments generated during the individual positive polarity pulses are random, which is illustrated by the 100-pulse accumulation images and a plasma image accumulated over the entire burst in Fig. 2-4. Therefore, the CARS spectra (which are averages of 100 shots), with 95% of the signal collected over approximately 20 mm along the laser beam (see Fig. 4), provide an adequate representation of vibrational excitation in the plasma, accumulated gradually during the discharge burst.

Figure 2-5 compares typical experimental CARS spectra, taken 5 ms after the end of a 200-pulse discharge burst in a 20% N_2/Ar mixture, and 5 ms after the beginning of a 200-pulse discharge burst in a 40% N_2/Ar mixture, with best fit synthetic spectra generated by CARSFT. It can be seen that the spectra exhibit good agreement. In the 20% N_2/Ar mixture, N_2(v=0-2) bands are identified (see Fig. 5(a)). Comparison of the CARS spectra taken with and without nitrogen in the main flow shows that the contribution of the signal from the N_2(v=0) band in ambient air surrounding the jet and the co-flow is insignificant, and does not exceed 2-3% of the N_2(v=0) signal from nitrogen in the jet. Therefore, the intensities of N_2(v=0-2) bands have been used to infer the N_2 vibrational temperature at these conditions, $T_v = 1530 \pm 70$ K. The rotational structure of the Q-branch of the v=0 band is used for the translational-rotational temperature inference, $T = 370 \pm 10$ K. The CARS spectrum taken in the 40% N_2/Ar mixture, plotted in Fig. 5(b) on a semilog scale, illustrates the detection limit of the v=1 band and the sensitivity of the present N_2 vibrational temperature measurements, $T_v \approx 600$ K. Several strong lines from the O-branch of the v=0 band are also visible in Fig. 5(b). Both spectra in Fig. 2-5 exhibit significant non-resonant background, primarily from argon (Fig. 2-5(a)) and also from nitrogen (Fig. 2-5(b)). When the resonant CARS signal intensity is comparable with the non-resonant background, noticeable “dips” appear on the violet side of the Q-branch features and O-branch lines (e.g. v=1,2 in Fig. 2-5(a) and v=0, J″=4-10 in Fig. 2-5(b)). In this case, the resonant signal detracts from the non-resonant background [58]. When the resonant signal intensity greatly exceeds the non-resonant background, this effect becomes much weaker, such that it is most pronounced in N_2-Ar mixtures with the low nitrogen mole fractions.

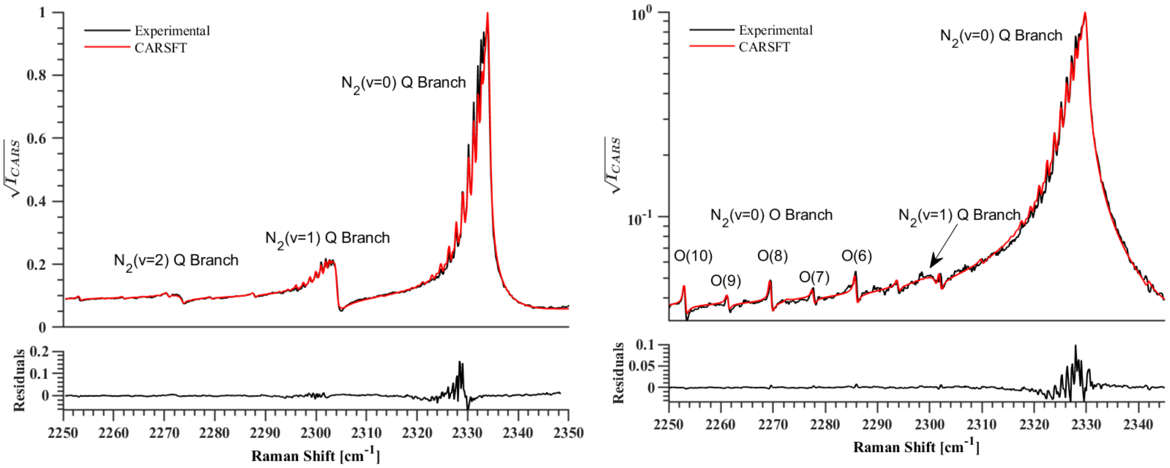

Figure 2 - 5: Typical experimental and best fit synthetic CARS spectra in a ns pulse discharge burst: (a) 20% N_2/Ar mixture, T = 370 ± 10 K, T_v = 1530 ± 70 K; (b) 40% N_2/Ar mixture, plotted on a semi-log scale to illustrate the detection limit of N_2(v=1) band and indicate the presence of O-branch transitions, T = 330 ± 10 K, T_v = 615 ± 70 K.

Time-resolved translational-rotational temperature and N_2 vibrational temperature during and after a 200-pulse discharge burst in N_2/Ar and N_2/He mixtures are plotted in Figs. 2-6, 2-7. It can be seen that in both cases, the temperature rise during the burst is relatively modest, not exceeding $\Delta T = 80$ K (see Figs. 2-6(a), 2-7(a)). Reducing the nitrogen mole fraction increases the temperature rise in the jet, indicating that a smaller fraction of the discharge input energy is stored in the N_2 vibrational mode. However, the specific vibrational energy loading per N_2 molecule increases as the nitrogen fraction in the mixture is reduced (see Figs. 2-6(b), 2-7(b)). In N_2/Ar mixtures, the nitrogen vibrational temperature increases steadily during the burst, and exceeds T_v = 1500 K by the end of the burst in a 20% mixture (see Fig. 2-6(b)). In contrast, the vibrational temperature measured in N_2/He mixtures levels off during the burst, at T_v = 1100-1150 K in a 20% mixture (see Fig. 2-7(b)). Significantly lower vibrational temperatures measured in N_2/He mixtures are most likely due to the faster V-T relaxation for N_2-He, compared to that for N_2-N_2 or N_2-Ar, $k_{10}(N_2\text{-}He) = 5\cdot10^{-18}$ cm^3/s [43] vs. $k_{10}(N_2\text{-}N_2) < 6\cdot10^{-21}$ –

$3.7\cdot10^{-20}$ cm^3/s ([40] and references therein) at room temperature. After the burst, the vibrational temperature decreases to near detection limit over 70 ms in a 20% N_2-Ar mixture (see Fig. 2-6(b), most likely controlled by convection with the flow), and within 10 ms in a 20% N_2-He mixture (consistent with the N_2-He V-T relaxation rate).

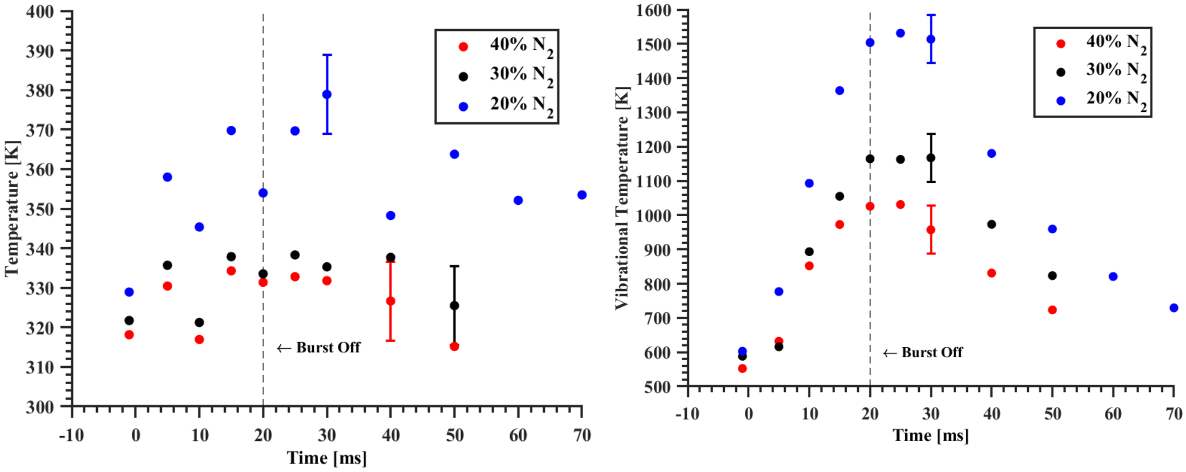

Figure 2 - 6: Time evolution of (a) gas temperature, and (b) N_2 vibrational temperature during and after a 200-pulse discharge burst in N_2/Ar mixtures.

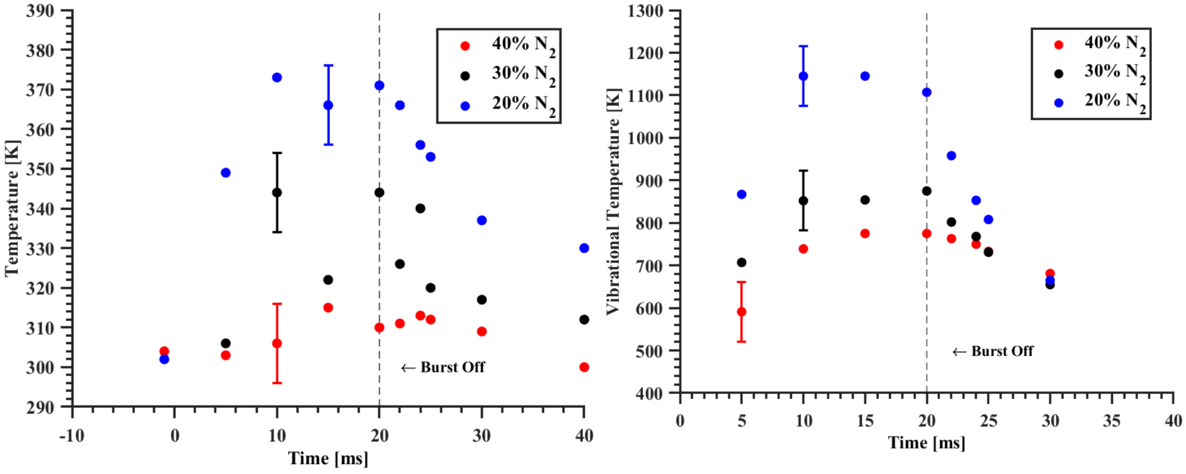

Figure 2 - 7: Time evolution of (a) gas temperature, and (b) N_2 vibrational temperature during and after a 200-pulse discharge burst in N_2/He mixtures.

The gradual rise of the vibrational temperature during the burst shows that the vibrational excitation produced by the individual discharge pulses is very low, approximately 0.1 meV/pulse. Therefore, the random filaments generated in the positive polarity pulses during the burst (see Fig. 4) are unlikely to perturb the vibrational energy distribution along the plasma (in the direction of the laser beam). Thus, the collinear CARS spectra, taken at a relatively long interaction length (95% of the signal originating within 20 mm) provide an adequate measurement of N_2 vibrational excitation accumulated over multiple discharge pulses.

As expected, N_2 vibrational excitation sustained in a ns pulsed discharge remains relatively low, both due to the low time-averaged discharge power (approximately 35 W during the burst), and because the energy is coupled to the plasma at high values of the reduced electric field (E/N), which greatly reduces the energy fraction going to N_2 vibrational excitation by electron impact. To enhance the vibrational nonequilibrium in the plasma jet, the discharge electrodes were powered by an RF waveform. At these conditions, peak applied voltage is over an order of magnitude lower compared to that in a ns pulse discharge (see Fig. 2-3), while the time-averaged discharge power increases to 130-180 W. To prevent overheating of the discharge electrodes, the RF discharge was sustained at a 30% duty cycle, with the RF burst duration of 30 ms. Figure 2-8 shows the RF discharge voltage and current in mixtures of nitrogen with helium and argon, both with 4% N_2 mole fraction. The time-averaged RF discharge power coupled to the load, 130 W in N_2 – He and 180 W in N_2 – Ar, is calculated from these waveforms. The waveforms and the coupled power in the 4% N_2-Ne mixture are similar to those measured in N_2-Ar.

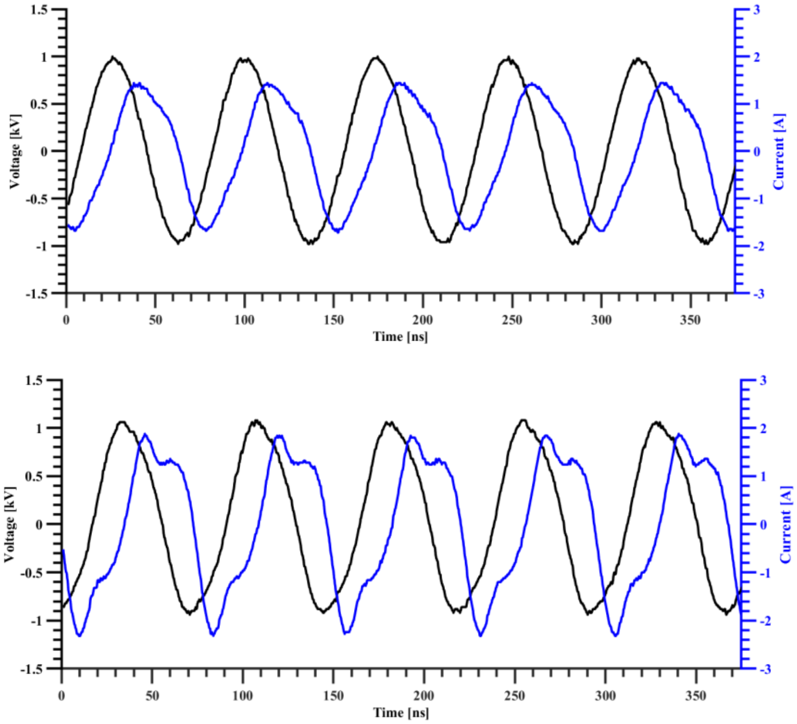

Figure 2 - 8: RF discharge voltage and current waveforms: (a) 4% N_2 – He (time-averaged power 130 W) and (b) 4% N_2 - Ar (180 W).

The plasma emission images in the RF discharge are shown in Fig. 2-9. Although RF plasmas sustained in pure argon, helium, and neon are diffuse and uniform, adding several percent of nitrogen results in the development of multiple diffuse filaments, which may affect the result of the present measurements, taken at a relatively low spatial resolution in the direction of the beam. The "end view" images indicate that the plasma jet remains diffuse. The laser beam was positioned approximately 300 μm below the channel exit, as illustrated schematically in Fig. 2-9, such that the measurements are made in the jet core flow, to minimize the effect of the vibrational energy transfer to the oxygen co-flow.

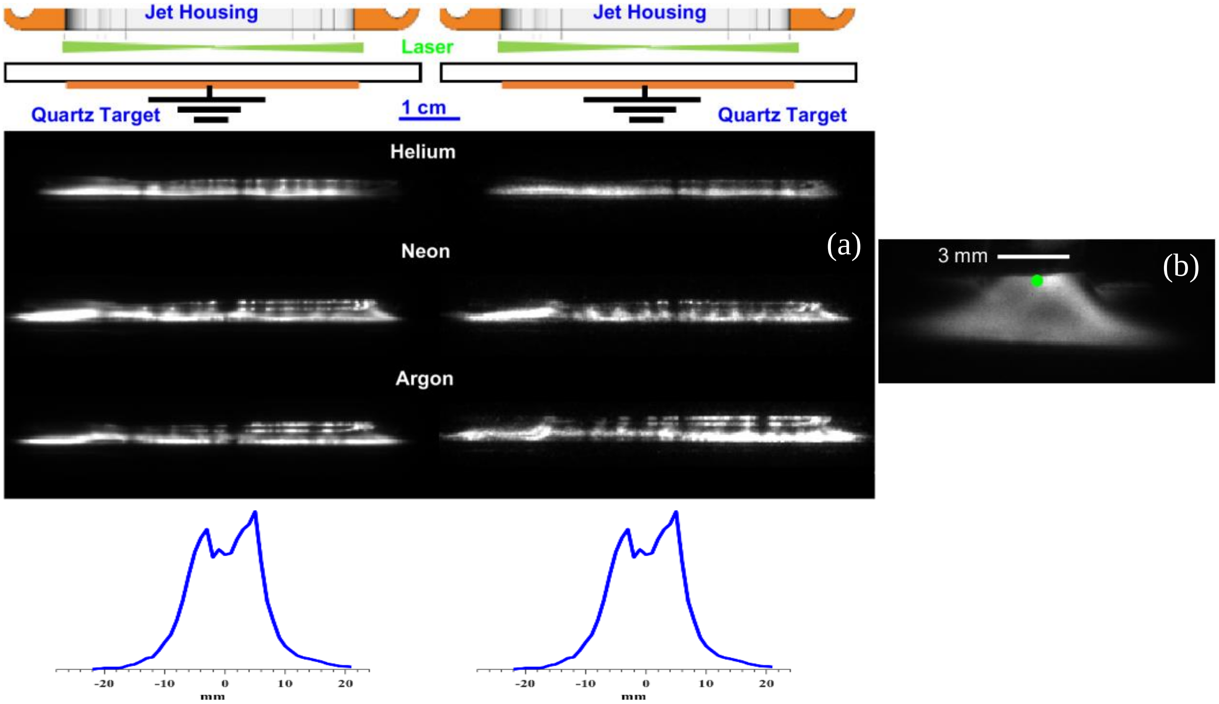

Figure 2 - 9: (a) ICCD images of RF plasma jets in helium, neon, and argon-based mixtures, each with 4% mole fraction of nitrogen (side view). Left column: camera gate 30 ms, right column: camera gate 100 µs, 1 ms after the discharge initiation. CARS signal distribution is plotted below the images. (b) ICCD image of the RF plasma jet in 4% N_2/He (end view), camera gate 30 ms.

During the CARS measurements in the RF plasma jet, the nitrogen fraction in the flow was reduced considerably compared to that in the ns pulse discharge, from 20-40% to 2.8-7.0%, to produce consistent breakdown during each RF discharge burst, at a relatively low peak voltage. At these conditions, the CARS signal from the plasma jet is 1-2 orders of magnitude lower compared to that in the jet excited by a ns pulse discharge. Therefore, the CARS signal from the N_2(v=0) band in ambient air becomes comparable, or sometimes even dominates, the N_2(v=0) signal from the jet. This is illustrated in Fig. 2-10, which plots the entire N_2 CARS spectrum taken in an RF discharge in a 6% N_2/Ne mixture. Turning the N_2 flow on and off indicated that the majority of the v=0 band signal originated outside the jet, such that it cannot be used for the data analysis. However, the spectral resolution and the signal-to-noise ratio in the rest of the spectrum are sufficiently high to circumvent this difficulty. This is illustrated in Fig. 10, which plots $N_2(v\geq1)$ CARS spectra taken in 6% N_2/Ne and 6% N_2/Ar mixtures. These spectra, acquired at the end of a 30 ms RF discharge burst, exhibit the presence of $N_2(v=1\text{-}6)$ vibrational bands, indicating strong vibrational excitation.

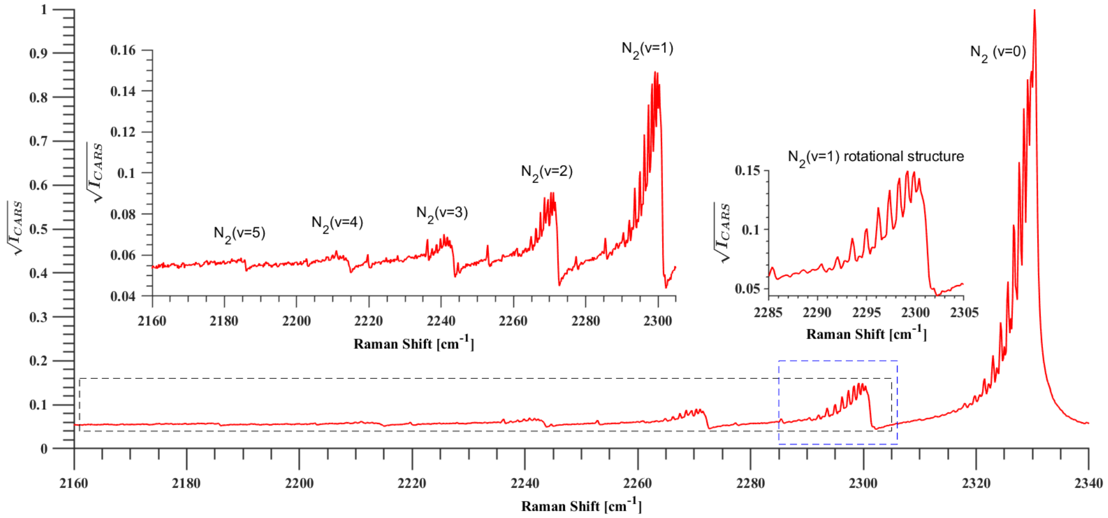

Figure 2 - 10: Entire N_2 CARS spectrum taken in an RF discharge in a 6% N_2/Ne mixture, illustrating a significant contribution of N_2 in ambient air into $N_2(v=0)$ signal, which was removed for the data processing. The dashed line boundaries (also shown as insets) indicate the regions used for the vibrational and rotational temperature inference.

As expected, the N_2 vibrational temperatures in the RF discharge, inferred from comparison with the best fit CARSFT spectra for $N_2(v=1\text{-}6)$ vibrational bands are much higher compared to those measured in a ns pulse discharge, $T_v(N_2) = 3370 \pm 200$ K in N_2-Ne and $T_v = 3680 \pm 200$ K in N_2-Ar. The N_2-Ar spectrum exhibits a modest overpopulation of vibrational levels v=3-5, compared to the CARSFT spectrum (see Fig. 10(a)), indicating the effect of anharmonic V-V pumping. Translational-rotational temperatures, inferred from the rotational structure of the v=1 band, are also significantly higher compared to that in a ns pulse discharge, $T = 675 \pm 15$ K and $T = 725 \pm 25$ K, respectively, due to the higher RF discharge power. Again, well-pronounced “dips” appear on the violet side of N_2 vibrational band heads, especially noticeable in Ar (see Fig. 2-11(a)), which has a third-order susceptibility over an order of magnitude higher compared to that of Ne [60]. Acquiring the high signal-to-noise CARS data in N_2/He mixtures with low nitrogen fractions proved challenging, due to the strong optical emission from helium near the anti-Stokes wavelengths. CARS spectra taken in 3% N_2/Ne and 3% N_2/Ar mixtures, plotted in Fig. 2-12, exhibit even stronger N_2 vibrational excitation, with $T_v = 4265 \pm 250$ K and $T_v = 5100 \pm 150$ K, respectively. However, the signal to noise at these conditions becomes significantly lower, such that no data were taken at lower N_2 fractions in the flow.

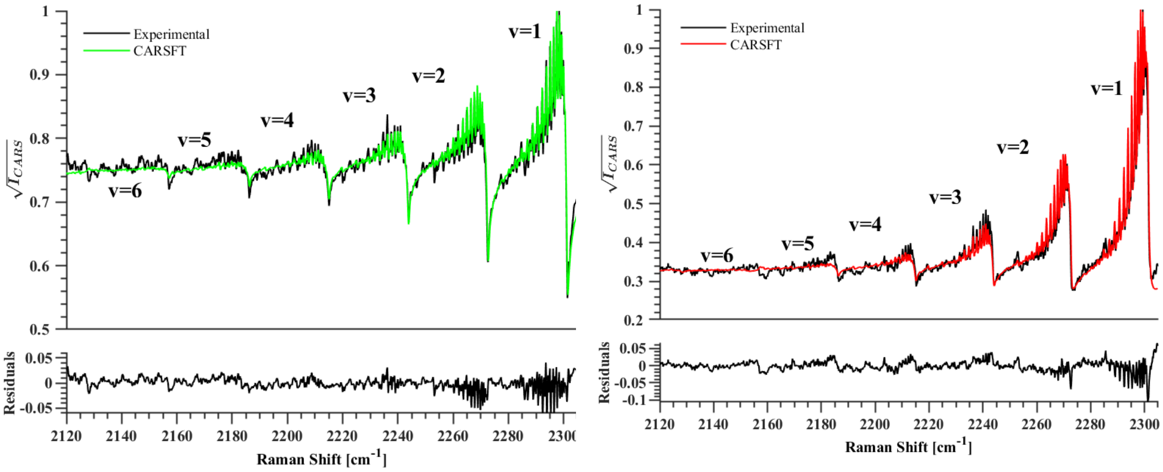

Figure 2 - 11: N_2 CARS spectra acquired at the end of a 30 ms RF discharge burst, exhibiting the presence of N_2(v=1-6) vibrational bands, and best fit synthetic spectra: (a) 5% N_2/Ar, (b) 5% N_2/Ne. Inferred rotational and vibrational temperatures are $T = 725 \pm 25$ K, $T_v = 3680 \pm 200$ K, and $T = 675 \pm 15$ K, $T_v = 3370 \pm 200$ K, respectively. Overpopulation of v=3-5, relative to the Boltzmann distribution, is apparent.

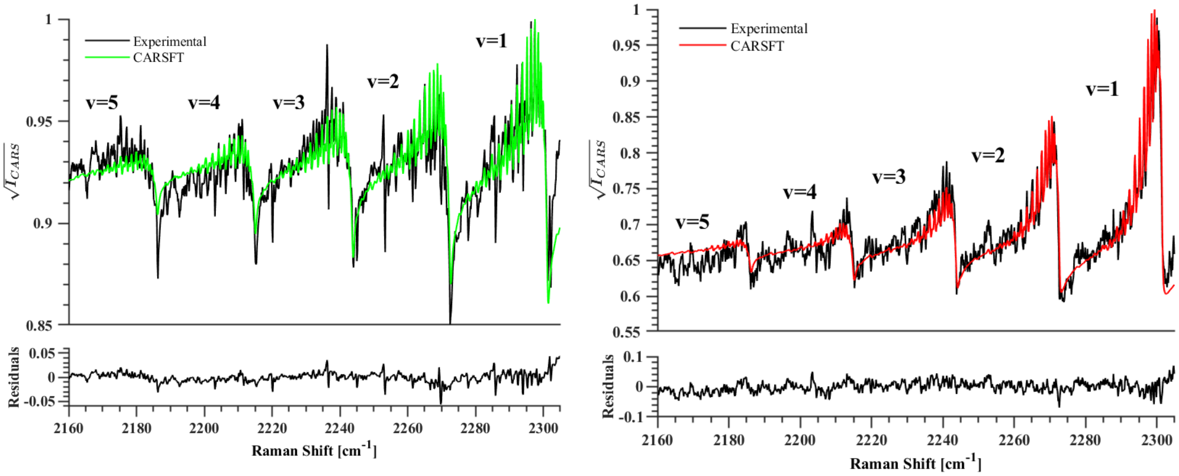

Figure 2 - 12: N_2 CARS spectra acquired at the end of a 30 ms RF discharge burst, exhibiting $N_2(v=1\text{-}5)$ vibrational bands, and best fit synthetic spectra: (a) 3% N_2/Ar, (b) 3% N_2/Ne. Inferred rotational and vibrational temperatures are T = 885 ± 30 K, T_v = 5100 ± 150 K, and T = 575 ± 12 K, T_v = 4265 ± 150 K, respectively.

Translational-rotational and vibrational temperatures inferred from the CARS spectra indicate that they rapidly reach near steady state and remain approximately constant during the RF discharge burst (see Fig. 2-13). After the burst, vibrational excitation decays on a ~10 ms time scale, which may be affected both by the V-T relaxation and convection with the flow. Vibrational temperature measured at the end of the discharge burst decreases significantly as the N_2 fraction in the mixture is increased from 3% to 5%, after which it begins to rise again (see Fig. 2-14). This behavior is observed both in N_2/Ne and N_2/Ar mixtures. Somewhat surprisingly, the translational-rotational temperature exhibits the opposite trends in N_2/Ne mixtures, where it increases with the nitrogen fraction, and N_2/Ar mixtures, where it decreases.

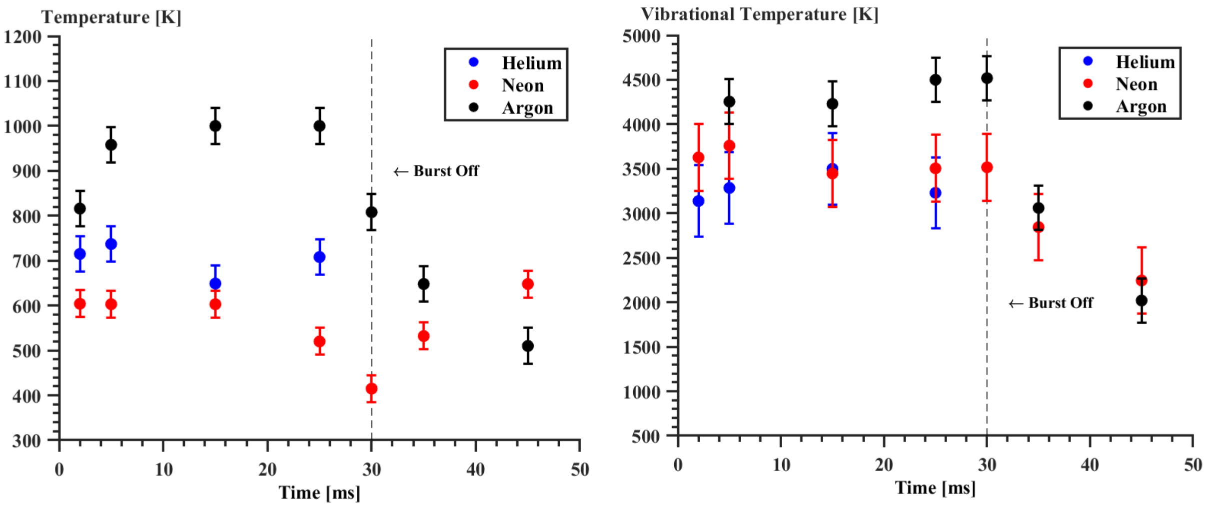

Figure 2 - 13: (a) N_2 translational-rotational temperature, (b) N_2 vibrational temperature measured during and after a 30 ms RF discharge burst in 4% N_2 / noble gas mixtures.

To understand the kinetics of N_2 vibrational excitation at the present conditions, we used kinetic modeling of energy transfer in N_2/Ar mixtures excited by the RF discharge. The major inelastic electron impact collision processes dominating the energy partition in the discharge include vibrational excitation of the ground electronic state N_2,

$$N_2(X^1\Sigma_g^+, v=0) + e^- \rightarrow N_2(X^1\Sigma_g^+, v) + e^-, \tag{2-1}$$

electronic excitation of N_2,

$$N_2(X^1\Sigma_g^+) + e^- \rightarrow N_2(A^3\Sigma_u^+, B^3\Pi_u, C^3\Pi_g, a'^1\Sigma_u^-) + e^-, \tag{2-2}$$

dissociation,

$$N_2(X^1\Sigma_g^+) + e^- \rightarrow N + N + e^-, \tag{2-3}$$

and electronic excitation of Ar,

$$Ar + e^- \rightarrow Ar^* + e^-\ , \tag{2-4}$$

where the notation Ar* is used for a group of excited electronic states near 11.5 eV, Ar($3p^5 4s$). Higher vibrational levels of $N_2(X^1\Sigma_g^+)$ are also populated by the anharmonic V-V pumping,

$$N_2(v) + N_2(w) \rightarrow N_2(v-1) + N_2(w+1)\ , \tag{2-5}$$

and depopulated by the V-T relaxation by N atoms, Ar atoms, and N_2 molecules,

$$N_2(v) + M \rightarrow N_2(w) + M\ . \tag{2-6}$$

Since the collisional quenching of metastable Ar($3p^5 4s$) atoms by argon is relatively slow, rapid energy transfer to electronic states of N_2 also contributes to their excitation,

$$Ar^* + N_2 \rightarrow Ar + N_2(A^3\Sigma_u^+, B^3\Pi_u, C^3\Pi_g)\ , \tag{2-7}$$

followed by the cascade radiative decay and collisional quenching of $C^3\Pi_g$ and $B^3\Pi_u$ and states to $A^3\Sigma_u^+$,

$$N_2(C^3\Pi_g) + N_2 \rightarrow N_2(B^3\Pi_u) + N_2 \rightarrow N_2(A^3\Sigma_u^+,v) + N_2\ . \tag{2-8}$$

The nascent vibrational distribution of $N_2(A^3\Sigma_u^+,v)$ generated during the quenching is assumed to be the same as in our previous work [45]. The $N_2(A^3\Sigma_u^+,v)$ decay processes are dominated by the energy pooling

$$N_2(A^3\Sigma_u^+,v) + N_2(A^3\Sigma_u^+,w) \rightarrow \begin{cases} N_2(B^3\Pi_g) + N_2(X^1\Sigma_g^+) \\ N_2(C^3\Pi_u) + N_2(X^1\Sigma_g^+) \\ N(^4S) + N(^4S) + N_2(X^1\Sigma_g^+) \end{cases}\ , \tag{2-9}$$

quenching by N atoms,

$$N_2(A^3\Sigma_u^+, v) + N \rightarrow N_2(X^1\Sigma_g^+) + N \ , \tag{2-10}$$

generated both by the electron impact dissociation and by the energy pooling [45,46], and quenching by the vibrationally excited molecules in the ground electronic state,

$$N_2(A^3\Sigma_u^+,v) + N_2(X^1\Sigma_g^+, w \geqslant 6) \rightarrow N_2(B^3\Pi_u) + N_2(X^1\Sigma_g^+, w=0) \ . \tag{2-11}$$

Finally, V-V energy exchange of $N_2(A^3\Sigma_u^+)$ with the ground electronic state N_2 also results in its vibrational excitation [26,45], in addition to electron impact,

$$N_2(A^3\Sigma_u^+,v) + N_2(X^1\Sigma_g^+, w=0) \rightarrow N_2(A^3\Sigma_u^+, v\text{-}2) + N_2(X^1\Sigma_g^+, w=1) \ . \tag{2-12}$$

Figure 2-14 compares the "first level" N_2 vibrational temperature, $T_v = \frac{\omega_e(1-2x_e)}{\ln\left(\frac{f_0}{f_1}\right)}$, and the translational-rotational temperature predicted by the model with the experimental data. It can be seen that the model is consistent with the experimental results indicating strong vibrational nonequilibrium, although the N_2 vibrational temperature is overpredicted, while the predicted gas temperature is within the uncertainty of the data with the exception of one data point at 6.7% N_2. At these conditions, most of the discharge input energy goes to electronic excitation of Ar, with the subsequent energy transfer to the electronic states of N_2. However, the energy transfer from the electronically excited N_2 molecules to the vibrational excitation of the ground electronic state (specifically the process of Eq. (2-12)) is of minor importance compared to the direct vibrational excitation of N_2 by electron impact, Eq. (2-1). Therefore, the latter process, along with the anharmonic V-V pumping and V-T relaxation, Eqs. (2-5,2-6), remains the dominant mechanism of N_2 vibrational excitation at these conditions. Also, unlike in our previous work in ns pulse discharges [45,46], where N_2 vibrational excitation was insignificant, in the RF discharge the process of Eq. (2-11) is a major channel of $N_2(A^3\Sigma_u^+)$ quenching and also has a significant effect on the rate of vibrational relaxation of nitrogen in the ground electronic state. It reduces the populations on the “plateau” and “tail” of the N_2 vibrational distribution function and increases the rate of heating in the plasma.

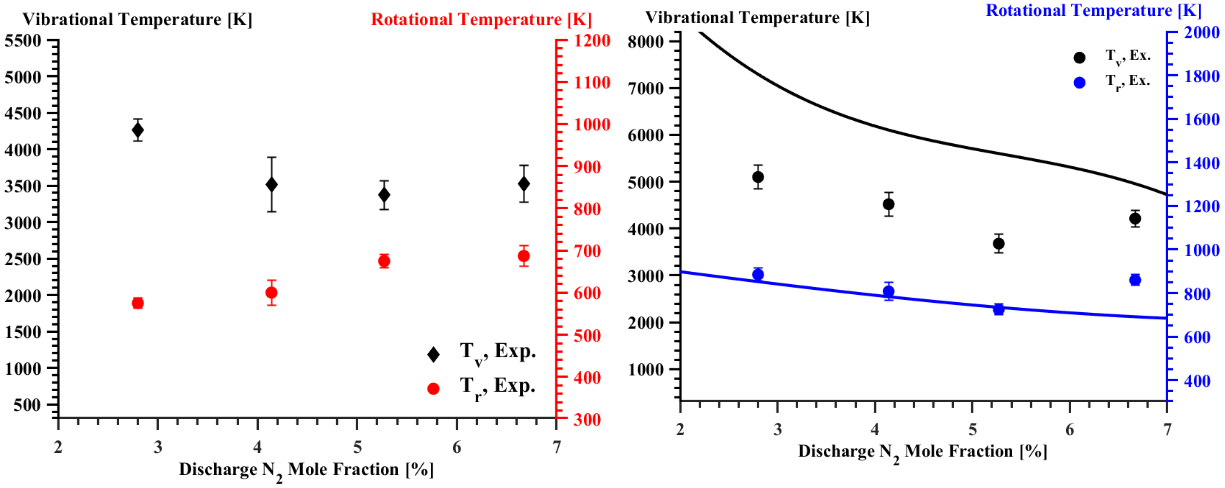

Figure 2 - 14: Variation of N_2 vibrational and translational-rotational temperatures in the RF discharge with N_2 mole fraction in the mixture: (a) N_2 /Ne, (b) N_2/Ar. Symbols, experimental data; lines, modeling predictions.

Figure 2-15 plots the relative vibrational level populations of the ground electronic state nitrogen, f_v, at the end of the RF discharge burst in N_2/Ar mixtures, for several nitrogen fractions in the mixture, 3.0-6.7%. The modeling predictions for 3.0 and 6.7% are compared with the N_2(v=0-6) relative vibrational populations inferred from the CARS spectra (see inset, v=0 populations are extrapolated from those of v=1-6, assuming Boltzmann distribution with the measured vibrational temperature T_v). Again, it can be seen that the model overpredicts the first level vibrational temperature, i.e. the slope of the vibrational distribution function at v=0. The effect of the anharmonic V-V pumping of Eq. (2-5), which produces an extended non-Boltzmann plateau in the vibrational distribution function, is readily apparent. The vibrational excitation is predicted to be most pronounced at the lowest N_2 fraction, 3.0%. Analysis of the modeling predictions indicates that this occurs due to the increase of the electron temperature in the plasma as the nitrogen fraction is reduced, since the electron energy loss to vibrational excitation of N_2 becomes less significant. This increases the rate coefficients of all electron impact processes, due to their strong (near exponential) dependence of the electron temperature. As a result, the specific vibrational energy loading per N_2 molecule in the mixture increases, even though the fraction of the discharge input power going to N_2 vibrational excitation becomes smaller.

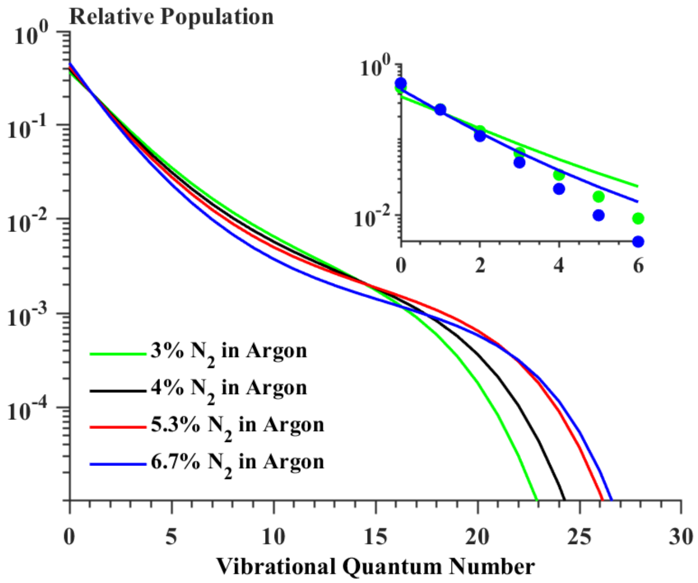

Figure 2 - 15: Quasi-steady-state N_2 vibrational level populations at the end of the RF discharge burst in N_2/Ar mixtures, predicted by the model for different nitrogen fractions in the mixture. Inset compares the modeling prediction with the vibrational populations inferred from the CARS spectra.

At the low N_2 mole fractions, the tail of the predicted vibrational distribution function crashes at lower vibrational levels (see Fig. 2-15). This is caused by more efficient generation of N atoms, both by electron impact of Eq. (2-3) and by the pooling mechanism of Eq. (2-9), at higher electron temperatures. V-T relaxation by N atoms, including multi-quantum jumps (Eq. (2-6)), is the dominant kinetic process reducing the N_2 vibrational populations at high vibrational levels

($v \gtrsim 15$) and increasing the populations at $v \lesssim 15$ (see Fig. 2-15). Compared to this, V-T relaxation by N_2 and Ar is negligibly slow, using the V-T rates predicted in [54] or [56]. The number densities of N atoms and $N_2(A^3\Sigma_u^+)$ molecules predicted by the model are plotted in Fig. 2-16. As discussed above, the N atom number density inversely correlates with the N_2 fraction in the mixture, due to the electron temperature reduction. The predicted N_2(A) number density variation is less pronounced, since it is controlled by the rates of N_2 electronic excitation by electron impact, Eq. (2-2), and the number density of N atoms (the dominant quenching species, Eq. (2-10)), both of which decrease with the electron temperature as the N_2 fraction is increased. Although N atoms and $N_2(A^3\Sigma_u^+)$ molecules are not measured in the present experiments, the modeling predictions using the same kinetic mechanism are in good agreement with time-resolved measurements of these species in a ns pulse discharge in nitrogen [45,46].

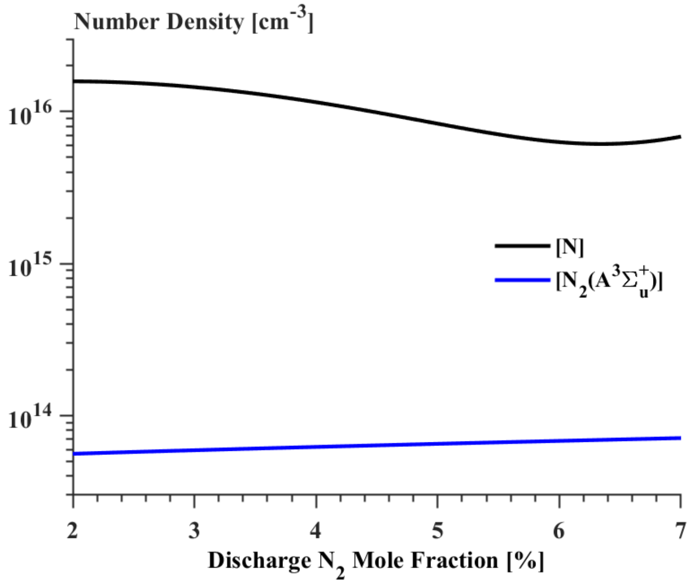

Figure 2 - 16: $N_2(A^3\Sigma_u^+)$ and N atom number densities predicted by the kinetic model at the end of the RF discharge burst in N_2/Ar mixtures, vs. N_2 fraction in the mixture.

Chapter 3: CO_2 Dissociation in Non-Equilibrium Discharges

3.1 Experimental Setup

Nanosecond pulses in N_2/CO_2 mixtures are studied in a discharge cell which is shown schematically in Fig 3-1. The plasma is generated in a rectangular cross section quartz channel (22 mm x 10 mm), with CaF_2 optical access windows at the Brewster's angle at both ends. A 5% CO_2-N_2 mixture flows through the cell at the flow rate of 335 sccm and pressure of 100 Torr. The discharge in the cell is produced between two parallel rectangular plate copper electrodes 60 mm long and 12 mm wide, mounted to the top and bottom outside walls of the cell, as shown in Fig. 3-1. The electrodes are attached to the walls by a silicon rubber adhesive, to prevent corona discharge formation near the electrode surfaces. The discharge is sustained by a positive polarity MegaImpulse NPG-18/100k generator (peak voltage 30 kV, pulse duration 15 ns) operating at a pulse repetition rate of 100 kHz, with burst duration of 250 pulses, and burst repetition rate of 2 Hz. The discharge voltage and current waveforms are measured by the Tektronix P-6015 high voltage probe and Pearson 2877 current monitor. Broadband plasma emission images are taken using a gated PI-MAX 3 ICCD camera with a UV lens.

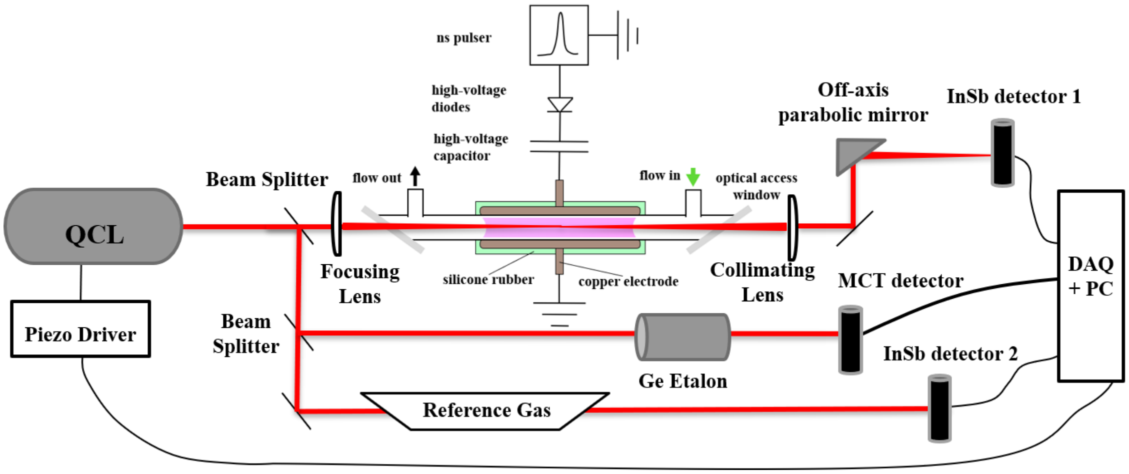

Figure 3 - 1: Schematic of experimental apparatus and QCL absorption spectroscopy diagnostic.

Vibrational level populations of nitrogen molecules in the ground electronic state are measured by broadband N_2 vibrational CARS [37]. Briefly, 80% of the second harmonic output of an externally triggered, injection-seeded, ns Nd:YAG laser (Surelite, SLIII-10) is used to pump a custom-built broadband dye laser to generate the Stokes beam with the FWHM of 7 nm, centered at 605 nm. The rest of the Nd:YAG laser output is used as the CARS pump/probe beam. The pulse energies of the pump/probe and the Stokes beams are 1.5 mJ and 0.25 mJ, respectively. The two beams are combined using a delay line and dichroic mirrors and focused in the test section by a 22 cm focal distance lens, in collinear phase matching geometry. 95% of the CARS signal in the test section is generated over a region 20 mm long, shorter than the length of the electrodes. The CARS signal is separated from the pump and Stokes beams using dichroic mirrors and detected by an Andor 750 spectrometer with Andor EMCCD camera. The resolution of the broadband CARS spectra is dominated by the spectrometer instrument function, approximately 0.4 cm^{-1} FWHM. N_2 vibrational and rotational-translational temperature are inferred from the CARS spectra using a CARSFT program [53], which has been modified to infer these parameters independently. The CARS optical system is shown in Figure 2-2.

The schematic of the QCL absorption spectroscopy diagnostic is shown in Fig. 3-1. A continuous wave Quantum Cascade Laser (Daylight Solutions 41045-MHF, with the CW full tuning range of 2120-2310 cm^{-1}, and mode-hop-free tuning range of 2175-2285 cm^{-1}), controlled by a piezoelectric driver (Thorlabs MDT694B) is used to measure the time-resolved CO_2 and CO vibrational level populations in the plasma. The laser output is split into three beams using CaF_2 beamsplitters, with the first beam passing through a low-pressure reference cell, the second through a germanium etalon (Light Machinery), and the third focused into the discharge cell by a 20 cm focal distance lens, as shown in Fig. 3-1. The reference cell, filled with a mixture of N_2O, ^{12}CO, $^{13}CO_2$, and $^{12}CO_2$, at the total pressure of 5-30 Torr is used for the absolute calibration of the laser output. The etalon with the Free Spectral Range (FSR) of 0.73 GHz is used for the accurate measurement of the laser tuning steps, as discussed below. Focusing the laser beam into the discharge cell prevents its clipping on the walls and greatly reduces the beam steering by the acoustic waves generated by the ns pulsed discharges in the cell. After the beam is recollimated, the signals from all three beams are monitored by InSb IR detectors (Judson J10D-M204-R01M-60) with pre-amplifiers (Judson PA-9-44, bandwidth 1 MHz), for the discharge cell and reference cell beams, while the etalon beam is measured with a HgCdTe IR detector/amplifier assembly (Kolmar KMPV11-1-J1, bandwidth 10 MHz). All signals are acquired and saved by a computer-controlled data acquisition card (National Instruments PCI-DAS4020/12, sampling rate up to 20 MHz, 200 kHz sampling rate used in the present work). To prevent the electromagnetic noise from the pulse generator, the laser and the IR detectors are placed within a grounded Faraday cage enclosure.

During the operation, the three time-resolved absorption signals are acquired during and after each ns pulse discharge burst at a fixed laser output wavelength, without averaging over multiple bursts. After each burst, the piezoelectric controller voltage is stepped in time to increase the laser wavelength by approximately 0.0027 cm^{-1}, as shown schematically in Fig. 3-2(a). Fig. 3-2(b) plots the typical signals measured after the etalon and the reference cell, illustrating the etalon fringe pattern and several $^{13}CO_2$ absorption lines used for the absolute wavelength calibration. The corrected, accurate values of the laser tuning steps are inferred by matching the reference absorption lines to the HITRAN spectra. Specifically, ^{12}CO, N_2O, and $^{13}CO_2$ absorption lines are used for the wavelength calibration at 2120-2220 cm^{-1}, 2160-2260 cm^{-1}, and 2260-2310 cm^{-1}, respectively. Figure 3-3(a) plots the relative tuning characteristic of the laser during the experiment, and Fig. 3-3(b) shows the calibrated spectrum matched to the reference spectrum.

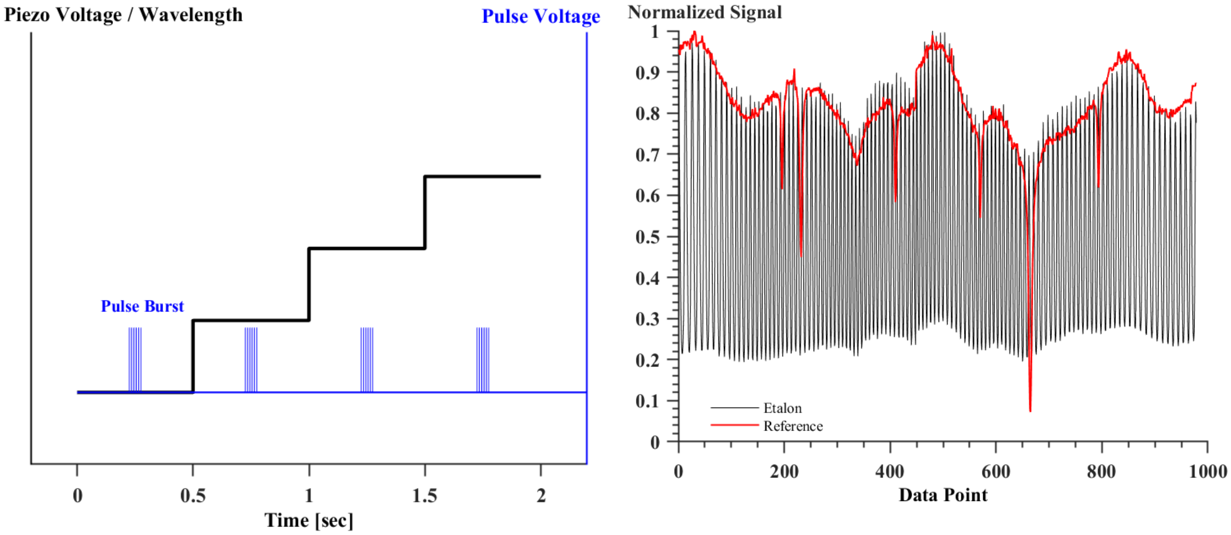

Figure 3 - 2: (a)Experiment chronology illustrating the step-scan approach to data collection with a 2 Hz burst repetition rate, (b) measured signals from reference and etalon signals during the experiment

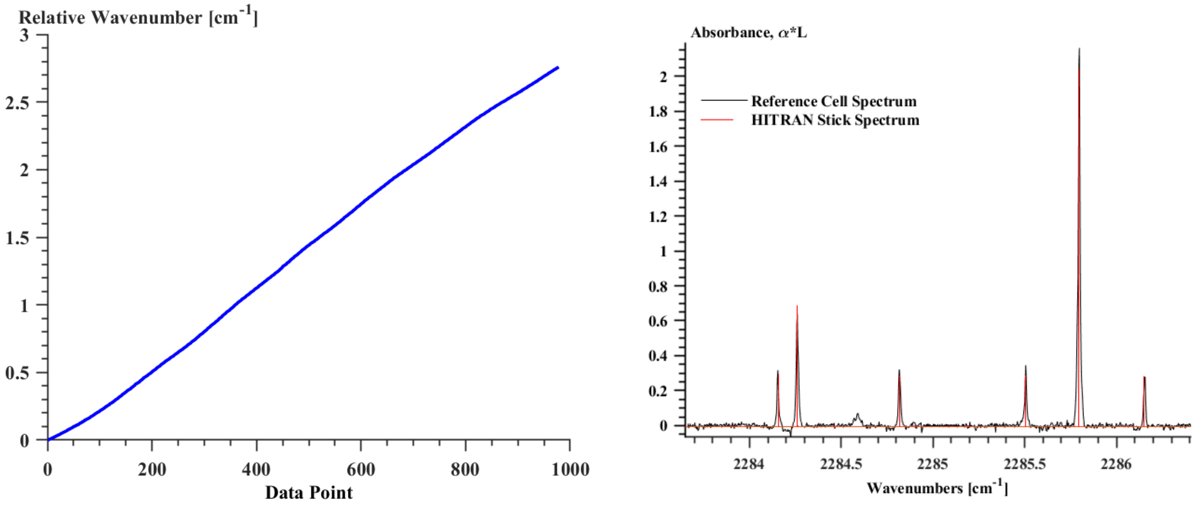

Figure 3 - 3: (a) Wavelength calibration curve, and (b) Comparison of a calibrated reference signal to 'stick' spectrum for $^{13}CO_2$ isotopologue generated from HITRAN database to identify the absolute wavelength

The CO_2 and CO vibrational level populations are inferred from the calibrated QCL absorption spectra measured in the discharge cell following the procedure described in Ref. [29], using the best fit synthetic spectra. The state-specific total energy, Einstein coefficients, and collisional broadening parameters for the Voigt absorption line shapes used by the synthetic spectrum computer code are taken from the HITRAN database. It is assumed that all rotational states in the same vibrational band follow the Boltzmann distribution at the rotational temperature. The vibrational populations are inferred in two steps. First, the translational-rotational temperature is inferred from the intensities of the rotational absorption transitions in the same vibrational band, to calculate the rotational Boltzmann factors and line shapes in the synthetic spectrum code. Second, the program infers the vibrational populations of the lower and upper states for all detected absorption transitions by computing the characteristic absorption cross sections of unique vibrational bands and then finding the linear combination which minimizes the least squares residual relative to the measured spectra. The resulting weighting factors are then precisely the vibrational number densities. This approach allows the inference of the vibrational level populations when the vibrational distribution is non-Boltzmann. To determine the population of the ground vibrational state of $CO_2(00^00)$, the absorption outside of the excited region is subtracted as the baseline. The uncertainty of the inferred vibrational populations is $\frac{n_{v_{max}}^2}{n_{v_{max}-1}}$, where $n_{v_{max}}$ is the population of the highest vibrational level detected in each band. The detailed description of the routine and the program is elaborated on in Appendix A.

3.2 Results and Discussion

Figure 3-4 plots the discharge current, voltage, and coupled energy waveforms, measured in a 5% CO_2 -N_2 mixture at P=100 Torr, at the pulse repetition rate 100 kHz, for pulse #250 in the burst. It can be seen that most of the energy is coupled by the first incident pulse, although multiple pulse reflections result in additional energy coupling. For each pulse number in the burst, the coupled energy variation burst-to-burst did not exceed several percent, as indicated in Fig. 3-5(a). During the first 150 pulses, the pulse energy gradually decreases, most likely due to the temperature rise in the plasma, since the coupled energy is a double dielectric barrier ns pulse discharge scales with the number density [62]. Figure 3-5(b) shows the single-pulse, broadband plasma emission images taken at these conditions. It can be seen that the well-defined discharge filaments begin to form in the plasma after approximately 40 pulses. The most likely reason for this is the electron attachment to CO_2, which reduces the residual electron density needed to generate a uniform plasma during the subsequent pulses. A similar effect, although not as pronounced, has been detected previously in pulse bursts in N_2-O_2 mixtures [63]. In comparison, the plasma generated in non-electronegative mixtures at the same conditions (nitrogen, N_2-H_2, and N_2-CH_4) does not exhibit the filamentation [63,64]. During the second half of the pulse burst, the discharge filaments become more diffuse, which is indicative of the further temperature increase [65]. Finally, the locations of the filaments vary burst-to-burst, such that the image accumulated over the entire burst appears nearly uniform (see Fig. 3-5(b)).

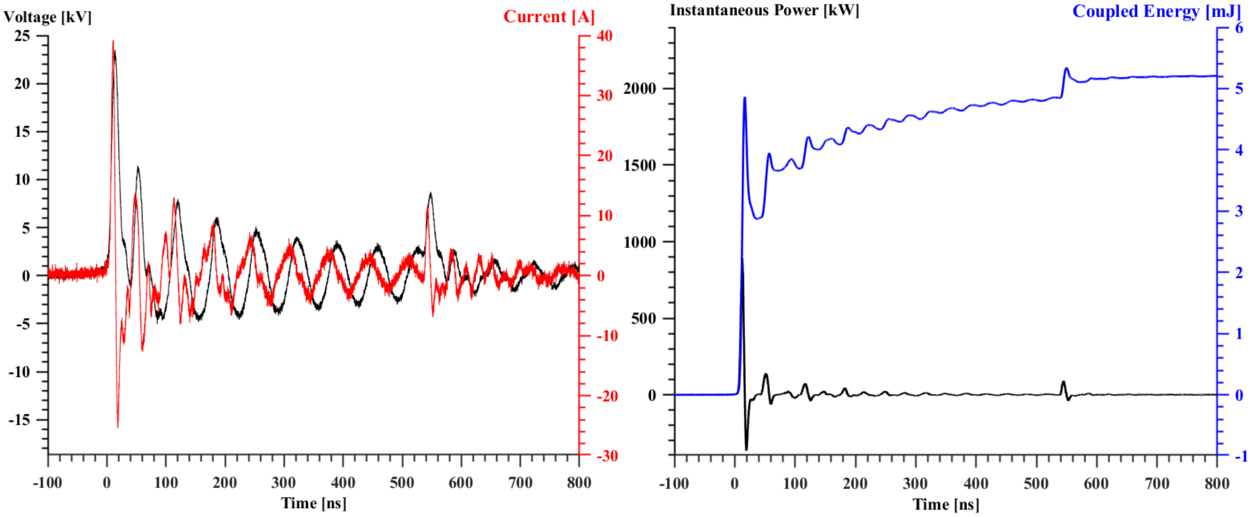

Figure 3 - 4: Typical ns discharge current and voltage waveforms and (b) instantaneous power and coupled energy

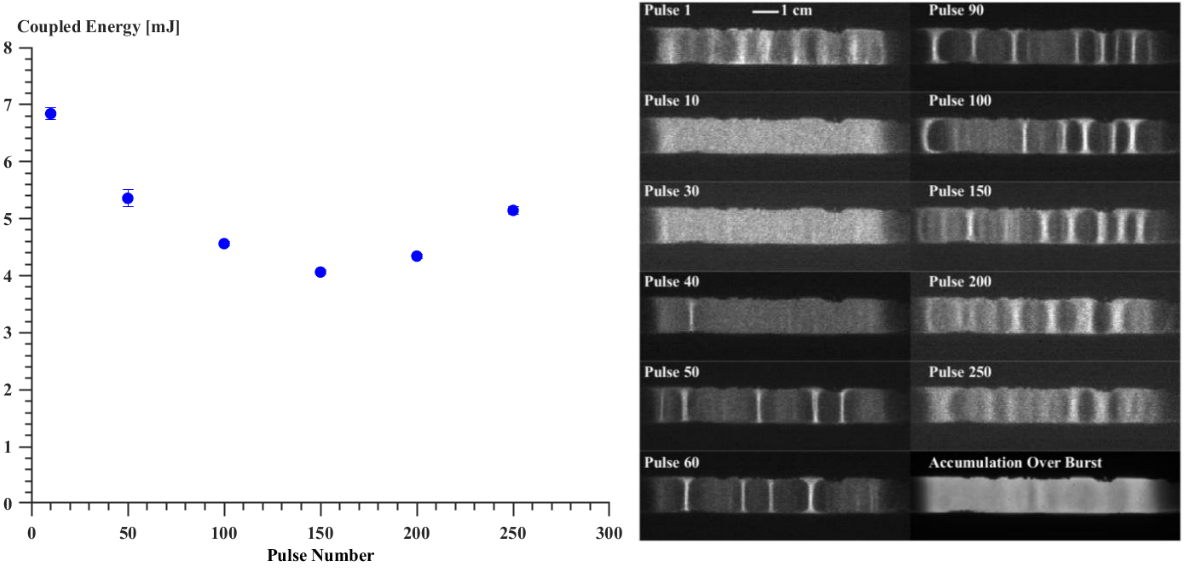

Figure 3 - 5: (a) Coupled pulse Energy as burst progresses, and the discharge characteristics change; error bars indicate the standard deviations of the measurements taken over 50 bursts. (b) Single shot, 4 µs exposure ICCD images of emission generated by individual plasma pulses, and 2.5 ms exposure single-shot emission integrated over entire burst

A part of a typical time-resolved absorption spectrum (1.3 cm^{-1}), measured in a 5% CO_2 - N_2 mixture at P=100 Torr during the discharge pulse burst and afterglow is shown in Fig. 3-6. The discharge is operated at a pulse repetition rate of 100 kHz, with 250 pulses in the burst (burst duration of 2.5 ms). Two of the $^{12}CO_2$ absorption transitions labeled in the spectrum illustrate the typical behavior of the ground vibrational state, v_3=0 (dominated by the plasma heating), and the first excited state, v_3=1 (dominated by the initial vibrational excitation and the subsequent relaxation), in the asymmetric stretch vibrational mode.

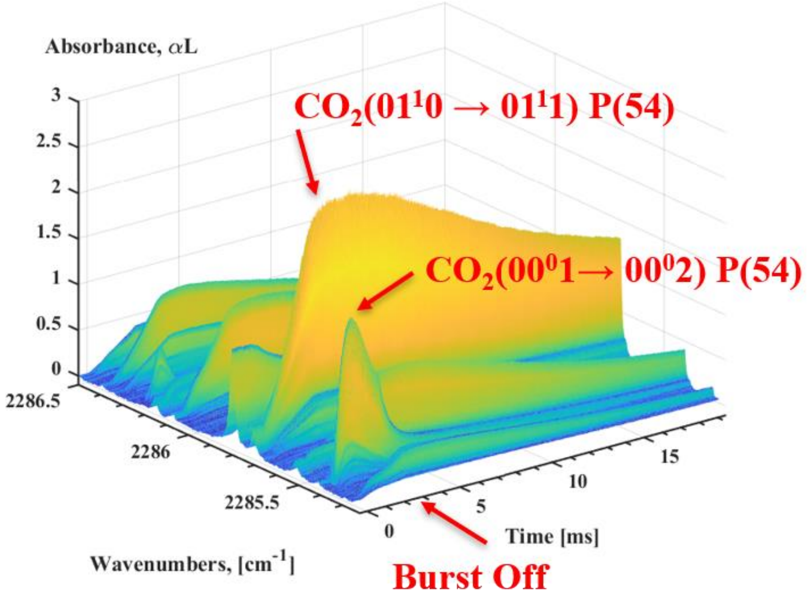

Figure 3 - 6: Typical temporally-resolved non-equilibrium CO_2 mid-infrared spectrum during the pulse burst and afterglow

Figure 3-7 shows two “time slices” of such spectra taken at the same operating conditions, one taken during the discharge burst (at t=0.63 ms) and the other at the end of the burst (at t=2.5 ms), compared with the best fit synthetic spectra. In both cases, the “time slices” are taken 9.8 μs after a discharge pulse. The time-resolved CO_2 vibrational level populations are inferred from the lines with peak absorbance not exceeding $\alpha L \lesssim 2.3$ (path-integrated transmission on the line center $\gtrsim 10\%$). Figure 3-8 also shows two "time slice" spectra with several absorption lines in the R branch of the CO(v=0) band, from CO generated in the plasma during the discharge burst at these conditions (note the breaks in the horizontal axes). One of the CO(v=1) lines was also detected during the measurements, yielding the time-dependent CO vibrational temperature.

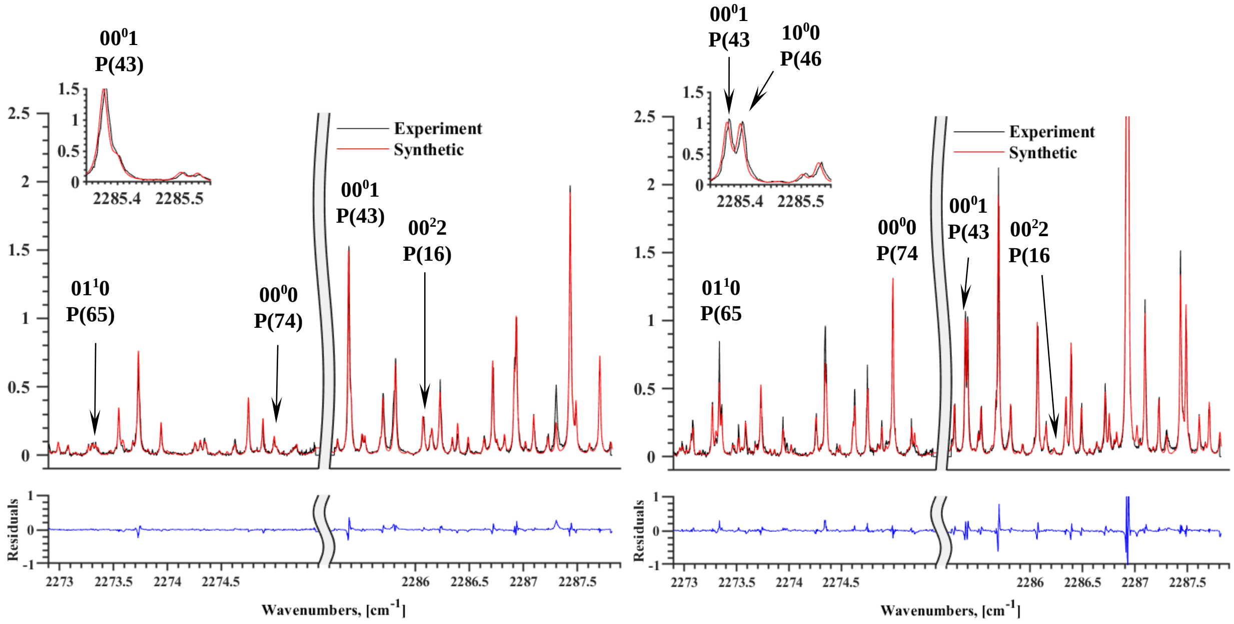

Figure 3 - 7: Comparison of the experimental and synthetic (HITRAN) CO_2 absorption spectra at the conditions of Fig. 5: (a) t = 0.63 ms and (b) t=2.5 ms after the beginning of the burst. Several $^{12}CO_2$ absorption lines are labeled.

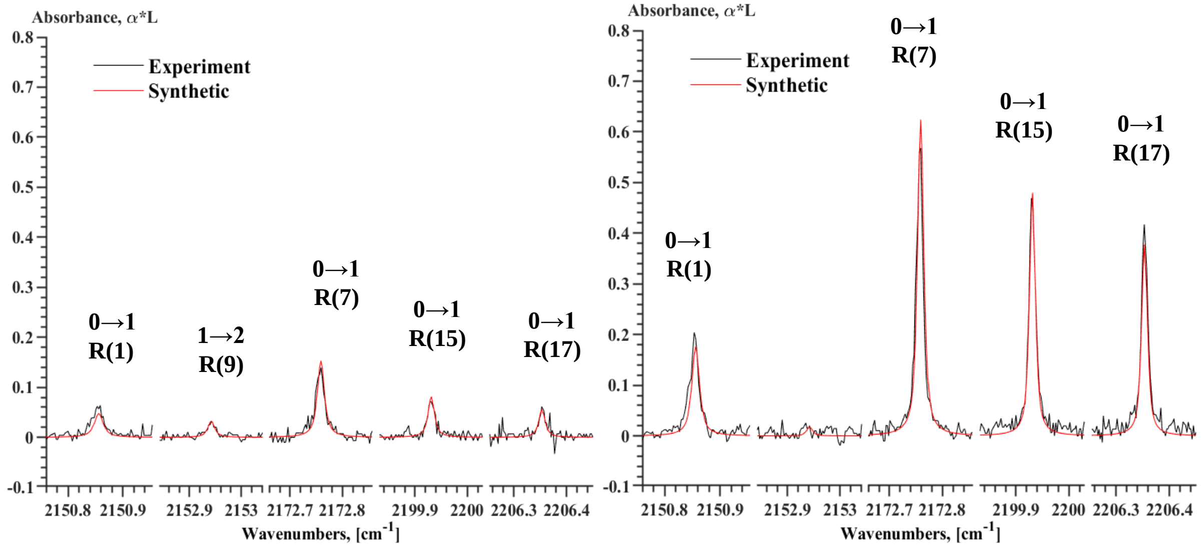

Figure 3 - 8: Comparison of the experimental and synthetic (HITRAN) CO absorption spectra exhibiting the ground and first vibrational levels at the conditions of Fig. 5: (a) t = 0.5 ms and (b) t = 10 ms after the beginning of the burst.

The Boltzmann plots shown in Fig. 3-9 are used for the inference of the time-resolved rotational temperature from the CO_2 and CO spectra such as shown in Figs. 6,7.

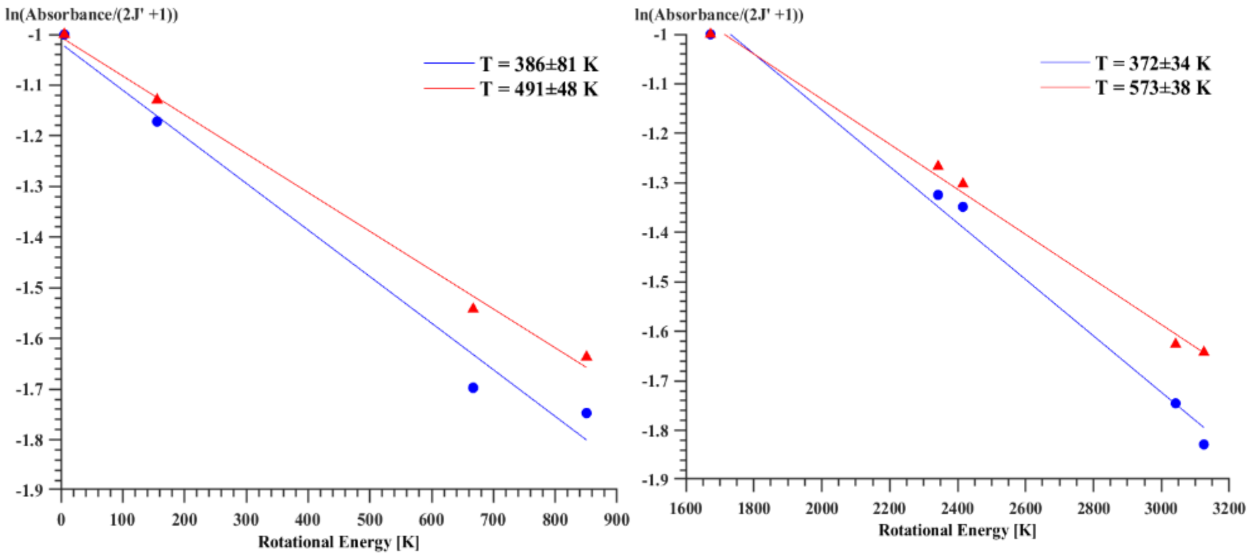

Figure 3 - 9: Boltzmann plots used to infer the rotational temperature from (a) CO(v=0) vibrational band, and (b) CO_2 (01^10) vibrational band, measured 1 ms and 2.5 ms after the beginning of the burst, at the conditions of Fig. 5. The temperature uncertainty is based on the standard deviation of the linear slope.

After the rotational temperature is inferred (i.e. the relative populations of the vibrational-rotational levels in each vibrational band are constrained), the vibrational level populations of two CO_2 isotopologues are inferred from the spectra such as shown in Fig. 6, using the best fit synthetic spectra.

The results for two “time slices”, t = 0.63 ms and t=2.5 ms, are shown in semilog plots in Fig. 3-10. It can be seen that relatively early in the burst, vibrational levels of the asymmetric stretch mode, v_3=0-3, are detected, with their populations strongly non-Boltzmann. The deviation of v_3=2,3 populations from the Boltzmann distribution is well pronounced and exceeds significantly the measurement uncertainty. Although the state-specific kinetic modeling calculations at these conditions are not yet available, we conjecture that this deviation is mostly likely indicative of the residual “nascent” vibrational distribution generated by electron impact during a ns pulse [66], rather than due to the anharmonic V-V pumping. Later during the burst, the asymmetric stretch mode populations decrease considerably and approach a nearly straight line (i.e. a Boltzmann distribution with the vibrational temperature T_3). In contrast, the vibrational populations of the bending mode, v_2=0-4, always follow nearly straight lines, indicating a lower vibrational temperature T_2. These results appear qualitatively similar to the diamond-shapepattern of the steady-state CO_2 vibrational populations measured in a DC glow discharge [47], with $T_3 > T_2$.

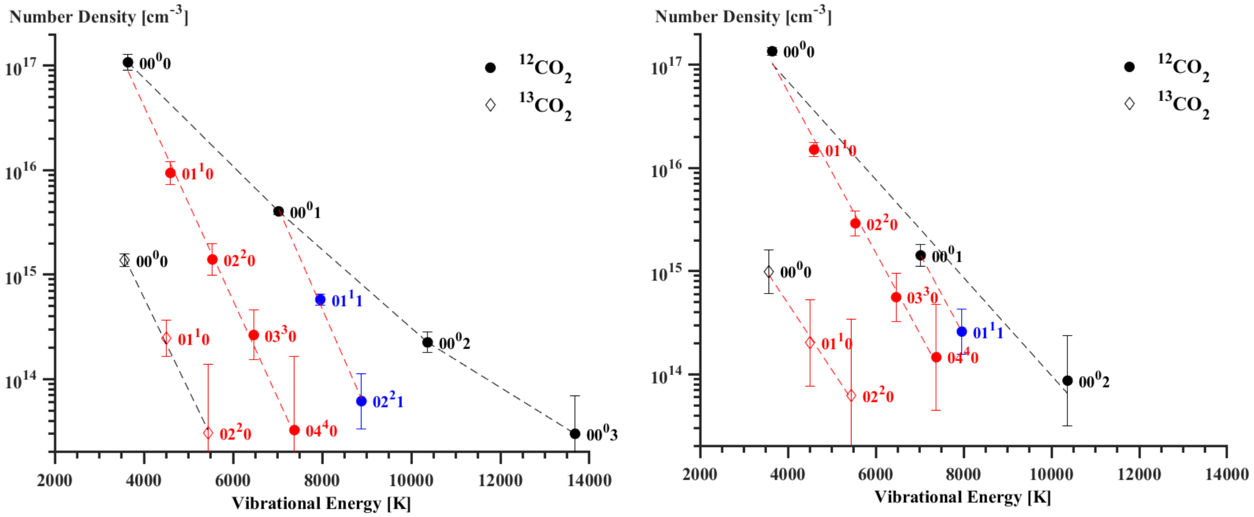

Figure 3 - 7: Absolute populations of $^{12}CO_2$ and $^{13}CO_2$ vibrational levels at the conditions of Fig. 5, inferred from the best fit synthetic spectra such as shown in Fig. 6, (a) t = 0.63 ms and (b) 2.5 ms after the beginning of the discharge burst. The uncertainties are based on the standard deviation of the inferred values.

To complement the measurements of CO_2 and CO vibrational level populations, N_2 rotational and vibrational temperatures during and after the discharge burst are inferred from the CARS spectra, such as shown in Fig. 3-11. At the present conditions, N_2 vibrational excitation remains relatively modest, such the $N_2(v>1)$ vibrational populations could not be inferred from the CARS spectra.

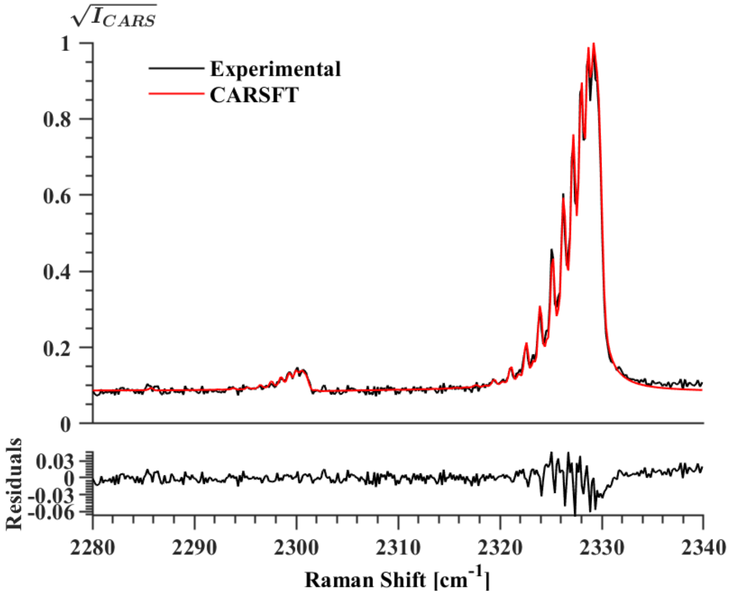

Figure 3 - 8: Comparison of a typical $N_2(v=0,1)$ vibrational CARS spectrum and best fit CARSFT synthetic spectrum in a 5% CO_2/N_2 mixture at the conditions of Fig. 5, at t = 0.75 ms. Inferred N_2 rotational and vibrational temperatures T = 373 ± 12 K and T_v = 1159 ± 80 K.

The results of QCL absorption spectroscopy and CARS measurements are summarized in Fig. 11. To simplify the data comparison, the vibrational nonequilibrium in the CO_2 asymmetric stretch mode is characterized in terms of the “first level” vibrational temperature (i.e. the slope of the vibrational distribution at v_3=0), $T_3 = \frac{\omega_{e3}(1-2x_{e3})}{\ln\left[\frac{f_{v_3=0}}{f_{v_3=1}}\right]}$. It is apparent that the vibrational temperature of nitrogen, the most abundant species in the mixture, initially increases, peaking after ~ 50 pulses, before decreasing again to near detection limit after ~ 200 pulses. Although the input energy fraction going to vibrational excitation by electron impact in a ns pulse discharge burst is relatively low, it is sufficient to produce detectable vibrational nonequilibrium [66]. Reducing the plasma volume would result in a much stronger vibrational excitation, even by a single ns discharge pulse [66,67]. A significant reduction of the N_2 vibrational temperature during the second half of the burst, also detected in a single-pulse ns discharge afterglow in our previous work [68], indicates the rapid vibrational energy transfer to CO_2, with its subsequent V-T relaxation. Both $T_3(CO_2)$ and $T_v(CO)$ follow $T_v(N_2)$ fairly closely (see Fig. 3-12), due to the relatively small difference between N_2, CO, and $CO_2(\nu_3)$ vibrational quanta.

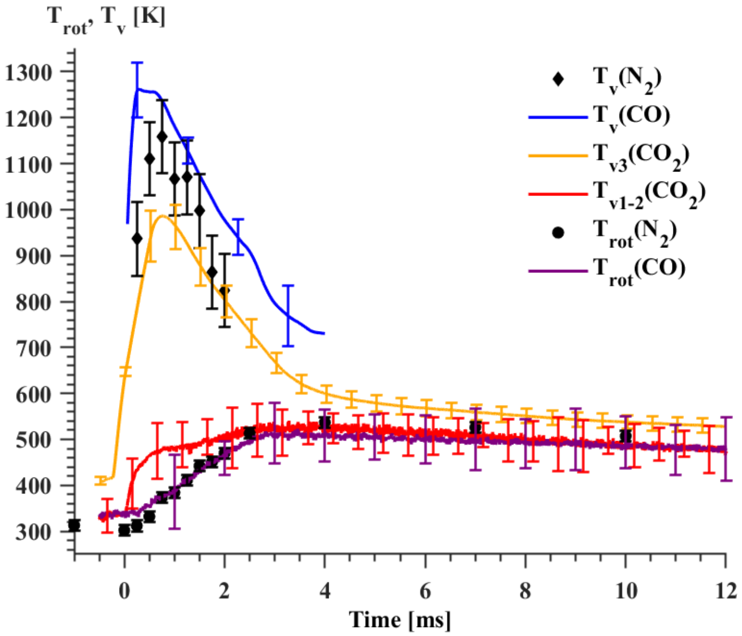

Figure 3 - 9: Vibrational and rotational temperatures of three major molecular species (N_2, CO_2, and CO) during and after the ns pulse discharge burst in a 5% CO_2-N_2 mixture, at the conditions of Fig. 5. The uncertainties in CO_2 and CO vibrational and rotational mode temperatures are based on the standard deviation of the slopes such as shown in Fig. 9. Uncertainties in N_2 vibrational and rotational temperatures are based on the 20% rise of CARSFT least squares residual

At these conditions, the vibrational temperatures of $CO_2(\nu_3)$ and CO are likely controlled by the rapid V-V energy transfer from N_2. On the other hand, the CO_2 bending mode vibrational temperature, T_2, remains low and follows closely the rotational temperatures inferred from the CARS measurements (for N_2) and QCL absorption spectra (for CO). The symmetric stretch mode vibrational temperature, T_1 (not plotted in Fig. 3-12), is very close to T_2, although it is inferred using a smaller number of CO_2 vibrational states. N_2 and CO rotational temperatures are close to each other, as expected, and increase monotonously during the discharge burst. In the afterglow after the burst, the vibrational mode temperatures gradually approach the rotational temperatures, although the CO vibrational temperature still exhibits a slight offset.

Time-resolved CO number density and the CO_2 dissociation rate during and after the burst are plotted in Fig. 3-13. For these measurements, the slowly varying "baseline" CO absorption by the residual CO remaining in the cell from the previous discharge burst generated 500 ms earlier was subtracted from the time-resolved absorption signal. It is readily apparent that most of CO is generated during the discharge burst, such that its number density in the afterglow remains nearly constant on a ms time scale. The CO number density generated by the discharge burst, $n_{CO} = 3.0 \cdot 10^{15}$ cm^{-3}, is significantly lower compared to that of the initial CO_2 number density, $n_{CO_2} = 1.6 \cdot 10^{17}$ cm^{-3}. The rate of CO_2 dissociation is obtained by differentiating the time-resolved CO number density over time, using the Savitzky-Golay filter to reduce the noise in the data. The dissociation rate is normalized by dividing it over the CO_2 mole fraction and the total number density in the cell (the latter obtained from the rotational temperature measurements, see Fig. 3-12). It can be seen that the normalized (i.e. specific) dissociation rate decreases gradually during the discharge burst, by approximately a factor of two, and does not exhibit a correlation with the $CO_2(\nu_3)$ vibrational temperature, which peaks during the burst (see Fig. 3-12). This suggests that at the present conditions, the role of the vibrationally stimulated "ladder climbing" dissociation mechanism is insignificant, such that the CO_2 dissociation via electronic excitation by electron impact may be the dominant channel. The reduction of the specific dissociation rate, at a nearly constant CO_2 mole fraction in the mixture, also suggests that the CO yield by the electron impact dissociation also decreases during the burst.

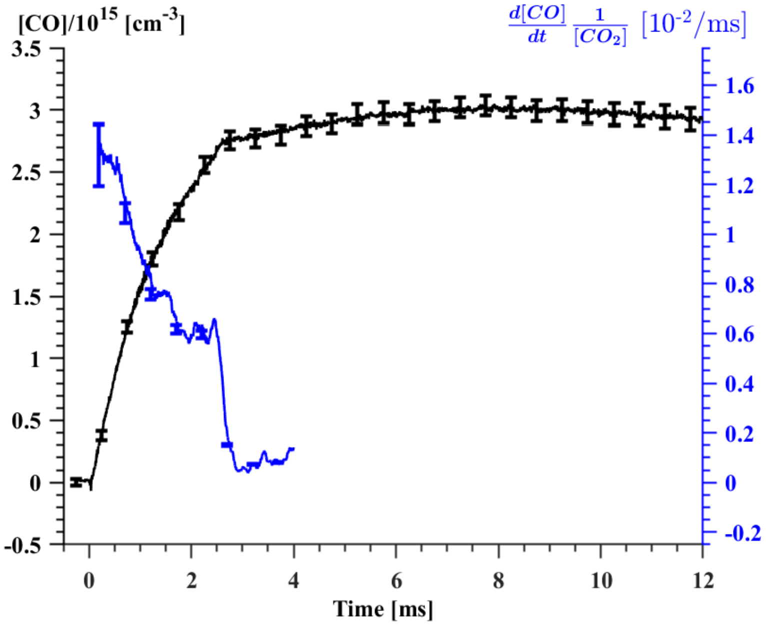

Figure 3 - 10: CO number density and normalized CO_2 dissociation rate during and after the burst, at the conditions of Fig. 11.

Although understanding the kinetic mechanism of CO_2 dissociation at the present conditions requires comparison of the experimental data with the kinetic modeling predictions, an instructive comparison can be made with N_2 dissociation in a plane-to-plane ns pulse discharge at similar experimental conditions [69]. In Ref. [69], the number density of N atoms generated by a 150-pulse burst in 150 Torr of nitrogen is $[N] \approx 4 \cdot 10^{15}$ cm^{-3}, i.e. comparable to the CO number density in the present work. Both the N atom recombination in Ref. [69] and CO recombination with O atoms in the present work are negligible on a ms time scale, such that the number densities measured at the end of the burst are representative of the generation rates. The discharge specific energy loading in the present work, $q \approx 0.061$ J/cm^3 ($\frac{q}{N} \approx 0.12$ eV/molecule, where N is the initial number density), is comparable to that in Ref. [69], $q \approx 0.085$ J/cm^3 ($\frac{q}{N} \approx 0.11$ eV/molecule). The energy cost per CO molecule, $\frac{q}{n_{CO}} \approx 130$ eV, is close to the energy cost per N atom in Ref. [69], $\frac{q}{n_N} \approx 130$ eV. However, the effective energy cost, based on the input energy fraction going to CO_2, $\frac{q}{n_{CO}}\frac{n_{CO_2}}{N} \approx 6.5$ eV. This is close to the threshold of CO_2 electron impact dissociation cross sections, 7 eV and 10.5 eV [69], which yield good agreement with the experimental data on CO_2 dissociation in dielectric barrier discharges [71]. This suggests that CO_2 dissociation by electron impact may be the dominant channel of CO generation at the present conditions, although dissociative quenching of the excited electronic states of N_2, such as $C^3\Pi_u$, $B^3\Pi_g$, and $a'^1\Sigma_u^-$, by CO_2 may also contribute. The effect of $N_2(A^3\Sigma_u^+)$ on CO_2 dissociation is likely to be negligible, due to its slow quenching by CO_2, $k_{CO2} = 2\cdot10^{-14}$ cm^3/s [72]. Further kinetic modeling analysis is expected to provide additional insight into the kinetics of CO_2 dissociation in a ns pulse discharge.

3.3 Ns Pulse – RF Hybrid Plasma

To heat the electrons generated by the ns discharge pulses and generate additional vibrational excitation of N_2 and CO_2 molecules by a sub-breakdown RF waveform applied between the pulses, the electrodes are powered both by the ns pulse generator and a Dressler Cesar 5 kW, 13.56 MHz RF generator, using a circuit shown in Fig. 3-14. The peak RF voltage is too low to produce breakdown in the discharge gap or sustain the plasma without the ns pulses. Therefore, the purpose of applying the RF waveform on top of the ns pulse train is to heat up the electrons already present in the plasma, rather than to generate additional ionization. The circuit is designed to isolate the plasma generators from each other, using the high-voltage diodes to block the current produced by each waveform to the opposing power supply. To enable the circuit operation, a DC bias is added to the RF waveform using a 1:1 transformer, to maintain the positive polarity of the waveform. The DC bias is removed using an RC filter before the high-voltage electrode (see Fig. 3-14). To reduce the Joule heat dissipation on the resistor connected parallel to the load (discharge electrodes), the filter is engaged only during the ns pulse / RF burst, using a MOSFET trigger switch.

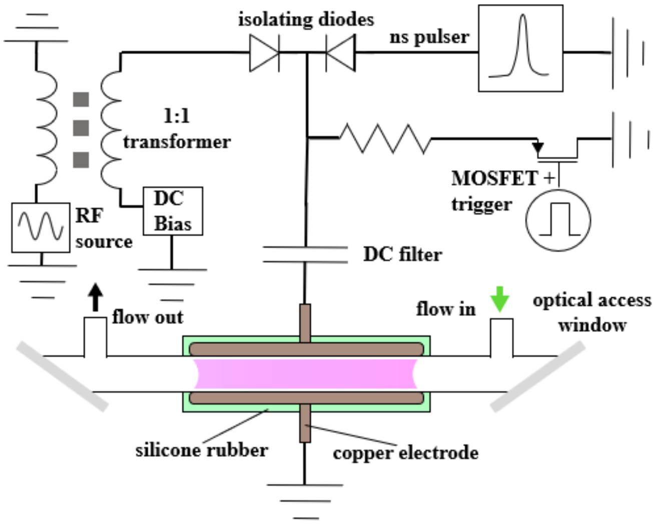

Figure 3 - 11: Schematic of the discharge cell and the external circuit used to generate a ns pulse train overlapped with the sub-breakdown RF waveform.

As discussed in Section I, a ns pulse train combined with the RF voltage to enhance vibrational excitation in the plasma [37]. Each ns discharge pulse, producing the high peak reduced electric field (E/N), generates ionization for the non-self-sustained RF discharge. Since the RF voltage is operated at much lower E/N, significantly below breakdown, it generates efficient vibrational excitation of N_2 molecules in the ground electronic state, without producing additional electronically excited molecules and atoms. By varying the RF voltage amplitude, vibrational excitation in the plasma can be controlled independently, to isolate the reaction pathways of vibrationally excited molecules. In the present study, this approach is extended to significantly higher peak voltage ns pulses compared to [37], by isolating the ns pulse generator and the RF generator from each other (see Fig. 3-14). Figure 3-15 shows the combined ns pulse / RF voltage waveform used to generate the nitrogen plasma at P = 100 Torr, measured on the high-voltage electrode. In Fig. 3-15, the pulse repetition rate is 10 kHz, burst duration is 100 pulses (10 ms long), and the burst repetition rate is 10 Hz, to match the pulse repetition rate of the CARS laser system. The insets show the ns pulse voltage and the RF waveform separately.

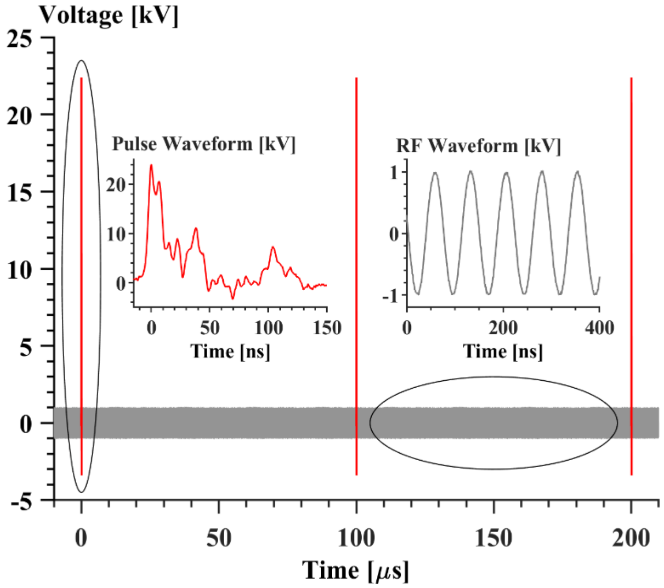

Figure 3 - 12: The combined ns pulse / RF voltage waveform, with the insets showing the ns pulse voltage and the RF waveform separately, on the shorter time scale. Nitrogen, P = 100 Torr, pulse repetition rate 10 kHz, burst duration 100 pulses, burst repetition rate 10 Hz.

Figure 3-16 plots typical broadband N_2 CARS spectra measured at the end of a 100-pulse ns discharge burst, with and without the RF voltage applied between the pulses, compared to the

CARSFT synthetic spectra. Clearly, adding the RF waveform results in an additional vibrational excitation of N_2. In the baseline ns pulse discharge, the N_2(v=1) vibrational band intensity is significantly lower, while in the ns pulse / RF discharge, N_2(v=0-5) vibrational bands are detected. The N_2 vibrational temperature is $T_v(N_2) = 1650$ K in the baseline ns pulse discharge, and $T_v(N_2) = 2760$ K in the ns pulse / RF discharge. This is significantly higher compared to the results of our previous work [37], obtained using a lower pulse peak voltage. The translational-rotational temperature in the plasma is inferred from the rotational structure of the N_2(v=0) vibrational band, using the best fit CARSFT spectra, as shown in Fig. 3-17. The accuracy of the temperature inference is determined by processing 20 room temperature CARS spectra, taken in a 100 Torr nitrogen without the plasma, yielding the mean temperature of T=292 K and the standard deviation of ± 8 K. The rotational temperatures at the end of the ns pulse and ns pulse / RF bursts, both 10 ms long, inferred from the spectra in Fig. 3-17, are T = 307 K and T = 414 K, respectively. The continuation of this work will focus on applying this technique to CO_2/N_2 mixtures and using the QCLAS diagnostic as discussed above to understand the effect of vibrational excitation on CO_2 dissociation.

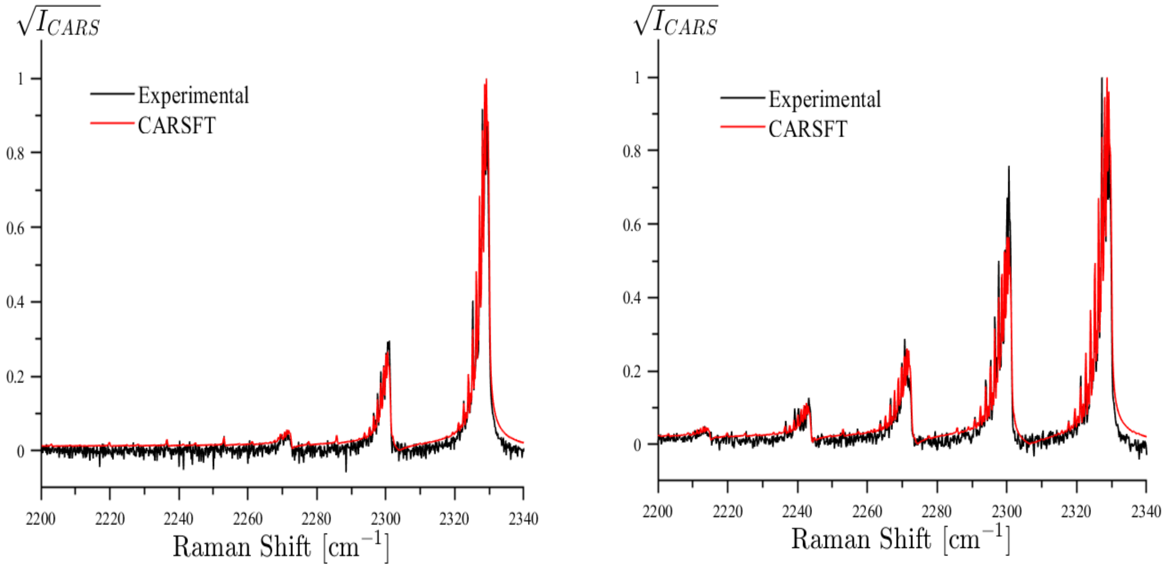

Figure 3 - 13: Broadband N$_2$ CARS spectra measured at the end of a 100-pulse ns discharge burst, without (a) and with (b) RF voltage applied between the pulses, compared to the best fit CARSFT spectra. Nitrogen, P = 100 torr, flow rate 0.1 SLM. Inferred N$_2$ vibrational temperatures are $T_v(N_2) = 1650$ K and $T_v(N_2) = 2760$ K, respectively.

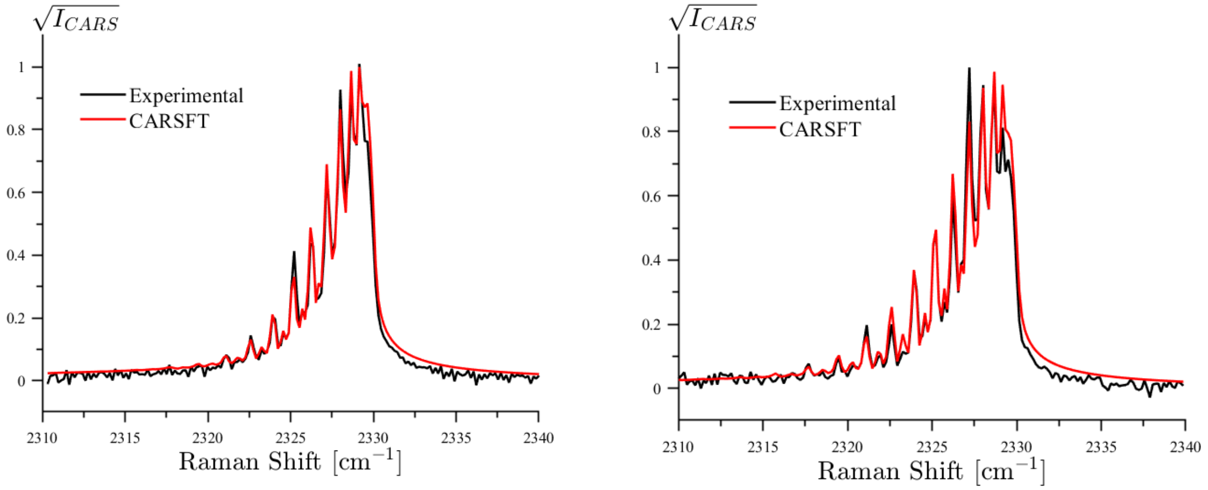

Figure 3 - 14: Figure X4. N$_2$(v=0) CARS spectra measured at the end of a 100-pulse ns discharge burst, without (*a*) and with (*b*) RF voltage applied between the pulses, compared to the best fit CARSFT spectra. Nitrogen, P = 100 torr, flow rate 0.1 SLM. Inferred translational-rotational temperatures are T = 307 K and T = 414 K, respectively.

Chapter 4: Summary and Future Work

In the first chapter, time-resolved N_2 vibrational temperature and translational-rotational temperature in atmospheric pressure plasma jets excited by ns pulse and RF discharges are measured by broadband vibrational CARS. As expected, the results indicate much stronger vibrational excitation in the RF plasma jet, due to the lower reduced electric field and higher time-averaged discharge power. In a ns pulse discharge in N_2/He, N_2 vibrational temperature is significantly lower compared to that in N_2/Ar, due to the more rapid V-T relaxation of nitrogen by helium atoms. Both in N_2/He and N_2/Ar mixtures excited by the ns pulse discharge, N_2 vibrational excitation remains relatively modest. In the RF plasma jets generated in N_2/Ne and N_2/Ar mixtures, the vibrational excitation is much stronger, and increases considerably as the nitrogen fraction in the mixture is reduced. Comparison of the kinetic modeling predictions with the experimental data shows that nitrogen vibrational excitation in N_2/Ar plasma jets with a small N_2 fraction in the mixture (several percent) is controlled primarily by electron impact, anharmonic V-V pumping, and V-T relaxation by N atoms (V-T relaxation by N_2 and Ar remains negligible). In comparison, V-V energy transfer from the vibrationally excited molecules in the lowest excited electronic state, $N_2(A^3\Sigma_u^+,v)$, which are generated mainly by energy transfer from the metastable Ar atoms, has a minor effect on the vibrational populations of the ground electronic state, $N_2(X^1\Sigma_g^+,v)$. Although the discharge input energy fraction going to the electron impact excitation of N_2 electronic states is significant, the quasi-steady-state $N_2(A^3\Sigma_u^+)$ number density, controlled by the energy pooling and quenching by N atoms, remains relatively low, below 10^{14} cm^{-3}. Because of this, the net rate of $N_2(X^1\Sigma_g^+)$ vibrational excitation by the V-V energy transfer from $N_2(A^3\Sigma_u^+)$ is much lower compared to that by the direct electron impact.

These results show that noble gas based, atmospheric pressure RF plasma jets can be used as continuous sources of highly vibrationally excited N_2 molecules and N atoms, with potential applications for plasma-assisted catalysis and plasma surface processing.

In the second chapter, time-resolved CO_2, N_2, vibrational populations and translational-rotational temperature measurements are made in a CO_2-N_2 plasma sustained by a ns pulse discharge burst in plane-to-plane geometry. Time-resolved, absolute number density of CO, a major product of CO_2 dissociation, is also inferred from the experimental data. These measurements are used to elucidate CO_2 dissociation kinetics. The discharge is sustained in a CO_2-N_2 mixture slowly flowing through a rectangular cross section quartz channel, with two parallel plate electrodes external to the channel. The results indicate that energy coupling to the plasma in a ns pulse discharge operated at a high pulse repetition rate results in vibrational excitation of both N_2 and CO_2 asymmetric stretch mode. However, the time-resolved rate of CO generation does not exhibit a correlation with N_2 or $CO_2(\nu_3)$ vibrational temperatures, suggesting that CO_2 dissociation via the vibrational excitation is a minor channel at the present conditions. The rate of CO generation, likely via the CO_2 electronic excitation by electron impact, decreases during the discharge burst. Kinetic modeling analysis is needed to provide insight into the kinetics of CO_2 dissociation in a ns pulse discharge. The main focus of the future work will be on the measurements of CO_2 vibrational nonequilibrium, CO number density, and the rate of CO generation in a hybrid ns pulse / RF discharge plasma, to isolate and quantify the major mechanisms of CO_2 dissociation, (i) via excited electronic states populated by electron impact, and (ii) stepwise vibration-vibration pumping of the asymmetric stretch vibrational mode, sustained by the strong vibrational excitation of N_2 and rapid V-V energy transfer to CO_2

Bibliography

1. C.E. Treanor, J.W. Rich, and R.G. Rehm, "Vibrational Relaxation of Anharmonic Oscillators with Exchange-Dominated Collisions", *Journal of Chemical Physics* 48 (1968) 1798
2. C. Dang, J. Reid, and B. K. Garside, "Detailed Vibrational Population Distributions in a CO_2 Laser Discharge as Measured with a Tunable Diode Laser", *Applied Physics* B 27 (1982) 145
3. P. Capezzuto, F. Cramarossa, R. D'Agostino, and E. Molinari, *Journal of Physical Chemistry* 80 (1976) 882
4. A. Fridman, "Plasma Chemistry", Cambridge University Press, 2008
5. I. Adamovich, S. Saupe, M.J. Grassi, O. Shulz, S. Macheret and J.W. Rich, "Vibrationally Stimulated Ionization of Carbon Monoxide in Optical Pumping Experiments", *Chemical Physics* 173 (1993) 491
6. K.A. Essenhigh, Y.G. Utkin, C. Bernard, I.V. Adamovich, and J.W. Rich, "Gas Phase Boudouard Disproportionation Reaction between Highly Vibrationally Excited CO Molecules", *Chemical Physics* 330 (2006) 506
7. C.D. Pintassilgo and V. Guerra, "Kinetic mechanisms in air plasmas", *Plasma Physics and Controlled Fusion* 61 (2019) 014026
8. P. Mehta, P. Barboun, F.A. Herrera, J. Kim, P. Rumbach, D.B. Go, J.C. Hicks and W.F. Schneider, "Overcoming ammonia synthesis scaling relations with plasma-enabled catalysis", *Nature Catalysis* 1 (2018) 269
9. K.A. Essenhigh, "Energy transfer and chemistry of carbon monoxide in vibrational mode non-equilibrium", Ph.D. dissertation, The Ohio State University, 2005
10. Yu.S. Akishev, A.V. Demyanov, I.V. Kochetov, A.P. Napartovich, S.V. Pashkin, V. Ponomarenko, V.G. Pevgov, and V.B. Podobedov, "Determination of Vibrational Exchange Constants in N_2 from Heating of Gas", *High Temperature 20* (1982) 658
11. R. Farrenq, C.Rossetti, G.Guelachvili, W.Urban, "Experimental rovibrational populations of CO up to $v = 40$ from doppler-limited fourier spectra of the sequences $\Delta v = 1$, 2 and 3 emitted by a laser type source", *Chemical Physics* 92 (1985) 389
12. B. Massabieaux, G. Gousset, M. Lefebvre, and M. Pealat, "Determination of $N_2(X)$ vibrational level populations and rotational temperatures using CARS in a D.C. low pressure discharge", *Journal de Physique* 48 (1987) 1939
13. A.V. Dem'yanenko, I.I. Zasavitskii, V.N. Ochkin, S.Yu. Savinov, N.N. Sobolev, M.V. Spiridonov, and A.P. Shotov, *Soviet Journal of Quantum Electronics* 17 (1987) 536
14. P. Supiot, D. Blois, S. De Benedictis, G. Dilecce, M. Barj, A. Chapput, O. Dessaux, and P. Goudmand, "Excitation of $N_2(B^3\Pi_g)$ in the nitrogen short-lived afterglow", *Journal of Physics D: Applied Physics* 32 (1999) 1887
15. V.A. Shakhatov, O. De Pascale, M. Capitelli, K. Hassouni, G. Lombardi, and A. Gicquel, "Measurement of vibrational, gas, and rotational temperatures of $H_2(X^1\Sigma_g^+)$ in radio frequency inductive discharge plasma by multiplex coherent anti-Stokes Raman scattering spectroscopy technique", *Physics of Plasmas* 12 (2005) 023504

16. M.A. Damen, L.M. Martini and R. Engeln, “Temperature evolution in a pulsed CO_2-N_2 glow discharge measured using quantum cascade laser absorption spectroscopy”, *Plasma Sources Science and Technology* 29 (2020) 065016
17. K. A. Vereshchagin, V. V. Smirnov, and V. A. Shakhatov, “CARS study of the vibrational kinetics of nitrogen molecules in the burning and afterglow stages of a pulsed discharge”, *Technical Physics* 42 (1997) 487
18. D. Messina, B. Attal-Tretout, and F. Grisch, “Study of a Non-equilibrium Pulsed Nanosecond Discharge at Atmospheric Pressure Using Coherent Anti-Stokes Raman Scattering”, *Proceedings of the Combustion Institute* 31 (2007) 825
19. A. Montello, Z. Yin, D. Burnette, I.V. Adamovich, and W.R Lempert, “Picosecond CARS measurements of nitrogen vibrational loading and rotational/translational temperature in nonequilibrium discharges”, *Journal of Physics D: Applied Physics* 46 (2013) 464002
20. A. Lo, A. Cessou, P. Boubert and P. Vervisch, “Space and time analysis of the nanosecond scale discharges in atmospheric pressure air: I. Gas temperature and vibrational distribution function of N_2 and O_2”, *Journal of Physics D: Applied Physics* 47 (2014) 115201
21. A. Brisset, F. Guichard, A. Cessou, and P. Tardiveau, “Energy relaxation and heating in the afterglow of high electric field ns-discharges in ambient air using spontaneous Raman scattering”, *Plasma Sources Science and Technology* 30 (2021) 035013
22. J. Kuhfeld, N. Lepikhin, D. Luggenholscher, and U. Czarnetzki, “Vibrational CARS measurements in a near-atmospheric pressure plasma jet in nitrogen: I. Measurement procedure and results”, *Journal of Physics D: Applied Physics* 54 (2021) 305204
23. C.E. Dedic, T.R. Meyer, and J.B. Michael, “Single-shot ultrafast coherent anti-Stokes Raman scattering of vibrational/rotational nonequilibrium”, *Optica* 4 (2017) 563
24. J. Jiang and P. Bruggeman, Private communication 2021
25. W. Van Gaens and A. Bogaerts, “Kinetic modelling for an atmospheric pressure argon plasma jet in humid air”, *Journal of Physics D: Applied Physics* 46 (2013) 275201
26. N.A. Popov, “Vibrational kinetics of electronically-excited $N_2(A^3\Sigma,v)$ molecules in nitrogen discharge plasma”, *Journal of Physics D: Applied Physics* 46 (2013) 355204
27. P. Capezzuto, F. Cramarossa, R. D’Agostino, and E. Molinari, *Journal of Physical Chemistry* 80 (1976) 882
28. C. Dang, J. Reid, and B. K. Garside, “Detailed Vibrational Population Distributions in a CO_2 Laser Discharge as Measured with a Tunable Diode Laser”, *Applied Physics* B 27 (1982) 145
29. A.V. Dem'yanenko, I.I. Zasavitskii, V.N. Ochkin, S.Yu. Savinov, N.N. Sobolev, M.V. Spiridonov, and A.P. Shotov, *Soviet Journal of Quantum Electronics* 17 (1987) 536
30. A. Fridman, “Plasma Chemistry”, Cambridge University Press, 2008, Chapter 5
31. V. D. Rusanov, A. A. Fridman, and G. V. Sholin, “The physics of a chemically active plasma with nonequilibrium vibrational excitation of molecules”, *Soviet Physics Uspekhi* 24 (1981) 447
32. R. I. Azizov, A. K. Vakar, V. K. Zhivotov, M. F. Krotov, O. A. Zinov’ev, B. V. Potapkin, A. A. Rusanov, V. D. Rusanov, A. A. Fridman, “Nonequilibrium plasmochemical process of the CO_2 decomposition in supersonic UHF discharge”, *Doklady Akademii Nauk SSSR* 271 (1983) 94 (in Russian)

33. L.D. Pietanza, O. Guaitella, V. Aquilanti, I. Armenise, A. Bogaerts, M. Capitelli, G. Colonna, V. Guerra, R. Engeln, E. Kustova, A. Lombardi, F. Palazzetti, and T. Silva, "Advances in non-equilibrium CO_2 plasma kinetics: a theoretical and experimental review", *European Physical Journal D* 75 (2021) 237
34. T. Kozak and A. Bogaerts, "Splitting of CO_2 by vibrational excitation in non-equilibrium plasmas: a reaction kinetics model", *Plasma Sources Science and Technology* 23 (2014) 045004
35. T. Kozak and A. Bogaerts, "Evaluation of the energy efficiency of CO_2 conversion in microwave discharges using a reaction kinetics model", *Plasma Sources Science and Technology* 24 (2015) 015024
36. S. Heijkers, R. Snoeckx, T. Kozák, T. Silva, T. Godfroid, N. Britun, R. Snyders, and A. Bogaerts, "CO_2 Conversion in a Microwave Plasma Reactor in the Presence of N_2: Elucidating the Role of Vibrational Levels", *Journal of Physical Chemistry C* 122 (2018) 8704
37. I. Gulko, E.R. Jans, C. Richards, S. Raskar, X. Yang, D. Van Bekerom, and I.V. Adamovich, "Selective Generation of Excited Species in Ns Pulse / RF Hybrid Plasmas for Plasma Chemistry Applications", *Plasma Sources Science and Technology* 29 (2020) 104002
38. Y. Du, T.V. Tsankov, D. Luggenhölscher, and U. Czarnetzki, "Time evolution of CO_2 ro-vibrational excitation in a nanosecond discharge measured with laser absorption spectroscopy", *Journal of Physics D: Applied Physics* 54 (2021) 365201
39. I. Shkurenkov and I.V. Adamovich, "Energy Balance in Nanosecond Pulse Discharges in Nitrogen and Air", *Plasma Sources Science and Technology* 25 (2016) 015021
40. M.A. Damen, L.M. Martini and R. Engeln, "Temperature evolution in a pulsed CO_2-N_2 glow discharge measured using quantum cascade laser absorption spectroscopy", *Plasma Sources Science and Technology* 29 (2020) 065016
41. B.L.M. Klarenaar, R. Engeln, D.C.M. van den Bekerom, M.C.M. van de Sanden, A.S. Morillo-Candas, and O. Guaitella, "Time evolution of vibrational temperatures in a CO_2 glow discharge measured with infrared absorption spectroscopy", *Plasma Sources Science and Technology* 26 (2017) 115008
42. E. Ploenjes, P. Palm, A.P. Chernukho, I.V. Adamovich, and J.W. Rich, "Time-Resolved Fourier Transform Infrared Spectroscopy of Optically Pumped Carbon Monoxide", *Chemical Physics* 256 (2000) 315
43. I. Gulko, E.R. Jans, C. Richards, S. Raskar, X. Yang, D. Van Bekerom, and I.V. Adamovich, "Selective Generation of Excited Species in Ns Pulse / RF Hybrid Plasmas for Plasma Chemistry Applications", *Plasma Sources Science and Technology* 29 (2020) 104002
44. R.E. Palmer, "The CARSFT Computer Code for Calculating Coherent Anti-Stokes Raman Spectra: User and Programmer Information SAND89-8206", Sandia National Labs, Livermore, CA, 1989
45. E.R. Jans, S. Raskar, X. Yang, and I.V. Adamovich, "Kinetics of Metastable $N_2(A^3\Sigma_u^+,v)$ Molecules in High-Pressure Nonequilibrium Plasmas", *Plasma Sources Science and Technology* 30 (2021) 025003
46. X. Yang, E. Jans, C. Richards, S. Raskar, D. van den Bekerom, and Igor V. Adamovich, "Measurements of Atoms and Metastable Species in N_2 and H_2-N_2 Ns Pulse Plasmas",

accepted for publication in *Plasma Sources Science and Technology*, doi.org/10.1088/1361-6595/ac3053

47. G.J.M. Hagelaar and L.C. Pitchford, “Solving the Boltzmann Equation to Obtain Electron Transport Coefficients and Rate Coefficients for Fluid Models”, *Plasma Sources Science and Technology* 14 (2005) 722-733
48. Morgan database, www.lxcat.net, 2016
49. C. Foissac, J. Kristof, A. Annusova, P. Veis, and P. Supiot, “Spectroscopic diagnostics and modelling of a N_2-Ar mixture discharge created by an RF helical coupling device: I. Kinetics of N_2 $(B^3\Pi_g)$ and $N_2(C^3\Pi_u)$ states, *Plasma Sources Science and Technology* 21 (2012) 055021
50. I.A. Kossyi, A.Yu. Kostinsky, A.A. Matveyev, V.P. Silakov, “Kinetic Scheme of the Non-equilibrium Discharge in Nitrogen-Oxygen Mixtures”, *Plasma Sources Science and Technology* 1 (1992) 207
51. J.T. Herron, “Evaluated Chemical Kinetics Data for Reactions of $N(^2D)$, $N(^2P)$, and $N_2(A^3\Sigma_u^+)$ in the Gas Phase”, *Journal of Physical and Chemical Reference. Data* 28 (1999) 1453
52. B. Gordiets, C.M. Ferreira, M.J. Pinheiro, and A. Ricard, “Self-consistent kinetic model of low-pressure flowing discharges: I. Volume processes”, *Plasma Sources Science and Technology* 7 (1998) 363
53. T. Ahn, I.V. Adamovich, and W.R. Lempert, “Determination of Nitrogen V-V Transfer Rates by Stimulated Raman Pumping”, *Chemical Physics* 298 (2004) 233
54. Billing, G.D., and Fisher, E.R., “VV and VT Rate Coefficients in N_2 by a Quantum-Classical Model”, *Chemical Physics* 43 (1979) 395
55. F. Esposito and M. Capitelli, “QCT calculations for the process $N_2(v) + N \longrightarrow N_2(v') + N$ in the whole vibrational range”, *Chemical Physics Letters* 418 (2006) 581
56. M. Cacciatore, A. Kurnosov, and A. Napartovich, “Vibrational Energy Transfer in N_2–N_2 collisions: A New Semiclassical Study”, *Journal of Chemical Physics*, 123 (2005) 174315
57. M. Simeni Simeni, B.M. Goldberg, C. Zhang, K. Frederickson, W.R. Lempert, and I.V. Adamovich, “Electric Field Measurements in a Nanosecond Pulse Discharge in Atmospheric Air”, *Journal of Physics D: Applied Physics* 50 (2017) 184002
58. A. C. Eckbreth, *Laser Diagnostics for Combustion Temperature and Species*, Cambridge, MA: Abacus Press, 1988, Chap. 6
59. M.M. Maricq, E.A. Gregory, C.T. Wickham-Jones, D.J. Cartwright, and C.J.S.M. Simpson, “Experimental and Theoretical Study of the Vibrational Relaxation of CO(v=1) and N_2(v=1): V-T Relaxation by the Isotopes of Helium”, *Chemical Physics* 75 (1982) 347
60. D.P. Shelton and J.E. Rice, “Measurements and Calculations of the Hyperpolarizabilities of Atoms and Small Molecules in the Gas Phase”, *Chemical Reviews* 94 (1994) 3
61. R.E. Palmer, “The CARSFT Computer Code for Calculating Coherent Anti-Stokes Raman Spectra: User and Programmer Information SAND89-8206”, Sandia National Labs, Livermore, CA, 1989
62. K. Takashima, Z. Yin, and I.V. Adamovich, “Measurements and Kinetic Modeling of Energy Coupling in Volume and Surface Nanosecond Pulse Discharges”, *Plasma Sources Science and Technology* 22 (2013) 015013

63. E.R. Jans, S. Raskar, X. Yang, and I.V. Adamovich, “Kinetics of Metastable $N_2(A^3\Sigma_u^+,v)$ Molecules in High-Pressure Nonequilibrium Plasmas”, *Plasma Sources Science and Technology* 30 (2021) 025003
64. D. Mignogna, E. Jans, S. Raskar, and I.V. Adamovich, “Generation and Decay of $N_2(A^3\Sigma_u^+)$ Molecules in Reacting CO_2 and CH_4 Plasmas”, AIAA Paper 2022-, AIAA Aerospace Sciences Meeting (SciTech 2021), 3-7 January 2021
65. Z. Yin, K. Takashima, and I.V. Adamovich, "Ignition Time Measurements in Repetitive Nanosecond Pulse Hydrogen-Air Plasmas at Elevated Initial Temperatures", *IEEE Transactions on Plasma Science* 39 (2011) 3288
66. A. Montello, Z. Yin, D. Burnette, I.V. Adamovich, and W.R Lempert, “Picosecond CARS measurements of nitrogen vibrational loading and rotational/translational temperature in nonequilibrium discharges”, *Journal of Physics D: Applied Physics* 46 (2013) 464002
67. J. Kuhfeld, N.D. Lepikhin, D. Luggenhölscher, and U. Czarnetzki, “Vibrational CARS measurements in a near-atmospheric pressure plasma jet in nitrogen: I. Measurement procedure and results”, J. Phys. D: Appl. Phys. 54 (2021) 305204
68. K. Frederickson, Y.-C. Hung, W.R. Lempert, and I.V. Adamovich, “Control of Vibrational Distribution Functions in Nonequilibrium Molecular Plasmas and High-Speed Flows”, *Plasma Sources Science and Technology* 26 (2017) 014002
69. X. Yang, E. Jans, C. Richards, S. Raskar, D. van den Bekerom, and Igor V. Adamovich, “Measurements of Atoms and Metastable Species in N_2 and H_2-N_2 Ns Pulse Plasmas”, accepted for publication in *Plasma Sources Science and Technology*, doi.org/10.1088/1361-6595/ac3053
70. J.J. Lowke, A.V. Phelps, and B.W. Irwin, “Predicted electron transport coefficients and operating characteristics of CO_2-N_2-He laser mixtures”, *Journal of Applied Physics* 44 (1973) 4664
71. A. Bogaerts, W. Wang, A. Berthelot, and V. Guerra, “Modeling plasma-based CO_2 conversion: crucial role of the dissociation cross section”, *Plasma Sources Science and Technology* 25 (2016) 055016
72. J.T. Herron, “Evaluated Chemical Kinetics Data for Reactions of $N(^2D)$, $N(^2P)$, and $N_2(A^3\Sigma_u^+)$ in the Gas Phase”, *Journal of Physical and Chemical Reference Data* 28 (1999) 14
73. G. Herzberg, “Molecular Spectra and Molecular Structure I. Spectra of Diatomic Molecules, Van Nostrand, Princeton, (1950).
74. L. S. Rothman, D. Jacquemart, A. Barbe, D. C. Benner, M. Birk, L. R. Brown, M. R. Carleer, C. Chackerian Jr, K. Chance, L. H. Coudert, V. Dana, V. M. Devi, J.-M. Flaud, R. R. Gamache, A. Goldman, J.-M. Hartmann, K. W. Jucks, A. G. Maki, J.-Y. Mandin, … G. Wagner, “The HITRAN 2004 Molecular Spectroscopic Database”, *Journal of Quantitative Spectroscopy and Radiative Transfer* (2005) (Vol. 96, Issue 2, pp. 139–204). Elsevier BV.
75. I. Suzuki, “General Anharmonic Force Constants of Carbon Dioxide”, *Journal of Molecular Spectroscopy* (1968) (Vol. 25, Issue 4, pp. 479–500). Elsevier BV.
76. T. Ida, M. Ando, & H. Toraya, “Extended Pseudo-Voigt Function for Approximating the Voigt Profile”, *Journal of Applied Crystallography* (2000). (Vol. 33, Issue 6, pp. 1311–1316). International Union of Crystallography (IUCr).

77. W.R. Lempert & I.V. Adamovich, “Coherent Anti-Stokes Raman Scattering and Spontaneous Raman Scattering Diagnostics of Nonequilibrium Plasmas and Flows” *J. Phys. D: Appl. Phys.* 47 (2014) 433001
78. I. Gulko, “Ns Pulse / RF Hybrid Plasmas for Plasma Chemistry and Plasma Assisted Catalysis Applications” Master’s Thesis, The Ohio State University (2020)

Appendix A: CO_2 VDF Inference Program

To infer the individual CO2 vibrational populations from the experimental QCL absorption spectrum, the algorithm described in [47] is implemented in several computer routines written in MATLAB. First, the rotational temperature is inferred from the spectra by the method of Boltzmann plots, as shown in Figure 3-7. For individual vibrational-rotational transitions within the same vibrational band,

$$-ln\left(\frac{I}{I_o}\right) = const * (J" + J' + 1)\, exp\left(\frac{-BJ''(J''+1)}{T}\right) \qquad (A1)$$

In Eq. (A1), the contribution of the stimulated emission from the upper state, which varies slightly over the rotational transitions, is neglected. As discussed in Ref. [47], at the present conditions this the effect is insignificant. In this formulation, $-ln\left(\frac{I}{I_o}\right)$, the line-integrated absorption coefficient, is measured directly in the experiment, while J', and J'' are the upper and lower rotational quantum numbers of the transition, respectively. This relation follows directly from the Boltzmann distribution over the rotational states, and is corrected for the rotational line intensity factors[73]), assuming equilibrium between the translational and rotational degrees of freedom. This assumption is valid after several mean collision times, i.e. on the time scales longer than ~ 10^{-9} s. The measurements are made several microseconds after the discharge pulse in this work, so this is applicable here. From eq (A1), it follows that

$$ln\left(\frac{-ln\left(\frac{I}{I_o}\right)}{J" + J' + 1}\right) = const + \frac{-BJ''(J''+1)}{T} \qquad (A2)$$

By plotting $ln\left(\frac{-ln\left(\frac{I}{I_0}\right)}{J"+J'+1}\right)$, which is measured, vs. the rotational energy, $-BJ''(J''+1)$, and fitting a straight line to the data, the temperature is inferred from the slope of the line, $1/T$. This procedure is repeated for the spectra taken at each time steps in the experiments, generating the time-resolved temperature in the discharge and the afterglow.

In practice, the proper selection of vibrational bands for which this procedure is applied is critical to ensure the accurate temperature inference. The rotational lines used for the Boltzmann plot should not overlap with lines from other vibrational bands, which could give the appearance of stronger absorption than in reality. In carbon dioxide and other polyatomic molecules, this presents a challenge, since absorption and emission on multiple vibrational bands can produce a very crowded spectrum when the mixture becomes vibrationally excited or when the temperature increases. Additionally, if the temperature is to be measured in the discharge afterglow, the vibrational bands used for the temperature inference should have slow relaxation rates or belong to a stable species. Otherwise, the transitions would not be detectable once the discharge power is turned off, and the temperature could not be inferred. For this work, the ground vibrational ground state of carbon monoxide, CO(v=0), was used, because the individual rotational lines are well separated, and because CO is a stable species, such that the absorption lines persist in the afterglow, after CO is generated during the discharge burst.

Another consideration is the selection of proper rotational lines, once the vibrational band is chosen. The energy spacing of the chosen lines should be greater than the temperature, several rotational transitions should be used for higher accuracy. For this work, ground state CO rotational transitions R(1), R(7), R(15), and R(17) in the CO(v=0 ⟶1) vibrational band were studied, with the total rotational energy spacing of approximately 900 K, In addition, as the lowest energy vibrational state of CO_2, (01^10), rotational transitions with lines P(54), P(64), P(65), P(73), and P(74) of the CO_2 vibrational band CO_2 ($01^10 \longrightarrow 01^11$), with the total energy spacing of approximately 1600 K, were used as an alternative temperature inference method. The uncertainty in the temperature is based on the standard deviation of the linear fitted slope, reported which is an output of by the built-in MATLAB function *regress*. To convert the standard deviation of the slope (-1/T) into the temperature inference, the error propagation is applied to obtain

$$\Delta T = T^2 \Delta \left(\frac{1}{T}\right) \tag{A3}$$

An illustration of this Boltzmann plot method is shown in Figure 3-7. For this work, the rotational temperatures inferred from the 2 different vibrational bands agree to within their combined uncertainty. The temperature inferred from the CO absorption spectra follows the rotational temperature inferred from the CARS spectra more faithfully where the discrete CARS spectra are available. This is likely due to the fact that there are no overlapping CO rotational transitions at these conditions, as opposed to carbon dioxide lines, as discussed previously. As a result, the rotational temperature inferred from CO lines is preferred and used for the remainder of the data processing. An implementation of this routine can be found in the file *T_rot.m* which outputs the rotational temperature and uncertainties, and prints GIF files to visualize temporal evolution.

With the rotational temperature in hand, attention is turned to the inference of the individual vibrational populations for both CO and CO_2. Spectroscopic Data from the HITRAN HITEMP database is used to enable these calculations [74]. At a high level, to find absorption coefficients for isolated transitions, it is necessary to have the Einstein B coefficient for absorption, which can be calculated as:

$$B_{lu} = A_{ul}\frac{c^3}{8\pi h\nu^3}\frac{g_u}{g_l} \qquad (A4)$$

where A_{ul}, is the Einstein A coefficient, taken from the HITEMP data, h is Planck's constant, and ν is the transition frequency (in Hz). The degeneracies of the upper and lower states g_u and g_l can either be calculated from the rotational quantum numbers or taken directly from the HITEMP data. Since the reverse process of stimulated emission may be important at the conditions with strong vibrational excitation, it is important to consider its effects when calculating the absorption coefficient. This requires using the Einstein B coefficient for stimulated emission, which is conveniently related to B_{lu} as

$$B_{ul} = \frac{g_l}{g_u}B_{lu} \qquad (A5)$$

From there, the true absorption coefficient in cm^{-1} can be found as:

$$\alpha_\nu = \frac{h\nu_0}{c}\left(f_{r,l}n_lB_{lu} - f_{r,u}n_uB_{ul}\right)g(\nu-\nu_0) \qquad (A6)$$

where $g(\nu - \nu_o)$ is the line-shape function (in cm) and $f_{r,l}$ and $f_{r,u}$ are the rotational Boltzmann factors, which are found assuming the rotational-translational equilibrium. The vibrational level populations, n_l and n_u, can be inferred from the measured line-integrated absorption coefficients, if the rotational-translational temperature and the absorption line shape are known.

In practice, for carbon dioxide, this calculation presents a formidable challenge because of the large number of coupled vibrational states to consider, and because the spectral line broadening (dominated by the collisional broadening at the present conditions) causes significant overlap between the relevant transitions. To facilitate the efficient calculations a MATLAB code *non_eq_CO2.m* was written which contains the necessary spectroscopic properties and methods to calculate synthetic spectra and to match the experimental spectra by inferring the vibrational level populations. In particular, the code is written as a MATLAB class, which stores much of the relevant physical data as properties. Therefore, an object instance must be created and named, after which the methods can be used to carry out the necessary computations. The code is listed at the end of the appendix in Table A-2 and referenced by line number in the text.

To begin with, the HITEMP spectroscopic data are filtered and saved in a format optimized for repeated use by MATLAB. Because the HITEMP database contains extensive transition data for the 7 most abundant isotopologues of CO_2 over a wide spectral interval from 0 – 13,000 cm^{-1}**,** it is very large, occupying tens of GB, and not suited for repeated parsing and loading. Accordingly, the data are filtered to include only the transitions of the three most abundant isotopologues ($^{12}C^{16}O_2$, $^{13}C^{16}O_2$, $^{16}O^{12}C^{18}O$). Then the data are selected over a relatively narrowed spectral range, 2125 cm^{-1} to 2500 cm^{-1}, which covers the tuning range of the QCL used in this work. Further, this data is converted from ASCII format into a MATLAB-friendly *.mat* filetype which can be loaded and parsed more expeditiously. This file is saved as *CO_2_Hitran_Data.mat* and is loaded in line 14 of the routine, as the variable *Data*. This way, all relevant data is stored as a matrix in the program, where each row represents an individual rovibrational transition and the columns represent a particular parameter associated with that transition. The format of the original ascii files can be referenced in [74], and the description of each column of the converted data matrix is listed below in Table A-1.

Table A-1: Description of the HITRAN Data Imported to the Program

Column 1	Column 2	Column 3	Column 4
Molecule HITRAN ID	Isotopologue HITRAN ID	Transition Wavenumber, cm^{-1}	Reference Line Strength $cm^{-1}/(molecule*cm^{-2})$

Column 5	Column 6	Column 7	Column 8
Einstein A Coefficient s^{-1}	Air broadened HWHM cm^{-1}/atm	Self broadened HWHM cm^{-1}/atm	Lower State Total Energy cm^{-1}

Column 9	Column 10	Column 11	Column 12
Pressure-broadening temperature exponent dimensionless	Pressure shift cm^{-1}/atm	ν_1, upper	ν_2, upper

Column 13	Column 14	Column 15	Column 16
l_2, upper	ν_3, upper	r_3, upper	ν_1, lower

Column 17	Column 18	Column 19	Column 20
ν_2, lower	l_2, lower	r_3, lower	ν_3, lower

Column 21	Column 22	Column 23	Column 24
j, upper	j, lower	g, upper	g, lower

Other relevant physical constants and properties of carbon dioxide are loaded and stored as object properties in lines 8-16 of the routine.

In order to simplify the computations, it is essential to direct the program to consider the minimum number of vibrational states necessary to describe the experimental spectrum. With this in mind, the main routine requires a list specifying the states to consider. With no a priori knowledge of which states will be relevant, the first method of the class, *filterData-,* starting on line 21 will generate such a list, as well as reduce and sort the data matrix, retaining and grouping the rows only for the states it deems significant. These items are the output variables *list* and *band_data*, respectively. Generating these items requires the following inputs. *Limits* is a two - column array containing the starting and ending wavenumbers where the spectrum is recorded. If the spectrum is taken over *n* disjoint (separate) spectral regions, *n* rows can be appended to *limits,* describing the boundaries for each region. The program will neglect all transition data from outside these spectral boundaries. Since most lines that are weak in equilibrium will still be weaker than strong lines during excitation, the equilibrium line-strength is an effective parameter to filter the values. The input *cutoff* is a value for the equilibrium line strength in $cm^{-1}/(molecule{\cdot}cm^{-2})$ where bands which do not have transitions stronger than this value in the region of interest are not considered. An important exception to this is the case of a pure asymmetric stretch transition ($0,0,n \rightarrow 0,0,n+1$), where the bands are filtered by the parameter *upperv3*, rather than the linestrength cutoff. This is because of the expected preferential excitation of this mode in N_2/CO_2 plasmas. The output *list* is a cell array with the names of the relevant vibrational bands, while the output *filteredData* is a structure with 24-column fields like the *Data* property. The field names are taken from the names in *list* and the field values are rows from *Data* that correspond to the field name and satisfy the other criteria discussed above. This drastically reduces the amount of data to consider and organizes it for the program. The names of the bands in *list* follow the following format:

*band_iso_i*____$v_{1,u}$_ $v_{2,u}$_ $l_{2,u}$_ $v_{3,u}$___ $v_{1,l}$ _ $v_{2,l}$ _ $l_{2,l}$ _ $v_{3,l}$ where i is the HITRAN isotopologue ID, and the *v's* and *l's* are the vibrational quantum numbers of the lower and upper state respectively. Once the user has a grasp of which bands are important to describe the experimental spectrum, it is expeditious to save the list external to the program and to import it rather than regenerate it with each use which would re-parsing the entire transition data file. In this case, the method *get_band_data* on line 79 will take such a list as an input, as well as spectral limits such as described above and produce the output of filtered data in a grouped structure.

The spectral inference routine not only requires the list of vibrational bands but it also needs to identify the upper states of the transitions involved and to map the lower states to the upper states. For this quantum cascade laser in the 4.3 μm range, the upper state always has the quantum number of the asymmetric stretch mode exceeding by 1 that for the lower state. Accordingly, generating a list of the upper states is straightforward. The method *upper_states* on line 116 takes the lower state list as input and outputs the *upper_state_list* which is an isomorphic list of the corresponding upper states. With the upper state names in hand attention is turned to generating a map identifies the index of the corresponding upper state for each lower state entry in the list. Inputting the lower and upper state lists to the method *map* on line 133 will generate a column vector of integers the same length as the list, where the map entry corresponding to a lower state represents the index of the upper state in the list. Since there is a finite number of the asymmetric stretch levels considered, there will inevitably come a point when the upper state for a band is not included in the list. When this occurs, the program fills in the map entry with a 0, and this is handled by the spectral inference routine which will be discussed in the next section. Examples showing the creation and use of these variables are printed below.

```
CO2 = non_eq_CO2% create the class object with all the relevant propeties and methods

line_cutoff = 1e-23; %intenity cutoff

upper_v3 = 3; %highest level of asymmetric stretch considered

[Vib_band_data, Vib_band_list] = ...
    CO2.filterData(split_lim, line_cutoff, upper_v3)%create the list and data

split_lim %spectral limits to consider [cm^-1]
```

```
CO2 = 

  non_eq_CO2 with properties:

                     c: 299792458
                    kb: 1.3807e-23
                     h: 6.6261e-34
              CO2_mass: 7.3065e-26
        heavy_CO2_mass: 7.4726e-26
                 B_rot: 0.5631
                  Data: [1356269×24 double]
          CO2_energies: [11×16×22×16 double]
    heavy_CO2_energies: [11×16×22×6 double]


Vib_band_data = 

  struct with fields:

    band_iso_1____0_0_0_1___0_0_0_0: [2×24 double]
    band_iso_1____0_0_0_2___0_0_0_1: [3×24 double]
    band_iso_1____0_0_0_3___0_0_0_2: [3×24 double]
    band_iso_1____0_0_0_4___0_0_0_3: [3×24 double]
    band_iso_1____0_1_1_1___0_1_1_0: [5×24 double]
    band_iso_1____0_2_2_1___0_2_2_0: [5×24 double]
    band_iso_1____0_3_3_1___0_3_3_0: [5×24 double]
    band_iso_1____1_0_0_1___1_0_0_0: [3×24 double]
    band_iso_1____1_1_1_1___1_1_1_0: [6×24 double]
    band_iso_1____1_2_2_1___1_2_2_0: [2×24 double]
    band_iso_1____2_0_0_1___2_0_0_0: [1×24 double]
    band_iso_2____0_0_0_1___0_0_0_0: [4×24 double]
```

```
    band_iso_2____0_0_0_2___0_0_0_1: [4×24 double]
    band_iso_2____0_0_0_3___0_0_0_2: [8×24 double]
    band_iso_2____0_1_1_1___0_1_1_0: [7×24 double]
    band_iso_2____0_2_2_1___0_2_2_0: [9×24 double]
    band_iso_2____1_0_0_1___1_0_0_0: [5×24 double]
    band_iso_3____0_0_0_1___0_0_0_0: [5×24 double]
    band_iso_3____0_0_0_2___0_0_0_1: [6×24 double]
    band_iso_3____0_0_0_3___0_0_0_2: [8×24 double]
    band_iso_3____0_0_0_4___0_0_0_3: [12×24 double]
    band_iso_3____0_1_1_1___0_1_1_0: [8×24 double]


Vib_band_list =

  25×1 cell array

    {'band_iso_1____0_0_0_1___0_0_0_0'}
    {'band_iso_1____0_0_0_2___0_0_0_1'}
    {'band_iso_1____0_0_0_3___0_0_0_2'}
    {'band_iso_1____0_0_0_4___0_0_0_3'}
    {'band_iso_1____0_1_1_1___0_1_1_0'}
    {'band_iso_1____0_2_2_1___0_2_2_0'}
    {'band_iso_1____0_3_3_1___0_3_3_0'}
    {'band_iso_1____1_0_0_1___1_0_0_0'}
    {'band_iso_1____1_0_0_1___1_0_0_0'}
    {'band_iso_1____1_1_1_1___1_1_1_0'}
    {'band_iso_1____1_1_1_1___1_1_1_0'}
    {'band_iso_1____1_2_2_1___1_2_2_0'}
    {'band_iso_1____2_0_0_1___2_0_0_0'}
    {'band_iso_2____0_0_0_1___0_0_0_0'}
    {'band_iso_2____0_0_0_2___0_0_0_1'}
    {'band_iso_2____0_0_0_3___0_0_0_2'}
    {'band_iso_2____0_1_1_1___0_1_1_0'}
    {'band_iso_2____0_2_2_1___0_2_2_0'}
    {'band_iso_2____1_0_0_1___1_0_0_0'}
    {'band_iso_2____1_0_0_1___1_0_0_0'}
    {'band_iso_3____0_0_0_1___0_0_0_0'}
    {'band_iso_3____0_0_0_2___0_0_0_1'}
    {'band_iso_3____0_0_0_3___0_0_0_2'}
    {'band_iso_3____0_0_0_4___0_0_0_3'}
    {'band_iso_3____0_1_1_1___0_1_1_0'}


split_lim =

   1.0e+03 *

    2.2726    2.2755
    2.2851    2.2879
```

```
upper = CO2.upper_states(Vib_band_list) %list of upper states
```

```
upper =

  25×1 cell array

    {'band_iso_1____0_0_0_2___0_0_0_1'}
    {'band_iso_1____0_0_0_3___0_0_0_2'}
    {'band_iso_1____0_0_0_4___0_0_0_3'}
    {'band_iso_1____0_0_0_5___0_0_0_4'}
    {'band_iso_1____0_1_1_2___0_1_1_1'}
    {'band_iso_1____0_2_2_2___0_2_2_1'}
    {'band_iso_1____0_3_3_2___0_3_3_1'}
    {'band_iso_1____1_0_0_2___1_0_0_1'}
    {'band_iso_1____1_0_0_2___1_0_0_1'}
    {'band_iso_1____1_1_1_2___1_1_1_1'}
    {'band_iso_1____1_1_1_2___1_1_1_1'}
    {'band_iso_1____1_2_2_2___1_2_2_1'}
    {'band_iso_1____2_0_0_2___2_0_0_1'}
    {'band_iso_2____0_0_0_2___0_0_0_1'}
    {'band_iso_2____0_0_0_3___0_0_0_2'}
    {'band_iso_2____0_0_0_4___0_0_0_3'}
    {'band_iso_2____0_1_1_2___0_1_1_1'}
    {'band_iso_2____0_2_2_2___0_2_2_1'}
    {'band_iso_2____1_0_0_2___1_0_0_1'}
    {'band_iso_2____1_0_0_2___1_0_0_1'}
    {'band_iso_3____0_0_0_2___0_0_0_1'}
    {'band_iso_3____0_0_0_3___0_0_0_2'}
    {'band_iso_3____0_0_0_4___0_0_0_3'}
    {'band_iso_3____0_0_0_5___0_0_0_4'}
    {'band_iso_3____0_1_1_2___0_1_1_1'}
```

```
map = CO2.map(Vib_band_list, upper) %map lower to upper states
```

```
map =


     2
     3
     4
     0
     0
     0
     0
     0
     0
```

```
 0
 0
 0
 0
15
16
 0
 0
 0
 0
 0
22
23
24
 0
 0
```

Example A-1: Creation of the Inputs for the Spectral Synthesis

With the reduced set of HITRAN data, the vibrational state list and map to the upper states in hand, attention can be turned to extracting the individual populations from the spectrum. The critical method in the whole routine is *vdf* on line 152. To run this function requires the wavenumber grid, the experimental spectrum, temperature, pressure, carbon dioxide mole fraction,the filtered data, list, and map as discussed above. The routine operates by calculating the synthetic spectrum which minimizes the least squares residual relative to the experiment. It also outputs the individual absorption path-integrated populations and uncertainties corresponding to the list entries in cm^{-2} (i.e. populations times absorption path). The spectral inference using the data from the example above is continued in the snippet below. To improve the spectral fit, a larger number of vibrational bands should be used, as several absorption lines are ‘missed’ in this demonstration (see Figure A-1).

```
L = size(abs);
rot_temp = load(temp_file); %load previoulsy calculated temperatures
num_of_var = length(Vib_band_list);
abs_syn = 0*abs;
pops = zeros(num_of_var, L(2),2);
Tv3 = zeros(L(2),2);
Tv12 = zeros(L(2),2);
ind_v3 = [1,2]; %this requires some prior knoweldge of the list structure
ind_v12 = [1,5,7,9];
abs;%abs is the experimentally measured aboprtion signal
bg = abs(:,1)*14/23; %path length correction for ground state

for i = 226

    tH = rot_temp(i,2);
    ex_spec = abs(:,i) - bg;

    [syn_spec, populations, uncertainties] = ...
        CO2.vdf(wv,ex_spec,tH,P,X,Vib_band_data, Vib_band_list,map); %calculate vdf

    abs_syn(:,i) = syn_spec;
    pops(:,i,1) = populations;
    pops(:,i,2) = uncertainties;

end

figure()
p = i;
plot(wv,abs(:,p)-bg,'k')
hold on
plot(wv,abs_syn(:,p),'r')
xlabel('Wavenumbers, [cm^-^1]')
ylabel('Absorbance, \alpha*L')
Axisformat(1,10)
ylim([-0.05,2.5])
s = breakxaxis([2275.5, 2284.9]);
l = s.leftAxes;
legend(l,'experiment','synthetic','box','off')
```

Example A-2: Use of the Spectral Synthesis Routine

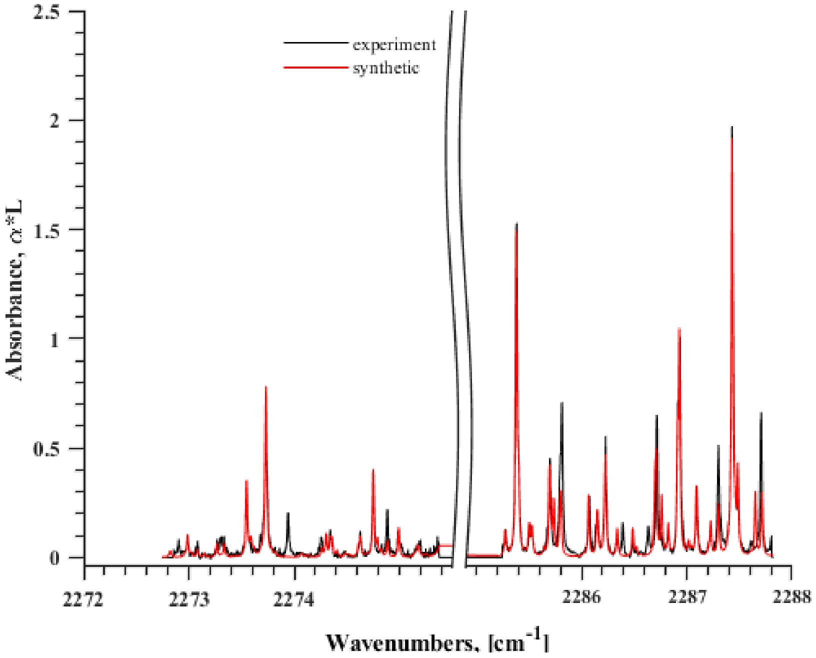

Figure A-1: Synthetic Spectrum Ourptut of Example A. 2

In this implementation, the synthetic spectrum is expressed as:

$$L * \sum \alpha_\nu = L * \frac{h\nu_0}{c} \sum \left[\left(g(\nu - \nu_0) f_{r,l} B_{lu} \right) * n_l - \left(g(\nu - \nu_0) f_{r,u} B_{ul} \right) * n_u \right] \quad (A7)$$

For each vibrational band specified in the list the program computes the spectral absorption coefficient, α(ν), using the data inside its ‘bin’. For each rotational line in the vibrational band the relevant data is extracted in lines 173-193, with the column description called out in Table A-1. The first item to calculate is the rotational Boltzmann factor. This parameter can be expressed simply as:

$$f_r = \frac{(2J'' + 1)}{Q_r} \exp\left(-\frac{E''}{kT} \right) \qquad (A8)$$

where J’’ is the lower state rotational quantum number, Q_r is the rotational partition function, and E’’ is the lower state rotational energy. J’’ is taken directly from the HITRAN data, while Q can be computed simply using the approximation given in [73] since $B/T \ll 1$,

$$Q_r = \frac{kT}{hcB} \tag{A9}$$

Since the HITRAN data lists the total rovibrational energy of the lower state for each transition, it is necessary to remove the vibrational energy to find the rotational contribution. The vibrational energies (in cm^{-1}) are stored as object properties in a 4-D array, and can be looked up by the vibrational quantum numbers (plus one) as done in lines 195 -208. Because the energies are slightly different for different isotopolgues, it is important to discriminate between them when retrieving the data. This is why there are two energy arrays loaded and named as object properties in lines 15-16, one for $^{12}C^{16}O_2$, and one for $^{13}C^{16}O_2$. The energies are saved in units of cm^{-1}. Because such energy tables were not readily available for access and use, they were created following the procedure and parameter values given in [75].

After the boltzmann fraction is calculated in lines 213-215, the lineshape of the transistion requires attention. Firstly, the collision-induced shift of the line center is addressed in line 212 using the HITRAN shift parameter and the experiment pressure. Next, a Voight line shape profile is calculated from the temperature, pressure, HITRAN broadening parameters, molecular mass, and the shifted transition location. In particular, a psuedo-Voight profile is used to speed up the calculations, as the computation of an actual Voight shape is extremely computationally expensive, and the program would run for several days at a time to accomplish this task for the many lines involved. The details of this particular implementation are described in [76], but ultimately it is merely a linear combination of Gaussian and Lorentzian profiles, accurate to within 1% of the exact Voight profile. The MATLAB implementation is contained in the separate function files *psuedo_voigt.m*, *gaussian.m*, and *lorentzian.m*. The transition lineshape is calculated in lines 216-218 over the entire spectral mesh, and centered at the shifted center.

To calculate the Einstein B (absorption and stimulated emission) coefficients, the program begins from the HITRAN Einstein A (spontaneous emission) coefficient and converts to the Einstein coefficient for absorption for the lower state,

$$B_{lu} = A_{ul} \frac{c^3}{8\pi h\nu^3} \frac{g_u}{g_l} \qquad (A10)$$

The Einstein coefficient for stimulated emission from the upper state is related to B_{lu} as follows:

$$B_{ul} = B_{lu} \frac{g_l}{g_u} \qquad (A11)$$

Now, all of the parameters used in Eqn. A-7 have been found, except for the number densities (vibrational level populations). The resultant units of the number density scaling factors after before incorporting the path length are cm^2, so that the units of number density are cm^{-3} after dividing out path length.

This process is repeated for all rotational lines in the vibrational band appearing in the spectral interval considered, adding the individual cross sections for rotational lines together to create the characteristic ‘band shape’ cross section [cm^2] in line. Because equation A-7 demonstrates that the integrated spectral absorption coefficient actually depends on population differences (lower minus upper), a subtractive cross section is also created with each loop, which only differs from the additive cross section by the upper state boltzmann fraction and the Einstein coefficient for stimulated emission, B_{ul}. The cross sections are created on lines 219 and 225. Finally, all of the above steps are repeated for all of the vibrational bands considered. Equation A-7 represents a system of coupled linear equations that can be solved for the number densities, however, it is necessary to assume the the upper state of the highest detected vibrational band has zero populations in order to complete the set of equations. For example, consider a pedagogical spectrum where only the first four levels of the asymmetric stretch vibrational mode of the main isotopologue of CO_2 contribute. The spectrum is saved as the column vector S. The program then computes the additive and subtractive absorption cross sections, α^+ and α^- as column vectors, for states 00^00, 00^01, 00^02, and 00^03, ignoring 00^04. Using this notation, the system of equations to solve is:

$$S = \ [\alpha_0^+, (\alpha_1^+ - \alpha_0^-\ ), (\alpha_2^+ - \alpha_1^-), (\alpha_3^+ - \alpha_2^-\ )\ ] \begin{bmatrix} n_0 \\ n_1 \\ n_2 \\ n_3 \end{bmatrix} \qquad (A12)$$

To solve the equations, a modified MATLAB routine *regress_non_neg* is used which is based on the built-in routine *regress,* modified to force positive values for the outputs. This routine solves the system of equations A12 by calculating the number densities, n_i, that minimize the least-squares residuals. Besides outputting the populations for the vibrational bands of interest, this routine also outputs the 95% confidence intervals for the inferred population values. These confidence intervals are divided by two and interpreted as the standard deviation (uncertainty of the inferred value). The number densities and uncertainties are output as column vectors with the same length as the input list. The identity of one of the entries in the output can then be found by looking up the name from the list entry at the same index. The routine also outputs the synthetic spectrum, which is simply the result of the matrix multiplication in eqn. A12 using the vibrational level populations calculated by the program. The synthetic spectra are computed in lines 238-242.

The final, ‘supplemental’ methods are useful for calculating the vibrational temperatures of different modes. The method *get_Energy* on line 247 will take the vibrational state list as an input and output an array of corrresponding vibrational energies in Kelvin. The method *getTv* on line 268 can then be used to calculate a vibrational temperature with the Boltzmann plot method by taking in the output of the *vdf* routine, the indices of which states to consider, and the state list. Proper use will require some prior knowledge of the list structure, if different modes are not anticipated to be in equilibrium. The snippet below illustrates its proper usage and ouptut. To convert the slope uncertainty of the Boltzmann plot to the vibrational temperature uncertainty, the same eqn, A-3 must be used, as derived during the discussion of the rotational temperature.

```
Vib_energies = CO2.get_Energy(Vib_band_list) %get the state energies
ind_v12 = [1,5,6]; %indices of first three pure bendidng states.
[Tv012, dSlope012] = CO2.getTv...%getting temperature and slope uncertainty
    (populations,ind_v12, Vib_band_list, Vib_energies)
```

```
Vib_energies =

   1.0e+04 *

    0.3643
    0.7023
    1.0367
    1.3675
    0.4597
    0.5537
    0.6465
    0.5563
    0.5563
    0.6509
    0.6509
    0.7443
```

```
    0.7473
    0.3568
    0.6853
    1.0105
    0.4502
    0.5441
    0.5488
    0.5488
    0.3568
    0.6853
    1.0105
    1.3323
    0.4502


Tv012 =

  438.3947


dSlope012 =

  557.9961
```

The virtue of reducing spectra in this manner is that indivdual vibrational level populations can be inferred for the conditions where there is non-equilibrium between between different vibrational energy modes, or when there is non-Boltzmann distribution within a given vibrational mode (e.g. due to the anharmonic V-V pumping). However, to validate the technique and implementation, it is necessary to compare the results against a benchmark. To do this, the HITRAN User Application Programming Interface (HAPI) was used to generate a synthetic CO_2 spectrum in thermal equilibrium at T = 600 K and P = 100 Torr from 2285 to 2290 cm^{-1}. This spectrum was processed using the custom routine described above to infer the vibrational populations, anticipating a Boltzmann distribution at 600 K. The results are shown in Figure A-2 below.

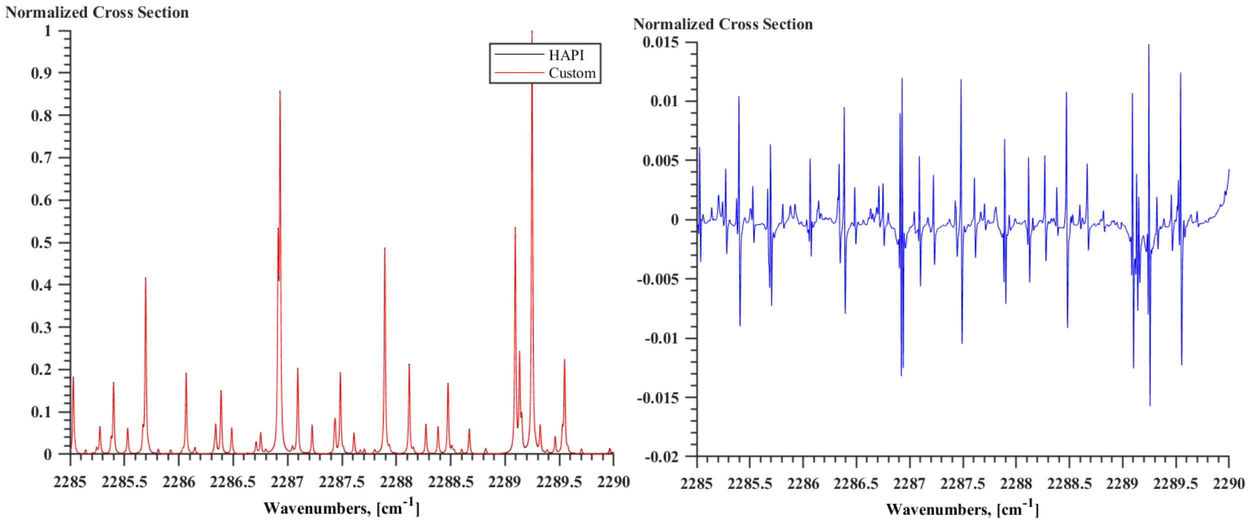

Figure A-2: Comparison of Equilibrium HAPI Spectrum to fit (a), and Residuals (b)

From Figure A-2, it can be seen that the synthetic spectum recreates the HAPI equilibrium spectrum, with less than 2% error. The inferred vibrational populations are plotted versus vibrational energy in Figure A. 3. By fitting a line to the data points, the vibrational temperature is calculated to be 589 ± 10 K, indicating that the routine is implemented correctly and the output is acceptable for use.

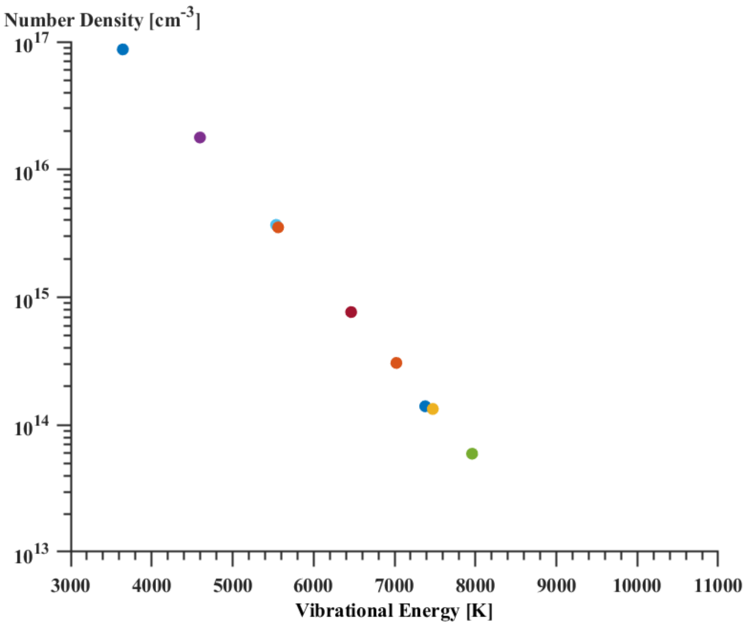

Figure A-3 VDF Inferred by Computing the Synthetic Spectrum Shown in Figure A. 2

The full MATLAB class source code is listed below in Table A-2.

Table A-2: MATLAB Code Implementing Procedures Discussed in Appendix A

```
classdef non_eq_CO2


    properties

        %physical constants

        c = 2.99792458e8; %meters/sec
        kb = 1.38065e-23;  %J/K
         h = 6.62607004e-34; %J*s
         CO2_mass = 7.306542676851544e-26;% kg, 44amu/N_a
         heavy_CO2_mass =  7.472600464961807e-26; % kg, 45 amu/N_a
         B_rot = 0.5631; %Kelvin, B_e
         Data = load('CO2_Hitran_Data_1st3_iso.mat','Data').Data; %see parseHTCO2 for
             explanation of each column
         CO2_energies = load('CO2_v_energies.mat','E').E;%energies in wavenumbers
         heavy_CO2_energies = load('heavy_CO2_v_energies.mat','E').E;%energies in wavenumbers
     end
```

```

    methods

        function [band_data, list] = filterData(obj, limits, cutoff, upperv3)

            %filterData will determine which vibrational are relevant based
            %on the wavelength ranges defined by limits and an intensity cutoff, cutoff,
            % list; cell array of strings which have the quantum number of
            %   each band in them
            % band_data; structure with fields named after their list entry
            %   and the line data for each line in the wavelength range


            band_data = struct();
            FilteredData = [];
            sz = size(limits);
            scan_regions = sz(1);
            for i = 1:scan_regions

                %finds linds that occur in the interval studied and are
                %either 'strong' lines or are pure asymmetric stretch lines
                ind_that_matter = find(((obj.Data(:,4)>cutoff)|((obj.Data(:,16)==0) &
                    (obj.Data(:,17)==0)...
                     &(obj.Data(:,18)==0) & (obj.Data(:,19)<=upperv3) &(obj.Data(:,11)==0)
                    &(obj.Data(:,12)==0)...
                     &(obj.Data(:,13)==0)))& (obj.Data(:,3)>limits(i,1)) &
                    (obj.Data(:,3)<limits(i,2)));
                FilteredData = [FilteredData; obj.Data(ind_that_matter,:)];
            end
            FilteredData = unique(FilteredData,'rows'); %Removing Duplicates due to overlap


            %finding unique vibrational bands and grouping lines in the band
            %accordingly
            b = FilteredData(:,[2,11:20]);
            b = unique(b, 'rows');
            list = cell(length(b(:,1)),1);
            for i = 1:length(b(:,1))
                %ignoring quantum number 'r' for now
                id = [num2str(b(i,2)),',',num2str(b(i,3)), '_',num2str(b(i,4)),...
                    ',',num2str(b(i,5)),'___',num2str(b(i,7)),',',num2str(b(i,8)),...
                    '_',num2str(b(i,9)),',',num2str(b(i,10))];
                isotope = num2str(b(i,1));
                pf = ['band_iso_',isotope,'____'];
                v = matlab.lang.makeValidName(id,'Prefix',pf);
                eval([v '= zeros(size(FilteredData));']);
                list{i} = v;
                l = 1;
                for k = 1:length(FilteredData(:,1))

                    if FilteredData(k,[2,11:20]) == b(i,:)

```

```
                eval([v '(l,:) = FilteredData(k,:);']);
                l=l+1;

            end

        end
        eval([v '( all(~' v ',2), : ) = [];']);
        eval(['band_data.' v '=' v ';']);

    end
end

function band_data = get_band_data(obj, list, limits)


    for i = 1:length(list)
        %ignoring quantum number 'r' for now
        id = list{i};
        parts = char(strsplit(id,'_'));
        sz = size(limits);
        scan_regions = sz(1);
        FilteredData = [];
        for k = 1:scan_regions
        ind = find(obj.Data(:,2)== str2double(parts(3)) &
           obj.Data(:,11)==str2double(parts(4)) &...
            obj.Data(:,12)==str2double(parts(5)) &             2
           obj.Data(:,13)==str2double(parts(6)) &...
            obj.Data(:,14)==str2double(parts(7)) &
           obj.Data(:,16)==str2double(parts(8)) &...
            obj.Data(:,17)==str2double(parts(9)) &
           obj.Data(:,18)==str2double(parts(10)) &...
            obj.Data(:,19)==str2double(parts(11)) & (obj.Data(:,3)>limits(k,1))...
            & (obj.Data(:,3)<limits(k,2)));
            FilteredData = [FilteredData; obj.Data(ind,:)];
        end

        FilteredData = unique(FilteredData,'rows'); %Removing Duplicates due to
           overlap
         %v = matlab.lang.makeValidName(id);
         eval([id '= zeros(size(FilteredData));']);
         l = 1;
         for k = 1:length(FilteredData(:,1))

                 eval([id '(l,:) = FilteredData(k,:);']);
                 l=l+1;

         end
         eval([id '( all(~' id ',2), : ) = [];']);
         eval(['band_data.' id '=' id ';']);
     end


```

```
        end

        function upper_state_list = upper_states(obj,band_list)

            num = length(band_list);
            upper_state_list = cell(num,1);
            for i = 1:num
               lower = band_list{i};
               parts = strsplit(lower,'_');
               nu3_lower = str2double(parts{11});
               nu3_upper  = nu3_lower + 1;
               nu3_upper_upper = nu3_upper + 1;
               parts{11} = num2str(nu3_upper);
               parts{7} = num2str(nu3_upper_upper);
               underscores = {'_','_','____','_','_','_','___','_','_','_'};
               upper_state_list{i} = strjoin(parts,underscores);
            end
        end

        function map_to_upper_state = map(obj, lower_list, upper_list)

           num = length(lower_list);
           map_to_upper_state = zeros(num,1);
           for i = 1:num

               upper = upper_list{i};

               for p = 1:num

                   lower = lower_list{p};
                   if strcmp(upper, lower)
                       map_to_upper_state(i) = p;
                   end
               end

           end
        end

        function [syn_spec, populations, uncertainties] = vdf(obj,grid, spectra, temperature,
           pressure, mole_frac, band_data, band_list, map)

            num_of_bands = length(band_list);
            num_of_pts = length(spectra);
            mat = zeros(num_of_pts,num_of_bands);%initializing matrix
            temp_curr = temperature; %temperature [K]
            P = pressure; %pressure [atm]
            X = mole_frac; %CO2 mole fraction
            X_air = 1 - mole_frac; %diluent mole fraction
            wv = grid;              %spectral axis, cm^-1
            for v = 1:num_of_bands %loops through the vibrational states...
                %specified in the list

```

```
            band = band_list{v}; %name of the vibrational state at hand
            current_band = []; %initialize the current vibrational state data variable
            eval(['current_band = band_data.',band,';']) %extract band data
            lines = length(current_band(:,1)); %get number of rotational lines
            band_shape = zeros(num_of_pts,1);   %initialize the cross-section
            band_shape_sub = zeros(num_of_pts,1); %initialize the subtractive cross-section
            for j = 1:lines %loop through lines in the current vibrational  band

                line_data = current_band(j,:); %import the data for the current line
                iso = line_data(2); %isotoplogue number
                center = line_data(3); %transistion wavenumber
                A = line_data(5); %A coefficient s^-1
                g_air = line_data(6); %Air broadened HWHM cm-1/atm
                g_self = line_data(7); %Self broadened HWHM cm-1/atm
                E_lower = line_data(8); %Lower State Total Energy cm-1
                n = line_data(9);% pressure broadening coefficient, dimensionless
                shift = line_data(10);%pressure-induced shift, cm^-1 / atm
                nu1_upper = line_data(11);%upper state symmetric stretch level
                nu2_upper = line_data(12);%upper state bending level
                nu3_upper = line_data(14);%upper state asymmetric stretch level
                l_upper = line_data(13);%upper state angular momentum number
                nu1_lower = line_data(16);%upper state symmetric stretch level
                nu2_lower = line_data(17);%upper state bending level
                nu3_lower = line_data(19);%upper state asymmetric stretch level
                l_lower = line_data(18);%upper state angular momentum number
                j_lower = line_data(21);%lower state rotational level
                j_upper = line_data(22);%upper state rotational level
                g_lower = line_data(23);%lower state degeneracy
                g_upper = line_data(24);%upper state degeneracy

                if iso == 1 %main isotopologue
                    E_vib = (obj.CO2_energies(nu1_lower+1, nu2_lower + 1, nu3_lower + 1,l_lower+1)...
                      - obj.CO2_energies(1,1,1,1)); %lower state vibrational energy , cm^-1
                    E_vib_upper = (obj.CO2_energies(nu1_upper+1, nu2_upper + 1, nu3_upper + 1,l_upper+1)...
                      - obj.CO2_energies(1,1,1,1)); %upper state vibrational energy , cm^-1
                    mass = obj.CO2_mass;    %mass

                else %heavy isotopologues
                    E_vib = (obj.heavy_CO2_energies(nu1_lower+1, nu2_lower + 1, nu3_lower + 1,l_lower+1)...
                      - obj.heavy_CO2_energies(1,1,1,1));%lower state vibrational energy , cm^-1
                    E_vib_upper = (obj.heavy_CO2_energies(nu1_upper+1, nu2_upper + 1, nu3_upper + 1,l_upper+1)...
                      - obj.CO2_energies(1,1,1,1)); %upper state vibrational energy , cm^-1
                    mass = obj.heavy_CO2_mass;  %mass
```

```
                    end


                    wvl = 1/center; %transition wavelength [cm]
                    center_shifted = center + shift*P; %shifted transition location [cm^-1]
                    E_r = (E_lower - E_vib)*obj.c*100*obj.h/obj.kb; % lower state rot. energy in Kelvin
                    Q_r = obj.kb*temp_curr/(obj.h*obj.c*100*obj.B_rot); %rotational partition function
                    f_r = (2*j_lower + 1)*exp(-E_r/temp_curr); %lower state rotational Boltzmann fraction
                    broadening = [g_air, n, X_air; g_self, n, X]; %array for the lineshape function
                    lineshape = pseudo_voight(center_shifted,temp_curr,mass,P,broadening,wv); %lineshape,cm
                    lineshape = lineshape/(100*obj.c); %linsehape, seconds
                    xs = A*lineshape*(wvl^2)*f_r*g_upper/g_lower/(Q_r*8*pi); %additive cross-section cm^2
                    band_shape = band_shape + xs; %cumulative additive vibrational state cross section

                    E_upper = E_lower + center; %upper state energy
                    E_r_upper = (E_upper - E_vib_upper)*obj.c*100*obj.h/obj.kb;% upper state rot. energy in Kelvin
                    f_r_upper = (2*j_upper + 1)*exp(-E_r_upper/temp_curr); %upper state rotational boltzmann fraction
                    xs_sub = A*lineshape*(wvl^2)*f_r_upper/(Q_r*8*pi); %subtractive cross-section cm^2
                    band_shape_sub = band_shape_sub + xs_sub;%cumulative subtractive vibrational state cross section, cm^2

                end

                mat(:,v) = mat(:,v) + band_shape; %filling in the matrix column with additive cross-section
                u = map(v);
                if u ~= 0
                   mat(:,u) = mat(:,u) - band_shape_sub; %filling in the matrix column with subtractive cross-section
                end

            end

            rhs = spectra; %experimental spectra
            [rp, u] = regress_non_neg(rhs,mat); %solve linear equations w/ positive solution
            uncertainties  = abs((u(:,1) - u(:,2))/2); %get the 95% confidence interval
            populations = rp; %rename for output
            syn_spec = mat*rp; %calculate synthetic spectrum


        end

```

```matlab
        function vibrational_energies = get_Energy(obj,band_list)
           E_vib = zeros(length(band_list),1);
           for j = 1:length(band_list)
                id = band_list{j};
                parts = strsplit(id,'_');
                iso = str2double(char(parts(3)));
                s = str2double(char(parts(8)));
                b = str2double(char(parts(9)));
                l = str2double(char(parts(10)));
                a = str2double(char(parts(11)));
                if iso == 1
                    E_vib(j) = obj.CO2_energies(s+1, b+1, a+1,l+1)...
                           *100*obj.c*obj.h/obj.kb;
                else
                    E_vib(j) = obj.heavy_CO2_energies(s+1, b+1, a+1,l+1)...
                           *100*obj.c*obj.h/obj.kb;
                end
           end
           vibrational_energies = E_vib;
        end

        function [vib_temp, uncertainty] = getTv(obj, populations, indices, band_list, energies)

            pops = zeros(length(indices),1);
            E_vib = zeros(length(indices),1);
            p = 1;
            k = 1;
            while p <=length(indices)

                if populations(indices(p)) == 0
                    pops(k) = [];
                    E_vib(k) = [];
                else
                    pops(k) = populations(indices(p));
                    E_vib(k) = energies(indices(p));
                    k=k+1;
                end

                p = p+1;

            end

            mat = [E_vib, ones(length(pops),1)];
            yvec = log(pops);
            [s, ci] = regress(yvec,mat);
            vib_temp = -1/s(1);
            ci = (ci(:,2) - ci(:,1))/2;
            uncertainty = abs(vib_temp*ci(1)/s(1));

        end

```

```
    end
end
```

Appendix B: Operation of Hybrid Plasma and QCL System

B.1 Hybrid Plasma Circuitry

To enable further investigation into the effect of adding vibrational excitation to molecular species in the plasma, operation and maintenance of the existing external circuit combining a ns pulse train and RF waveform is of critical importance. Furthermore, understanding the principles of the circuit operation is necessary to ensure the ability to adapt and troubleshoot as different difficulties present themselves. The circuit diagram is shown in Figure B-1. The overlap of a ns-pulse train with an RF waveform is needed to selectively couple the discharge input energy to the vibrational energy modes of molecules in the plasma. This requires the integration of commercial pulsers and RF sources into a single circuit, while isolating the power supplies from each other to prevent damage. The basic idea is to use high-power diodes to guide the respective waveforms to the discharge cell and block them from the opposing power sources. For a single polarity pulsed power source such as MegaImpulse NPG 100k, this can be accomplished with the use of high-voltage diodes connected in series to withstand the high peak voltage pulses. D2 in Figure B-1 prevents the ns pulses from reaching the RF or DC power supplies which is composed of 25 avalanche diodes in series described in Table B-1.

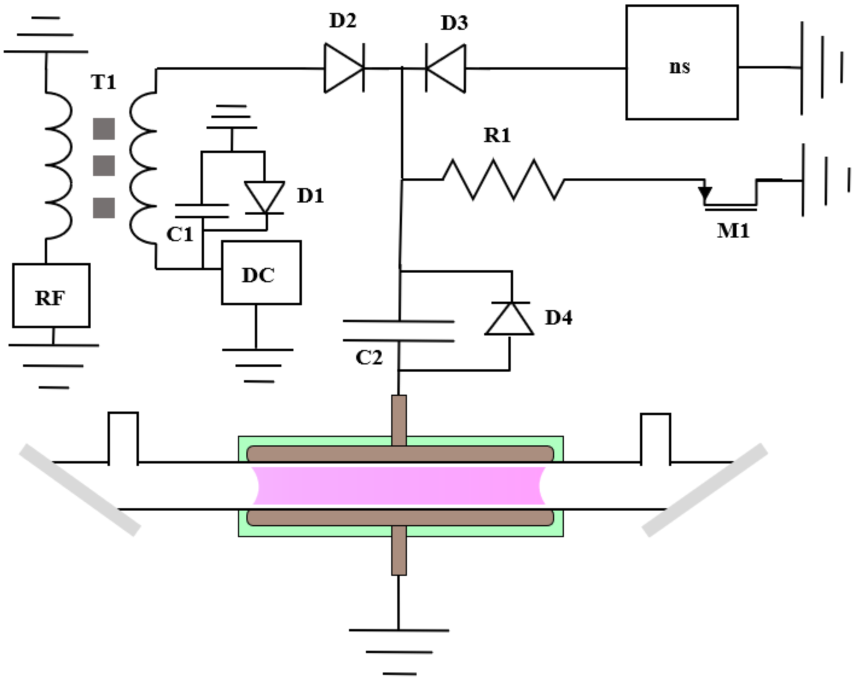

Figure B-1: Full Schematic of Hybrid Plasma External Circuit

For an alternating polarity RF source, this problem is more difficult. The solution is to first bias the RF waveform by adding a DC offset, such that the same voltage polarity is maintained during the RF burst. Once this is done, the current from the RF waveforms can be blocked by a series of diodes, and the DC bias can be subsequently removed with a filter. In this case the filter is simply a 660 nF capacitor, C2, in Figure B-1. D3 in Figure B-1. blocks the biased RF + DC waveforms from reaching the ns pulser. D3 is composed of 5 series avalanche diode described in Table B-1. Figure B-2 below illustrates the progression of the RF voltage; (a) shows the output of the RF source going into the primary of T1, (b) shows the waveform at the output of the secondary of T2, and (c) shows the waveform delivered to the load after passing through C2.

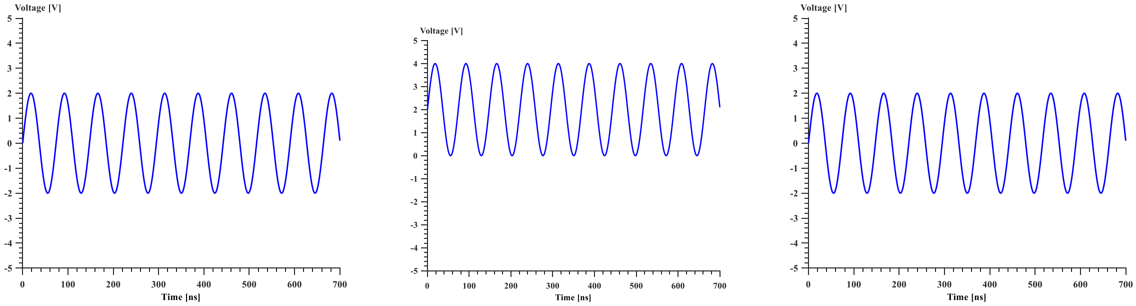

Figure B-2: Transformation of the RF Waveforms by the Circuit

To pass the RF waveform through the diode series D2, it is important that the DC current is engaged to ensure the presence of a bias current keeping the diodes in forward conduction. To allow this, a dummy 20 kΩ resistive load, R1, is connected in parallel with the capacitive load, and engaged only during the power delivery with a low-side MOSFET switch, M1.

Other auxiliary parts include capacitor C1 which helps stabilizing the DC power supply output. Diodes D1 and D4 serve as voltage clamps that protect C1 and C2 from over voltage. The parts list is given below in table B-1.

Table B-1: List of Parts Used in the Hybrid Electric Discharge Circuit

T1	Hand-Wound 1:1 Transformer	Vacuumschmelze T60006-L2063-W517 Ferrite rings (6x)
C1	25 μF Stabilizing Capacitor	Kemet ESG157M500AQ5AA Capacitors (3 series x 2 parallel)
C2	660 nF DC filtering Capacitor	WIMA SNFPX033308J1AKS00 Capacitors (2 parallel)
D1	Voltage Clamping Diode	3 Series VISHAY BYW 36-TR
D2	Pulse Blocking Diode	20 Series VISHAY BY269TR + 5 Series VISHAY BYT62-TAP
D3	RF/DC Blocking Diode	5 VISHAY BYT62-TAP
D4	Voltage Clamping Diode	3 Series VISHAY BYW 36-TR
R1	20 kΩ, low-inductance, DC Current Drain Resistor	4 Series Vishay / Dale ROX4005K00FNF5NT
M1	MOSFET	IXYS IXTX4N300P3HV
RF	RF Voltage Source	Dressler Cesar 5KW
DC	DC Voltage Source	Glassman LQ 5 kV, 2 Amp
ns	Ns pulser	MegaImpulse NPG-100K

The steps to operate the hybrid plasma circuit are listed below.

1. Turn on the main power on for the Mega-Impulse pulse generator. Make sure that the pulser is in external triggering mode, by ensuring the LED in the green front panel button is off when no trigger is applied. If the LED is on with no trigger applied, then the pulser is internally triggered, and the green front panel button needs to be toggled. Set the pulse energy in percent of full power with the knob in lower right corner. Set the maximum frequency in kHz with the knob in the top right. There is also a limit to the number of

pulses allowed per second which can be changed by pressing and holding the frequency knob, until the menu shows a flashing number, which sets this limit. By default, this number is reset to 1000 pulses per second with each power cycle. Turning the knob will then adjust this limit. At this point, enable the high-voltage output by toggling the red front panel button.

2. Turn on the main power for the DC source. Make sure the power supply is in the voltage controlled mode before proceeding. However, it is helpful to set a reasonable current limit in case of a circuit component failure. For instance, during previous operations, the maximum current required at any time during normal operations was 2kV/20kΩ = 100 mA, so the current was limited to this value. Make sure there is no trigger being sent to MOSFET.
3. Enable the high voltage and slowly increase the voltage from zero to the desired level. Since the MOSFET is not gated until the trigger is applied, there should be no continuous current being drawn from the DC source. If the current readout shows a non-zero continuous current, this indicates that something has failed, so the DC voltage should be shut off immediately. Because the DC filtering capacitor forms a capacitive voltage divider with the discharge cell (with a much smaller impedance) during the transient voltage increase, the node between the cell and the filtering capacitor is charged to the same voltage as the DC source. This stray charge needs to be removed, otherwise the electric field will not alternate polarity as intended. To discharge this node, a grounded wire should be brought into contact with the cell high-voltage electrode. It is best to repeat this process for every 500 V of DC voltage increase, to prevent a high peak current discharge through the grounding wire. **IT IS ESSENTIAL TO PREVENT**

ACCIDENTAL CONTACT WITH THE HIGH VOLTAGE SIDE OF THE CAPACITOR DURING THIS PROCEDURE. THIS IS EXTREMELY DANGEOURS AND MAY BE FATAL. EVEN ACCIDENTALLY SHORTING THE LIVE SIDE WITH THE GROUNDING WIRE WILL CAUSE A POWERFUL DISCHARGE THAT MAY INVOKE A DANGEROUS REFLEX.

4. Turn on the main power for the RF source and make sure that External Pulsing is turned on. Sometimes the power supply fails to load the settings from the last operation. Only after turning on the RF generator should the matching network be plugged in. If the matching network is powered before the generator, the internal control system will try to adjust the matching capacitors rather than maintain the previous value, and the matching point set during previous use will be lost. For this generator and circuit, the best matching was obtained when the network series capacitance is maximized and parallel capacitance is minimized. Importantly, the RF matching network was modified to bypass the output inductor in order to better match the impedance to the transformer load.
5. Turn on the SRS DG535 which provides the DC inputs necessary for successful external pulsing. Importantly, the offset from channel B controls the RF power set point during operation, with 0-10 V input corresponding to 0-5kW of forward power. The forward power should be chosen such that the resulting voltage amplitude does not exceed the DC bias set in Step 3, thus keeping the net DC + RF waveform before the filter positive. Two other TTL inputs are needed for pulse modulation. One primes the generator to receive the blanking signal, and the other is the blanking signal itself. The inputs to the for the external modulation are provided via a modified 15 pin D-sub cable connected to the rear

of the generator. The full description of the function of each pin can be found in the manual.

6. Turn on the fan mounted above D3, to facilitate the removal of heat dissipated in the diode junction.
7. After this the trigger for the pulser can be enabled. The proper triggering formula for the pulser can be found in the manual. Then the RF waveform can be added independently by starting its trigger. Note that the trigger for the MOSFET gate should always be synchronized with the RF burst, or else the RF waveform will be distorted. However, it is best for the MOSFET gate to be closed when the RF waveform is not applied, to prevent excessive heating of R1, D2, and M1.
8. To shut down the circuit, steps 1-7 should be repeated in the reverse order.

To monitor the performance of the circuit and check for any potential issues, a voltage probe should be attached to the high-voltage electrode and the waveforms should be monitored constantly. If any waveform distortion or unexpected behavior occurs, the system should be shut down immediately, and the cause investigated. Additionally, the time-averaged DC current drawn from the DC power supply should remain low if the plasma is operated in burst mode. If the current readout shows a sustained, high value of current, this is indicative of a circuit component failure, and the system should be shut down immediately. For the RF source, the maximum allowable voltage amplitude is 3 kV. This is because M1 cannot tolerate more than a 3kV DC bias. Again the DC bias must be greater than or equal to the RF voltage amplitude.

The component most susceptible to failure has been found to be the diode chain D3. This is most likely because of the reflected pulses returning to the pulser causing repeated avalanche breakdown of the diodes and dissipating heat in the junction. In the pulse burst regimes used thus far, it is normal for single diodes to fail (short-circuit) after several hours of operation. Because of the redundancy built in to the diode chain this is not a catastrophic occurrence. However, if all of the diodes in the chain fail (short circuit), the current from the DC source will flow directly to the pulser, which can cause severe damage to the pulser, especially if the current continues to flow unnoticed for a long time period. This is why it is important to operate the DC supply with an adequately low current limit as discussed in Step 2. With this in mind it is best to check the condition of these diodes after each use. This can be done by using the diode feature on a Fluke multimeter to measure the junction forward voltage, which is ~ 1V for a healthy VISHAY BYT62-TAP diode. A voltage significantly lower than this, or short-circuit across the junction indicates component failure. When 2 or more diodes have failed, it is advisable to replace them with spare ones, or even replace the whole series. When changing pulse burst parameters, it is advisable to find out what the expected lifetime of the diodes are before failure.

B.2 Quantum Cascade Laser and Data Acquisition

To operate the Quantum Cascade Laser in CW mode, which was done to take the data in Chapter 2, the following steps should be followed. The laser communicates to the HP Z210 Workstation Computer on the adjacent desk via a USB connection. The software with a GUI to control the laser is *Sidekick Controller*.

1. Turn on the chiller beneath the laser, making sure the set point is 17 ^{o}C.
2. Turn on the laser power supply and defeat the interlock by turning the key.
3. Open the Sidekick controller software and connect to the laser head.

4. After successfully connecting to the laser, arm the laser to engage the thermoelectric cooling of the chip.
5. Enter the desired wavelength in the wavelength field, and press ‘tune to wavelength’
6. After the chip temperature has stabilized, open the manual shutter, and press ‘turn emission on’ to turn the laser output on.
7. To turn the laser off, press ‘turn emission off’, disarm the laser, close the Sidekick program, turn off the power supply, turn off the chiller, and close the shutter.

The laser is contained inside an aluminum plate housing which acts as a Faraday cage to reduce the effect of EMI generated by the ns pulser and RF power generator on the laser power supply electronics. There is a BNC connection attached to the housing which can be used to connect the current or piezo tuning. In this case, the bnc connecter is connected the piezo grating drive. It is important to apply appropriate voltages so as not to damage the grating. Because of this, the piezo driver should always be operated with the internal voltage limit set to 100 V. Additionally the voltage should always be turned down to zero before turning the power to the driver off. Otherwise, upon re-powering the supply, the voltage will snap back to the set point and potentially shock the grating.

For alignment of the QCL output, in the existing optical setup there are two irises which prescribe the output beam path. Rough alignment of the beam to these two irises will guide the beam components to their respective detectors. To visualize the infrared beam and complete the alignment, it is necessary to use temperature sensitive plastic, or an infrared card to locate the spot on the iris. Because of this, it is nearly impossible to make an exact alignment. As a result, fine tuning of the beam paths should be done by optimizing the real time signal on the detectors by turning the micrometer screws on the mirrors before the detectors. The three infrared detectors used are all housed inside of another aluminum plate Faraday cage enclosure. The top of the enclosure can be easily removed to add liquid nitrogen to the detector dewars. The power for all 3 detector preamplifiers is applied by turning on the power strip with the three cables leading inside the enclosure. It is important that the detectors are turned off after use.

The data collection described in Chapter 2 was done using LabView to control the experiment timing and data acquisition. The same HP computer containing the Sidekick software has a National Instruments PCI-DAS4020/12 data acquisition card mounted in the PCI slot and the BNC cables from the 3 infrared detectors are terminated there. Additionally, the endmost BNC connection is a trigger input which starts the data acquisition when the TTL trigger is received. The main LabView program, *PZ_Tuner.vi,* contains all of the necessary parameters to carry out the data acquisition as described in Chapter 2. The high-level principle of the program's operation is to enable the 'step-and-measure' approach discussed in Chapter 2. In particular, the program records and saves the signals from the infrared detectors when it receives an external trigger. The parameters of the data aquisition can be set in the 'Sample Rate (Hz)' and 'Samples Per Channel' fields in the LabView GUI. These control the sampling frequency and the total number of samples in the acquisition respectively. When collecting data, it is essential to make sure the virtual pushbutton named 'Write Data' is 'depressed' or else the data are not saved upon acquisition. After the acquisition is complete the laser wavelength is tuned by stepping the piezo driver voltage by the amount set in the 'PZ Voltage Step' field. Then the program waits for the next external trigger and repeats this procedure. The voltage start and stop values are set in the 'PZ Start Voltage' and 'PZ End Voltage' fields in the LabView GUI. It is important that the voltage on the piezo driver is manually tuned to match the start value in the program, or else the voltage will jump to it at the start and potentially shock the grating. Once the voltage is tuned to the end value, the data acquisition ceases, and the program slowly detunes the voltage back to its start value. The data is saved as individual ASCII files generated at each voltage step, named simply #.lvm where # is the step number in the acquisition series starting from 1. The files are saved to the directory specified in the field ‘Data File Save Path’ of the LabView interface. Each column is the output from a unique channel. Time is not explicitly saved; it must be deduced from the row index and the sampling frequency. To control the timing of the data acquisition relative to the discharge burst, set the trigger timing relative to the electronics trigger on the SRS DG645 delay generator that is located in front of the computer.

Appendix C: CARS Measurement System

In Chapters 2 and 3, collinear CARS is used to measure vibrational populations of ground electronic state nitrogen molecules. The collinear geometry is simple to implement and generates a strong signal. Figure 2-2 illustrates the implementation used in these works. The fundamental output of a Continuum Surelite SLIII-10 Nd:YAG laser is frequency doubled to 532 nm, and then split by an 80:20 ratio beam-splitter. 80% of the beam is used to pump a custom broadband dye laser. The dye laser functions as the CARS Stokes beam, with the wavelength tailored to access the first 8 vibrational levels of $N_2(X_1\sum_g^+)$. The broadband output of the dye laser has the FWHM of approximately 6 nm, centered at 605 nm. The remaining 20% of the 532 nm beam passes through a ½ waveplate and polarizing beam splitter combination, used to vary its energy and proceeds to the probe region as the CARS pump and probe beams in the degenerate setup. To synchronize this with the Stokes beam, a delay line mounted on a translation stage is used to adjust the time delay between the arrival of the two beams. The 532 nm and 605 nm beam are overlapped using a R532/T605 dichroic mirror and then focused into the plasma volume by a 22 cm focal distance lens. The presence of vibrationally excited nitrogen, $N_2(X_1\sum_g^+,v)$, generates anti-stokes CARS signal as described in [77]. The signal is generated between 473 and ~478 nm depending on how many vibrational levels are detected in the spectra. This signal is recollimated by a 25 cm focal distance lens and separated from the input beams by R473/T532/T605 dichroic mirrors. The spectral content is dispersed with an Andor Shamrock SR-750-B2 spectrometer (Czerny-Turner configuration), and imaged with an Andor Newton 971 EMCCD camera. The signal is passed through a narrow T743 bandpass filter to remove the residual pump/probe beams, and then focused onto the entrance slit, kept at 10 µm for these measurements.

In this work, the Continuum Surelite, SLIII-10 Nd:YAG laser is operated in conjunction with a Continuum injection seeder. Injection seeding reduces the Nd:YAG laser linewidth from ~0.50 – 0.64 cm-1 (measured with a High Finesse WS-6 wavelength meter), to ~0.0053 – 0.018 cm-1, as quoted by the manufacturer. This improves the spectral resolution of CARS, to partially resolve the rotational lines in the v=0 and v=1 bands of N_2, used for the inference of the rotational-translational temperature. The spectral output is centered at 532.25 nm, regardless of whether the injection seeding is turned on or off, as measured by the wavemeter. In the present experiments the Nd;YAG laser is externally triggered by the falling edge of a 5 V TTL trigger pulse sent to the flashlamp and Q-switch. The delay of the Q-switch is kept at 300-350 µs.

The custom-made broadband dye laser, described in [78] was used in this work with no significant changes, except for the intentional misalignment of the amplified spontaneous emission dye cell, as discussed in detail below. The conversion efficiency of the broadband dye laser depends strongly on the concentration and age of the dye, as well as the energy of the 532 nm pump beam. In the present work, the dye mixture contains around 500 mg each of Kiton Red 620 (KR620) and Rhodamine 640 (R640) dyes, dissolved in methanol. Varying the relative concentrations of KR620 and R640 allows to tune the center of the dye laser spectral output, with the addition of the R640 results in a red shift, and the addition of a solution of the two dyes (50:50 ratio) in methanol producing a blue shift. The output power of the dye laser is optimized by adding methanol to the dye solution, until the energy per pulse reaches its maximum at a constant pump laser power.

In the present experiments, the spectral output of the dye laser is centered near 605 nm and has a full width at half-max (FWHM) of 7 nm, as shown in Figure 2-8 (top), which gives access to several vibrational bands of N_2. N_2(v” = 0 – 7) vibrational band centers are shown in the figure. The dye laser spectrum is obtained by measuring non-resonant CARS spectrum in argon and calculating the wavelength from the Raman shift,

$$\frac{1}{\lambda_{Stokes}} = \frac{2}{532\ nm} - \frac{1}{\lambda_{CARS}} \qquad (C1)$$

To analyze the CARS data with the CARSFT computer program [44] for the inference of vibrational and rotational temperatures, the background signal originating from the dark current on the camera chip is subtracted. Next, the spectrum is normalized by dividing it over the non-resonant background measured in argon. To measure the N_2 vibrational distribution with high-resolution, it is expeditious to measure the non-resonant CARS signal generated over the same wavelength range as the resonant N_2 signal. By flowing argon through the jet channel and displacing the ambient air, a strong non-resonant signal is created by the system and imaged by the spectrometer, due to the relatively high value of argon’s non-linear susceptibility, $\chi^{(3)}$. Because $\chi^{(3)}$ is effectively constant over this wavelength range, the resultant non-resonant CARS signal is proportional to the dye laser spectral intensity distribution. The dark current background is removed from this signal, leaving behind the Raman-shifted spectral distribution of the dye laser.

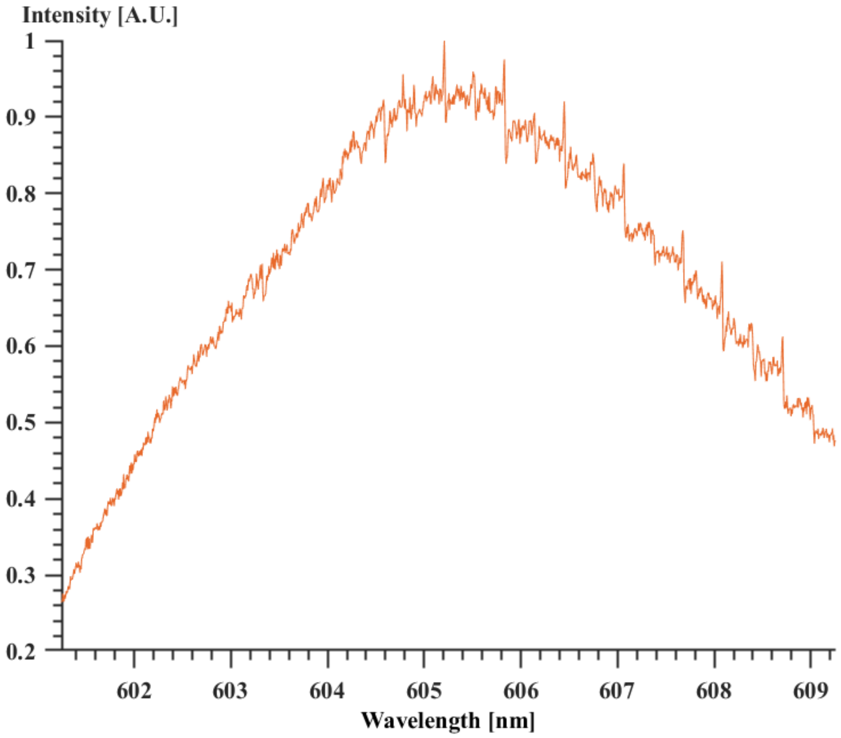

Figure C-1: Spectral Intensity Distribution of the Broadband Dye Laser

When measuring the Raman-shifted spectral distribution of the dye laser at high-resolution, the appearance of regularly spaced etalon fringes became apparent. By measuring the non-resonant background in real time, these fringes were found to originate from the oscillator cavity in the dye laser ([78], Figure 2-7). Because these fringes are not completely stable and because a weak CARS signal can be overwhelmed by them, it is desirable to reduce this effect and operate with a ‘smoother’ dye laser spectral output. By slightly misaligning the ASE cavity high reflector and output coupler and monitoring the real time non-resonant background signal, an acceptable trade-off was identified where the spectral distribution of the laser was smoothed without reducing the total output power significantly. This change is shown below in Figure C-2.

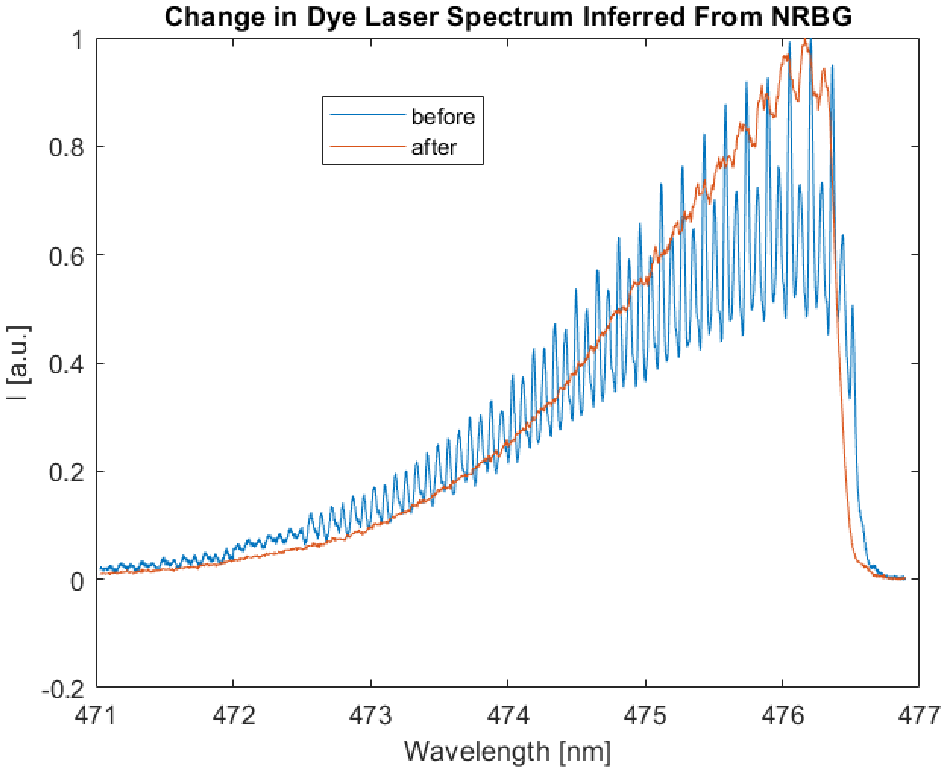

Figure C-2: Change in Dye Laser Spectral Distribution Caused by Misalignment of the Oscillator Cavity

The non-resonant signal is also helpful to identify the spatial region over which CARS signal is generated. This was done by placing a 1 mm thick glass microscope slide on a translation stage near the focal point of the pump/probe/Stokes beams and traversing the slide along the beam axes. Because glass also has a much higher value of $\chi^{(3)}$ than air, the resulting non-linear signal is dominated by the 1mm slide, enabling mm-scale mapping of the CARS signal origin. The slide is then traversed over a 45 mm linear path centered at the nominal beam focal point. Figure C-3 shows that 95 % of the signal is generated within 20 mm centered at the focal point. The spatial distribution deviates from the expected Gaussian distribution. This is most likely due to the less-than-optimal beam quality of the dye laser, as it does not focus as tightly as the YAG beam.

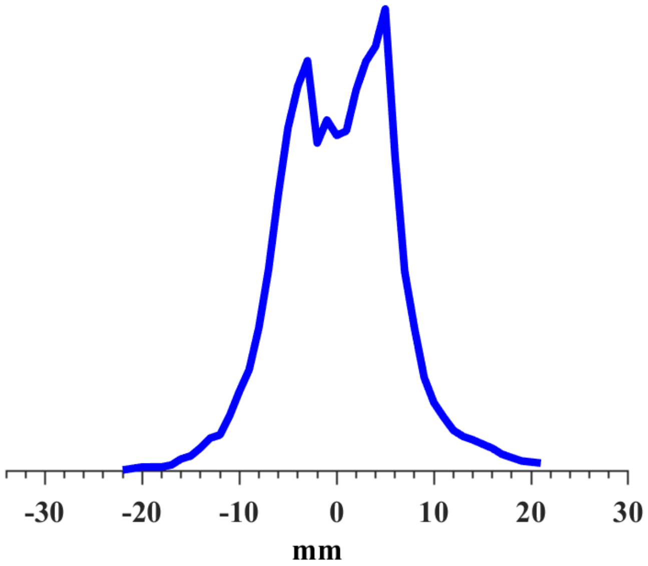

Figure C-3: Distribution of Non-Resonant CARS Signal From Microscope Slide. 0 mm Represents the Focal Point

Finally, it is necessary to calibrate the Andor CARS spectrometer, as the wavelengths reported by the spectrometer tend to be inaccurate. This is accomplished by matching the location of rotational lines in a spectrum exhibiting strong vibrational excitation to their known wavelength. In particular, the locations on the experimental axis are matched to the known location by using a spline fit, implemented by the MATLAB function *makima*. Then the spline fit is applied to the entire spectrum is applied to the entire spectrum to convert to the calibrated coordinates using the MATLAB function *ppval*. The choice of points used for the calibration are tabulated below. Note that the list of the experimentally measured wavelengths may need to be updated for future use as the system is realigned and the grating optics may shift somewhat.

Table C-1: Measured Lines and Reference Locations used to Calibrate Spectrometer

Measured Location, cm^{-1}	Reference Location, cm^{-1}	Description
2330.090	2329.750	V”(0), Q”(0)
2327.500	2327.150	V”(0), Q”(7)
2324.150	2323.850	V”(0), Q”(13)
2301.100	2301.370	V”(1), Q”(0)
2297.295	2297.570	V”(1), Q”(9)
2272.620	2272.660	V”(2), Q”(0)
2264.870	2265.030	V”(2), Q”(17)
2243.210	2243.860	V”(3), Q”(0)
2237.000	2237.650	V”(3), Q”(13)
2213.890	2215.070	V”(4), Q”(0)
2209.990	2211.150	V”(4), Q”(11)
2184.800	2186.320	V”(5), Q”(0)
2155.330	2157.270	V”(6), Q”(0)
2126.110	2128.290	V”(7), Q”(0)

The energy of the 532 nm beam, used to pump the dye laser, and of the 605 nm dye laser output beam is measured using the Ophir PE50BF-DIF-C power meter. During the present experiments, the dye concentration was maintained by adding methanol to the mixture as needed, to counter its gradual evaporation and to maintain an approximately constant volume of the dye solution in the system (500 mL level in both glass bottles of the dye pump). The possible causes for the reduction in conversion efficiency over time are the loss of internal alignment of the dye laser and the degradation of the dye.

Appendix D: V-V and V-T Rate Expressions

V-V processes for ground electronic state N2-N2

$$N_2(v) + N_2(w) \longleftrightarrow N_2(v\text{-}1) + N_2(w\text{+}1), \quad 0 \le v,w \le 40$$

$$k_{w\to w+1}^{v\to v-1} = (w+1)(v)k_{0\to 1}^{1\to 0}\exp\left(-\delta_{VV}|w-(v-1)|\right)\left(\frac{3}{2}-\frac{1}{2}\exp(-\delta_{VV}|w-(v-1)|\right)$$

$$\delta_{VV} = \frac{6.85}{\sqrt{T\,(K)}}\ ,\ k_{0\to 1}^{1\to 0}(T) = 1.5\cdot 10^{-14}\cdot\left(\frac{T}{300}\right)^{3/2}\left[\frac{cm^3}{s}\right] \quad \text{(Ref. [53])}$$

Approximation used for the Landau-Teller temperature scaling incorporated in Chemkin Pro:

$$\frac{A}{\sqrt{T}} \approx \frac{A}{2}\left(\frac{1}{T^{\frac{1}{3}}T_0^{\frac{1}{6}}} + \frac{T_0^{\frac{1}{6}}}{T^{\frac{2}{3}}}\right) \approx \frac{B}{T^{\frac{1}{3}}} + \frac{C}{T^{\frac{2}{3}}}\,,$$

where $B = \frac{A}{2}\cdot T_0^{-\frac{1}{6}} \approx 1.12,\quad C = \frac{A}{2}\cdot T_0^{\frac{1}{6}} \approx 10.44$ for $T_0 = 800$ K.

V-T processes for N2-N2 and N2-Ar

$$N_2(v) + M \longleftrightarrow N_2(v\text{-}1) + M, \quad 0 \le v \le 40$$

$$k_{v\to v-1} = k_{1\to 0}\cdot v\cdot\exp\left(\delta_{VT}(v-1)\right), \quad \delta_{VT} = \frac{1.94}{T^{\frac{1}{3}}} \quad \text{(Ref. [54])}$$

$$k_{1\to 0}(T) = 3.0\cdot 10^{-4}\cdot\exp\left(-\frac{400}{T^{\frac{1}{3}}} + \frac{886}{T^{\frac{2}{3}}}\right)\left[\frac{cm^3}{s}\right] \quad \text{(Ref. [54])}$$

$$k_{1\to 0}(T) = 2.0\cdot 10^{-4}\cdot\exp\left(-\frac{405}{T^{\frac{1}{3}}} + \frac{1055}{T^{\frac{2}{3}}}\right)\left[\frac{cm^3}{s}\right] \quad \text{(Ref. [56], Pot II)}$$

V-T processes for N_2-N

$$N_2(X, v) + N \leftrightarrow N_2(X,w) + M, \quad 0 \leq v,w \leq 40$$

Expressions for $k_{v\rightarrow w}(T)$ are calculated using a computer code provided by the authors of Ref. [55].